Studies of Models with Large Extra Dimensions in CMS

von

Metin Ata

Diplomarbeit in Physik

vorgelegt der

Fakultät für Mathematik, Informatik und Naturwissenschaften
der Rheinisch-Westfälischen Technischen Hochschule Aachen

im November 2009

angefertigt im

III. Physikalischen Institut A
Prof. Dr. Thomas Hebbeker

Zweitgutachter

Prof. Dr. Christopher Wiebusch

Zusammenfassung

Die vorliegende Arbeit präsentiert eine Monte Carlo Studie zu Theorien mit Large Extra Dimensions (LEDs) im myonischen Zerfallskannal und das dazugehörige Entdeckungspotential des Compact Muon Solenoids, kurz CMS Detektors. LEDs sind zusätzliche, räumlich kompaktifizierte Dimensionen welche nur für die Gravitation zugänglich sind. Die Einführung von LEDs wurde dadurch motiviert, dass die gravitative Wechselwirkung zuvor nie bei Abständen kleiner als ein Millimeter getestet worden ist. Im Falle der Existenz von LEDs wird die fundamentale Skala der Gravitation von der sogenannten Planck Skala $M_{Planck} \sim 10^{16}\,\text{TeV}$ zur elektroschwachen Skala M_{EW} reduziert, welche mit $M_{EW} = 1\,\text{TeV}$ deutlich niedriger ist als die Planck Skala und damit auch das Hierarchie Problem löst. Obwohl vorhergehende Experimente an den Beschleunigern wie LEP am CERN und Tevatron am Fermilab nach der Existens von LEDs gesucht haben, war bisher noch kein Nachweis für LEDs möglich.
Durch die signifikant höhere Schwerpunktenergie von bis zu 14 TeV am LHC, verglichen zu den anderen genannten Beschleunigern, wird es schon mit den frühzeitigen Daten von etwa $100\,\text{pb}^{-1}$ möglich sein, (Ausschluss-)Grenzen auf verschiedene Parameterpunkte zu erweitern, welche für die Beschleuniger LEP und Tevatron unzugänglich waren.
Die hier vorgestellte Studie basiert auf vielen, unabhängig voneinander angewandten Schnitten auf die Myoneigenschaften. Die Monte Carlo Simulationen wurden mit dem Computer-Framework SHERPA (**S**imulation for **H**igh-**E**nergy **R**eactions of **PA**rticles) generiert und anschließend wurde mit der CMS Software (CMSSW) eine volle Simulation des CMS Detektors durchgeführt.

Abstract

This thesis presents Monte Carlo studies of models with Large Extra Dimensions (LEDs) in the di-muon channel and their discovery potential with early data taken by the Compact Muon Solenoid, shortly CMS detector. LEDs are additional compactified spatial dimensions where only gravity can propergate into. The postulation of LEDs has been motivated by the fact that gravity had never been tested at distances shorter than a millimeter. Assuming LEDs, the fundamental scale of gravity decreases from the so called Planck Scale, $M_{Planck} \sim 10^{16}\,\text{TeV}$ to the Electroweak Scale, which is much lower at $M_{EW} \sim 1\,\text{TeV}$ and thus solves the Hierarchy Problem. Although at former accelerators like LEP at CERN and Tevatron at Fermilab searches for LEDs have been performed, there has been no evidence of LEDs so far.
Due to the significantly higher center of mass energies up to 14 TeV at LHC compared to Tevatron and LEP, already early data of $100\,\text{pb}^{-1}$ will extend the limits for parameter points, which have been inaccessible for the other two accelerators.
The analysis shown in this thesis is a cut-based one, meaning that only rectangular cuts have been applied. The Monte Carlo simulations have been done using the multipurpose event-generation framework SHERPA (**S**imulation for **H**igh-**E**nergy **R**eactions of **PA**rticles) and afterwards the CMS Software (CMSSW) to get a full simulation of the CMS detector.

Contents

Chapter 1

Introduction

In this thesis several conventions and short forms will be used which need to be explained. The very common *natural* units $\hbar = c = 1$ are used. The space-time coordinate x is representative for the contravariant vector $x = x^\mu = (t, \vec{x})$ by default. The corresponding covariant vector is obtained by : $x_\mu = g_{\nu\mu}x^\nu$ with the metric tensor $g_{\mu\nu} = \text{diag}(1, -1, -1, -1)$ so that the *invariant* mass m of a particle is given by:

$$p^2 = p^\mu p_\mu = E^2 - |\vec{p}|^2 = m^2 \tag{1.1}$$

This formula is also known as energy-momentum relation. If a particle obeys this relation, it is called *on-shell* , if not it is *off-shell*. The invariant mass of a system is a conserved quantity. It represents the energy of the particles (in their center of mass frame) before a reaction (collision) takes place. One can see, that the invariant mass of a single particle is its rest mass, where else the invariant mass of a system of particles is larger than the sum of the single masses. This work will mainly concentrate on the invariant mass of two muons, from now on called invariant di-muon mass. The variables p_x, p_y, p_y are physically adequate but experimentally the CMS detector measures the variables p_t which is the *transverse* momentum $p_t = \sqrt{p_x^2 + p_y^2}$, the polar angle φ and the pseudorapidity $\eta = -\ln\left[\tan\left(\frac{\theta}{2}\right)\right]$. Both sets of variables (coordinates) are equivalent and can be transformed to each other.

Chapter 2

Theoretical Considerations

2.1 The Standard Model

The Standard Model (SM) is a gauge theory, which describes strong, weak and electromagnetic interactions, via the exchange of the corresponding gauge fields: eight massless gluons and one massless photon, respectively, for the strong and electromagnetic interactions, and three massive bosons, $W^{\pm}$ and Z, for the weak interaction [1]. In the Standard Model the structure of matter is explained by the known leptons l and quarks q (and the corresponding anti-particles $\bar{l}$ and $\bar{q}$), which are organized in a three-fold family structure. Quarks participate in every interaction, whereas leptons do not interact strongly. Experimentally quarks have not been observed as free particles. They are the constituents of mesons ($q\,\bar{q}$) and (anti-)baryons ($q\,q\,q$ and $\bar{q}\,\bar{q}\,\bar{q}$).
Quantum Field Theory (QFT) is the mathematical description of the Standard Model which characterizes particles as quantized fields. The interactions between elementary particles are mediated by four types of gauge bosons (Figure 2.1). The interactions themselves and the quantum

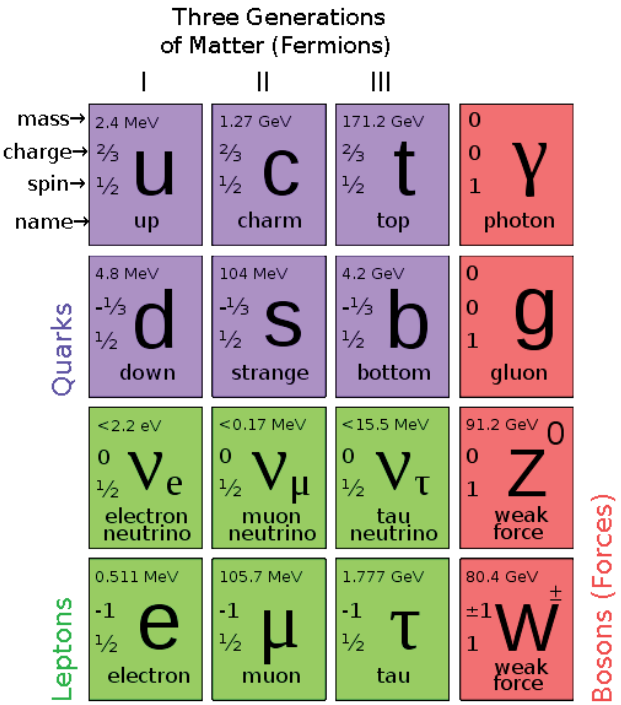

Figure 2.1: Particles of the Standard Model are divided into three generations of leptons and quarks. The four known types of gauge bosons are in the most right column [2].

fields are described by the lagrange density (Lagrangian) $\mathcal{L}$. It is constructed that it leads to the

Euler-Lagrange equation:

$$\frac{\partial \mathcal{L}}{\partial \phi_i} - \partial_\mu \left(\frac{\partial \mathcal{L}}{\partial(\partial_\mu \phi_i)} \right) \equiv 0,$$

and thus provide the equation of motion. A spin 1/2 particle is described by the Dirac equation $(i\gamma^\mu \partial_\mu - m)\psi = 0$, and the corresponding Lagrangian $\mathcal{L}$,

$$\mathcal{L} = \bar{\psi}(i\gamma^\mu \partial_\mu - m)\psi = \bar{\psi}(i\not{\partial} - m)\psi,$$

where ψ and $\bar{\psi}$ describe independent fields. The gravitational force is not considered in the Standard Model, as it does not play a role at the distances of interacting elementary particles. No quantum field theory for gravity has been successfully formulated so far.

2.1.1 Gauge Theory and Symmetries

The Standard Model is a gauge theory based on local symmetry describing the microscopic interactions. It is partly represented as an abelian and as a non-abelian gauge theory.

The gauge principle: A Dirac field will be submitted to a gauging processes [3]. The choice of a Dirac field is arbitrary, as the whole procedure shown here also works for (complex scalar) Klein-Gordon fields. The Lagrangian:

$$\mathcal{L} = \bar{\psi}(i\not{\partial} - m)\psi, \tag{2.1}$$

is invariant under a phase transformation of the form $U = \mathrm{e}^{iq\chi}$:

$$\psi \rightarrow \psi' = U\psi, \tag{2.2}$$
$$\bar{\psi} \rightarrow \bar{\psi}' = \bar{\psi}U^\dagger, \tag{2.3}$$

where $U \in U(1)$ is a unitary operator of the corresponding symmetry group, and q and χ are scalars, which means that $\mathcal{L}$ is invariant under global gauge transformations.

If the unitary transformation is depending on the space-time variable $U \equiv U(x)$ and $\chi \equiv \chi(x)$, the derivative of the Dirac field has to be written as:

$$\partial_\mu \psi \rightarrow \partial_\mu \psi' = \mathrm{e}^{iq\chi(x)} \partial_\mu \psi + iq\psi \partial_\mu \chi(x), \tag{2.4}$$

and therefore the Lagrangian assumes the form:

$$\mathcal{L}' = \bar{\psi}(i\not{\partial})\psi - q\bar{\psi}\gamma^\mu \psi \partial_\mu \chi - m\bar{\psi}\psi \not= \mathcal{L}, \tag{2.5}$$

which means, that this Lagrangian is not invariant under local gauge transformations. To restore the local invariance, the definition of a covariant derivative is necessary with the implementation of a new gauge field A_μ, which transforms like:

$$A_\mu(x) \rightarrow A'_\mu(x) = A_\mu(x) - \partial_\mu \chi(x), \tag{2.6}$$

where $\chi(x)$ is a scalar field depending on the space-time variable x. So the new, *covariant* derivative can be written as:

$$D_\mu = \partial_\mu + iqA_\mu(x). \tag{2.7}$$

Restoring local gauge invariance is equivalent to adding an interacting gauge field. This also allows to make the reverse consideration, meaning that the interaction of fields (the elementary particles) can be described in an elegant way by demanding the Lagrangians to be local gauge invariant. QED, Quantum Electro Dynamics, is an example for a local gauge theory, where the

gauge field A_μ describes the gauge boson of the electromagnetic field, the photon. A mass term, written as

$$\frac{m^2}{2} A_\mu A^\mu, \tag{2.8}$$

of the gauge field would spoil the local gauge invariance of the QED. Experimentally it has been shown, that the photon is a massless particle, indeed.

Non-Abelian gauge theory: A particle traveling in space-time not only changes its phase, but can also change other properties like color (strong interaction) or flavor (charged currents of the weak interaction). Therefore it is crucial to consider not only a one-dimensional parameter $\chi(x)$ within the transformation, but more generally a whole set of parameters. This can be achieved with a unitary $n \times n$ matrix description of a more complex transformation acting on the wave function $\psi(x)$:

$$U \equiv \mathrm{e}^{\,i \sum_{j=1}^{\mathcal{O}(G)} T_j a^j}. \tag{2.9}$$

The matrices a^j and T_j are depending on the considered group [4]. For a group of the dimension $\mathcal{O}(G) = n$, the number of T_j matrices is fixed by the relation n^2 [1]. The hermetic matrices T_j have to satisfy the relation

$$[T_i, T_j] = i c_{ijk} T_k, \tag{2.10}$$

which means that they do not commutate. c_{ijk} is called the structure constant and has to be completely asymmetrical under permutations of its indices.

2.1.2 Standard Model of Electroweak Interactions

The electromagnetic and the weak forces can be described simultaneously by a non-abelian gauge theory, called the GSW-Model [5] of the electroweak force formulated in the 1960s. The weak force maximally violates parity [2], meaning that it distinguishes between left and right. In particle physics the helicity of a particle is calculated as :

$$H = \frac{\vec{p} \cdot \vec{\sigma}}{|\vec{p}| \cdot |\vec{\sigma}|}, \tag{2.12}$$

where $\vec{p}$ is the momentum of the particle and $\vec{\sigma}$ the rotation axis of its spin. For $H = +1$ the particle is called right handed, for $H = -1$ it is left handed. The projection of a field into complementary left and right handed parts is done with the projection operators:

$$P_R = \frac{1}{2}(1 + \gamma^5),$$
$$P_L = \frac{1}{2}(1 - \gamma^5).$$

An elegant way to characterize left- and right-handed particles is by the weak isospin. Left-handed particles have isospin $I = 1/2$ so that they form a doublet with respect to the weak force:

$$\begin{pmatrix} \nu_e \\ e^- \end{pmatrix}_L \begin{pmatrix} \nu_\mu \\ \mu^- \end{pmatrix}_L \begin{pmatrix} \nu_\tau \\ \tau^- \end{pmatrix}_L \begin{pmatrix} u \\ d' \end{pmatrix}_L \begin{pmatrix} s \\ c' \end{pmatrix}_L \begin{pmatrix} t \\ b' \end{pmatrix}_L \quad \begin{matrix} I_3 = 1/2 \\ I_3 = -1/2. \end{matrix}$$

[1] For e.g. the special unitary group SU(2) the number of T_j matrices is given by $n^2 - 1$ as one parameter of the matrices is fixed by the constraint of the determinant of the matrices.

[2] Π: parity-operator

$$\Pi f(x) = f(-x) = \begin{cases} f(x) & p = +1 \\ -f(x) & p = -1 \end{cases} \tag{2.11}$$

The right-handed particles with isospin $I = 0$ transform like singlets:

$$e_R,\ \mu_R,\ \tau_R,\ u_R,\ d_R,\ s_R,\ c_R,\ b_R,\ t_R.$$

This implies that right-handed neutrinos cannot be transformed in the Standard Model as they only form a singlet. As the electroweak force is not symmetric w.r.t. left- and right-handed fermions, the description can be done by the gauge group $SU(2)_L \times U(1)_Y$, where L stands for left-handed and Y is the hypercharge which is related to the electric charge Q by the Gell-Mann-Nishiyima relation [4]:

$$Q = I_3 + \frac{1}{2}Y, \tag{2.13}$$

where I_3 is the third component of the isospin w.r.t. the quantization axis. It can be seen that left-handed leptons must have $Y = -1$, whereas the right-handed leptons have $Y = -2$. To enforce the local gauge invariance, an external gauge field is needed which modifies the covariant derivative. In the case of $SU(2)_L$ the Pauli matrices $\mathbf{T} = (\tau_1/2, \tau_2/2, \tau_3/2)$ are used as generators of the group. It is necessary to introduce a triplet of gauge fields:

$$\mathbf{W}^\mu = \begin{pmatrix} W_1^\mu \\ W_2^\mu \\ W_3^\mu \end{pmatrix}. \tag{2.14}$$

For $U(1)_Y$ just one additional gauge field B^μ is needed. The covariant derivative then takes the form

$$D^\mu_{EW} = \partial^\mu + ig\,\mathbf{T}\cdot\mathbf{W}^\mu + i\frac{g'}{2}YB^\mu. \tag{2.15}$$

For left-handed leptons with $\mathbf{T} = \tau/2$ and $Y = -1$ the derivative is calculated as

$$D^\mu = \partial^\mu + i\frac{g}{2}\tau\cdot\mathbf{W}^\mu - i\frac{g'}{2}B^\mu, \tag{2.16}$$

where for right-handed ones with $\mathbf{T} = 0$ and $Y = -2$ the covariant derivative becomes:

$$D^\mu = \partial^\mu - ig'B^\mu. \tag{2.17}$$

The next step now is to identify the fields $\mathbf{W}^\mu$ and B^μ with the experimentally measured vector bosons as shown in Figure 2.1. The fields $W^{(\pm)\mu}$ are calculated as follows:

$$W^{(\pm)\mu} = \frac{1}{\sqrt{2}}(W_1^\mu \pm W_2^\mu). \tag{2.18}$$

The electromagnetic field A^μ and the field of the neutral weak current Z^μ are

$$A^\mu = B^\mu\cos\theta_W + W_3^\mu\sin\theta_W, \tag{2.19}$$
$$Z^\mu = -B^\mu\sin\theta_W + W_3^\mu\cos\theta_W. \tag{2.20}$$

The electromagnetic-weak-charge ratio is given as

$$e = g'\cos\theta_W = g\sin\theta_W, \tag{2.21}$$

where e is the electric charge, g, g' are the weak charges, and θ_W the weak mixing (*Weinberg*) angle.

2.1.3 Quantum Chromodynamics (QCD)

QCD is the theory of strong interactions which only involves the quarks and gluons but not leptons. It is a non-abelian gauge theory based on the group $SU(3)_C$ due to three additional degrees of freedom, the color charges red , green and blue (R, G, B). The entire wave function Ψ of quarks then can be written as a product of the Dirac wave function $\psi(x)$ and the color-spinor χ_{color}:

$$\Psi = \psi(x) \cdot \chi_{\text{color}} \tag{2.22}$$

So quarks can be charged R, G, or B and anti-quarks $\bar{R}, \bar{G}$, or $\bar{B}$ w.r.t. the color spinor Ψ. To conserve the $SU(3)_C$ invariance the quarks must have the same masses in all color states. Quarks never appear as isolated particles, which is called confinement. Hadrons (particles consisting of quarks) are always in a colorless state. The mediators of the strong force, the massless gluons themselves carry a color-charge, so that gluons also feature self-coupling. As darstellung of the $SU(3)_C$ group, the 8 Gell-Mann matrices λ_i are used. QCD interaction is described by the Lagrangian:

$$\mathcal{L}_{QCD} = -\frac{1}{4}\sum_{a=1}^{8} F_{a,\mu\nu}F_a^{\mu\nu} + \sum_{j=1}^{n_f} \bar{q}_j(i\not{D} - m_j)q_j \tag{2.23}$$

where the q_j are the quark fields, n_f the number of different quark flavors and m_j their respective masses; $\not{D} = D_\mu\gamma^\mu$ is the covariant derivative with $D^\mu = \partial^\mu + i\frac{g_s}{2}\lambda_i G_j^\mu$, and $F_a^{\mu\nu}$ is the field-strength-tensor given by:

$$F_a^{\mu\nu} = \partial^\mu G_a^\nu - \partial^\nu G_a^\mu - g_s f_{abc} G_b^\mu G_c^\nu, \tag{2.24}$$

containing the gluon field G_a^μ and describing its self-interaction. As QED interactions get stronger with shorter distances, the QCD coupling strength rises with distance. If one quark has enough energy to depart from another quark, the energy stored in the interacting field gets so high that new hadrons are created from the field; this is called hadronization.

2.1.4 The Higgs Mechanism

In the previous section the gauge structure of interacting fields has been discussed. Demanding that the Lagrangians have to be locally gauge invariant, interacting fields have been introduced. These fields describe massless gauge bosons. Experimentally it has been shown that bosons of the weak force, $W^\pm$ and Z^0 do have mass. Since the theory of electroweak interaction does not contain these masses, there has to be a mechanism responsible for them. A solution of this problem is the Higgs mechanism. Its approach to make massive $W^\pm$ and Z^0 bosons is to introduce a doublet of two complex fields, ϕ^+ and ϕ^0:

$$\Phi = \begin{pmatrix} \phi^+ \\ \phi^0 \end{pmatrix} = \frac{1}{\sqrt{2}}\begin{pmatrix} \phi_3 + i\phi_4 \\ \phi_1 + i\phi_2 \end{pmatrix} \qquad (I = 1/2,\ Y = 1) \tag{2.25}$$

with the Lagrangian:

$$\mathcal{L}_{Higgs} = (D_{EW}^\mu\Phi)^\dagger(D_{EW,\mu}\Phi) - V(\Phi^\dagger\Phi) = \mathcal{L}_{Higgs} = (D_{EW}^\mu\Phi)^\dagger(D_{EW,\mu}\Phi) + \mu^2\Phi^\dagger\Phi - \lambda(\Phi^\dagger\Phi)^2. \tag{2.26}$$

Now the vacuum expectation value VEV of the neutral Higgs field ϕ^0 is set to be different from 0 whereas the VEV of the charged field ϕ^+ has to vanish [3].

$$\langle 0|\Phi|0\rangle = \frac{1}{\sqrt{2}}\begin{pmatrix} 0 \\ v \end{pmatrix}, \qquad v = \sqrt{\frac{-\mu^2}{\lambda}} \tag{2.27}$$

By this choice of the VEV, the symmetry of the lowest energy state of the potential $V(\phi)$ is broken as shown in Figure 2.2. This also implies that the whole electroweak symmetry is broken from $SU(2)_L \times U(1)_Y$ to $U(1)_{em}$. This means that the symmetry group $U(1)_{em}$ is not broken and the photon remains massless by the choice of the higgs dublet.

[3] If the charged part would not vanish, the photon would also acquire a mass.

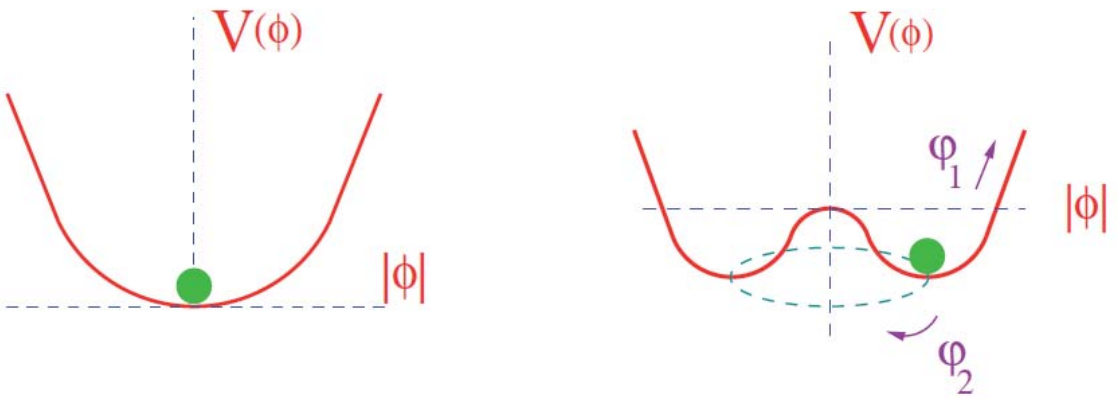

Figure 2.2: Potential of non-broken (left) and broken ground state symmetry (right) [6].

The field $\Phi(x)$ can be expanded around the minimum v according to:

$$\Phi(x) = \frac{1}{\sqrt{2}} \begin{pmatrix} 0 \\ v + \eta(x) \end{pmatrix}. \tag{2.28}$$

Plugging this field into the Lagrangian $\mathcal{L}_{Higgs}$ in Equation 2.26, the masses of the gauge bosons $W^{\pm}$ and Z are set with $M_W = \frac{gv}{2}$ and $M_Z = \frac{M_W}{\cos\theta_W}$; the later relation is experimentally confirmed by measurements.

2.1.5 Basics of Field Quantization

In analogy to non-relativistic Quantum Mechanics, fields of elementary particles can also be quantized and treated as operators. Let Φ describe a scalar particle with spin 0. The commutation relations between operator of the field $\Phi(\vec{x}, t)$ and the canonical conjugated momentum $\Pi(\vec{x}, t)$ has to be set (in analogy to non-relativistic Quantum Mechanics) as follows:

$$\begin{aligned} \left[\Phi(\vec{x}, t), \Phi(\vec{x}', t)\right] &= 0 \\ \left[\Pi(\vec{x}, t), \Pi(\vec{x}', t)\right] &= 0 \\ \left[\Phi(\vec{x}, t), \Pi(\vec{x}', t)\right] &= i\delta(\vec{x} - \vec{x}') \end{aligned}$$

The fields can be expanded in Fourier-space:

$$\Phi(\vec{x}, t) = \sum_k a(\vec{k}) \cdot u_k(\vec{x}), \tag{2.29}$$

$$\Pi(\vec{x}, t) = \sum_k a(\vec{k}) \cdot u_k^*(\vec{x}), \tag{2.30}$$

with the plane waves $u_k(\vec{x})$. The next step is to determine the solution of the Klein-Gordon equation with a quantized field (the same procedure is used for Dirac fields).

$$\Phi(x) = \frac{1}{\sqrt{2\pi}^3} \int_0^{\infty} \frac{d^3\vec{k}}{2k_0} \left(a(\vec{k}) e^{-ikx} + b^{\dagger}(\vec{k}) e^{+ikx} \right) \tag{2.31}$$

$$\Phi^{\dagger}(x) = \frac{1}{\sqrt{2\pi}^3} \int_0^{\infty} \frac{d^3\vec{k}}{2k_0} \left(a^{\dagger}(\vec{k}) e^{+ikx} + b(\vec{k}) e^{-ikx} \right) \tag{2.32}$$

As demanded by the commutator relation above, all commutators of $a(\vec{k})$ and $b(\vec{k})$ have to equal 0 except:

$$\left[a(\vec{k}), a^\dagger(\vec{k}')\right] = 2k^0\delta^3(\vec{k}-\vec{k}') \quad (2.33)$$

$$\left[b(\vec{k}), b^\dagger(\vec{k}')\right] = 2k^0\delta^3(\vec{k}-\vec{k}') \quad (2.34)$$

These operators $a^\dagger(\vec{k})$ and $a(\vec{k})$ can be interpreted as creation and annihilation operators, just like for the harmonic oscillator. They act on the ground state (vacuum) as follows:

$$\begin{aligned} a(\vec{k})|0\rangle = b(\vec{k})|0\rangle &= 0 \\ a^\dagger(\vec{k})|0\rangle &= |a(\vec{k}\rangle) \\ b^\dagger(\vec{k})|0\rangle &= |b(\vec{k}\rangle) \end{aligned}$$

So the quantized field acts on the vacuum by creating a particle or destroying an anti-particle (the conjugated one the opposite). To estimate the evolution of a field, the commutator $\Phi(x)$ with $\Phi^\dagger(x')$ and $\Pi(x')$ (especially for different times) has to be computed :

$$\Delta_F(x-x') := -i\left\langle 0\left|\mathbf{T}\left[\Phi(x), \Phi^\dagger(x')\right]\right|0\right\rangle. \quad (2.35)$$

T is the symbol of the time ordered product, depending on the time variable of the fields. It obeys the law "late goes left", meaning that the state later in space-time is on the left side of the commutator. Setting in the fields Φ and $\Phi^\dagger$ and computing the residual integral, one gets:

$$\Delta_F(k) = \frac{1}{k^2 - m^2 + i\epsilon}, \quad (2.36)$$

which is the Feynman-Propagator for Klein-Gordon fields and contains the information of the evolution of the field. The propagators are used in Feynman graphs to describe virtual particles as e.g. gauge bosons.

2.1.6 The Drell-Yan process

This study will concentrate on di-muon pairs originating from the Drell-Yan process. The process $p + p \rightarrow \mu^+\mu^- + X$ can be mediated by a photon γ as well as by a Z^0 Boson. For simplicity, only the photon mediation will be taken into the calculation as shown in Figure 2.3. Following the Feynman rules for QED, the matrix element of this process assumes the form:

$$-iM = iQ_j\frac{e^2}{q^2}\left[\bar{\nu}(p_2)\gamma^\mu u(p_1)\right]\left[\bar{u}(p_3)\gamma_\mu\nu(p_4)\right]. \quad (2.37)$$

The matrix element has to be squared and averaged over spin and color:

$$|\bar{M^2}| = \left(\frac{1}{2}\right)^2 3\left(\frac{1}{3}\right)^2 Q_j^2\frac{e^4}{q^4}Tr[\not{p_2}\gamma^\mu\not{p_1}\gamma^\nu]Tr[\not{p_3}\gamma_\mu\not{p_4}\gamma_\nu]. \quad (2.38)$$

Here the Feynman notation of $\not{p} = \gamma^\mu p_\mu$ has been used for the four momenta of the interacting particles and Tr denotes that the traces of the matrices have to be calculated. The cross section which is related to the matrix element is defined by:

$$d\sigma = \frac{1}{2\hat{s}}|\bar{M^2}|\frac{d\cos(\theta)}{16\pi}. \quad (2.39)$$

The cross section of this process is then of the form:

$$\frac{d\sigma(q_j\hat{q}_j \rightarrow \mu^+\mu^-)}{d\cos(\theta)} = Q_j^2\alpha^2\frac{\pi}{6}\frac{1}{\hat{s}}\left(1+\cos^2(\theta)\right) \quad (2.40)$$

$$\sigma(q_j\hat{q}_j \rightarrow \mu^+\mu^-) = Q_j^2\frac{4\pi\alpha^2}{9\hat{s}} \quad (2.41)$$

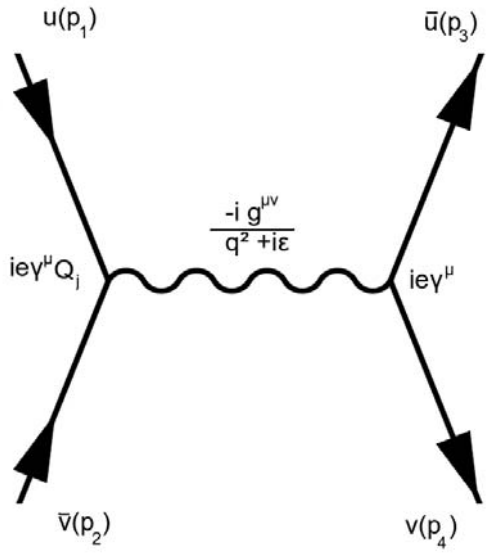

Figure 2.3: Incoming quark and anti-quark annihilating into a lepton pair mediated by a virtual photon.

The total cross section σ is obtained by computing the integral

$$\sigma = \sum_{i,j} \int \hat{\sigma}_{ij}(\hat{s}) d\hat{s} \int_0^1 dx_1 \int_0^1 dx_2 \, f_i(Q^2, x_1) f_j(Q^2, x_2) \delta(\hat{s} - x_1 x_2 s). \tag{2.42}$$

Here, $f(Q^2, x)$ is the parton distribution function and gives the probability of an interaction with a parton with the fractional energy x at the energy scale Q. $\hat{s}$ is the centre of mass energy of the collision, Q_j is the fractional charge of the quarks (for leptons $Q_j = 1$), and θ the decay angle which gives the angular distribution of the final state particles.

2.1.7 Shortcomings of the Standard Model

The Standard Model makes precise predictions of particles' interactions. However there are still several problems that the SM is not able to solve. The most prominent ones are listed below:

- **Neutrino mass**
  From neutrino experiments it is known that due to oscillations of the flavor neutrinos need to have a non-vanishing mass. In the theory of electroweak interactions masses of neutrinos are not foreseen as this mass term would connect the left- and right-handed states. As right-handed neutrinos are not contained in the electroweak theory, these masses cannot be described with the SM.

- **Unification**
  The Standard Model is based on different gauge groups with different coupling constants. A theory which unifies all these gauge groups as subgroups of a unified theory is the aim of the so called Grand Unified Theory GUT. In the SM this unification is not possible as the coupling strengths of the electroweak and strong interaction do **not** unify at a certain energy scale.

- **Problem of Hierarchy and Fine-tuning**
  One known interaction is not addressed by the Standard Model at all, the gravitational force. For low energies, gravity does not play a role. For example the ratio of (Newtonian)

gravitation and electromagnetic force of two electrons in an arbitrary distance r is (for low energies the running of the coupling α_{QED} has not to be considered):

$$\frac{F_{grav}}{F_{el}} = 10^{-40}. \tag{2.43}$$

The apparent weakness of the gravitational force is not yet understood. This is called the hierarchy problem. Another very close issue is the problem of **fine-tuning**. The Higgs-Mechanism predicts the mass of the Higgs boson to be of the order of the vacuum expectation value of $v = \sqrt{\frac{\mu}{\lambda}} = 246\,\text{GeV}$. Computing the $t\bar{t}$ one-loop corrections (Figure 2.4) of the Higgs mass, the *effective* mass (the one which is measured) of the Higgs boson has the form:

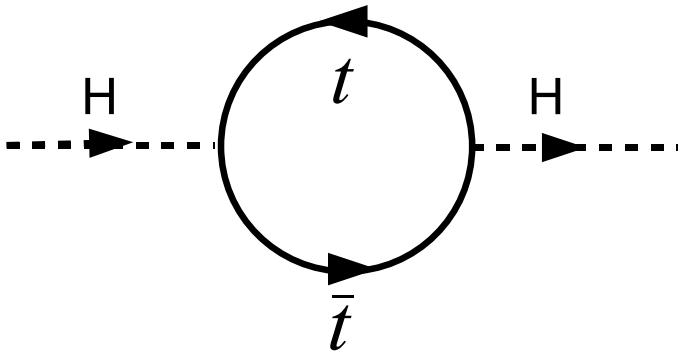

Figure 2.4: $t\bar{t}$ -loop correction to the Higgs mass.

$$m^2_{H,bare} = m^2_{H,eff} + \frac{\lambda_f^2}{8\pi^2}\Lambda^2 - \mathcal{O}(\log(\lambda^2))... + h.c. \tag{2.44}$$

where λ_f is the self coupling constant of the higgs bosons and Λ the cut-off scale up to where the SM is believed to be valid [4]. Gravity itself is supposed to become strong at scales where the Compton wavelength λ_C (the characteristic value of quantum effects) and Schwarzschild-radius r_s are of the same magnitude:

$$\begin{aligned} \lambda_C &= r_s \\ \frac{2Gm}{c^2} &= \frac{h}{mc} \\ M_{Planck} \approx \sqrt{\frac{c\hbar}{G}} &= \frac{1}{\sqrt{G}} \approx 10^{19}\,\text{GeV}. \end{aligned}$$

Defining the Planck scale M_{Planck} as cut-off of the SM, the effective mass of the Higgs boson has to be fine-tuned down the the electroweak scale M_{EW}, where the mass of the Higgs is expected. This tuning has to be done for $(\Lambda/M_{EW})^2 = 10^{32}$ orders of magnitude. This is not only an aesthetic problem but also a technical one, as huge hierarchies in nature tend to collapse.

[4] The integral of the loop amplitude $\int^{\Lambda} \frac{d^4k}{2\pi k^2}$ has to be evaluated at the cut-off scale.

2.2 Theory of Extra Spatial Dimensions

In collider experiments like the ones at LEP the SM has been tested at distances down to 10^{-18} m. For gravity this has never been possible as the necessary energies could not be supplied up to now. The distances down to which gravity has been tested are in the sub-millimeter range. Below the sub-millimeter scale there is no knowledge about gravity at all. This is the motivation of the recent theories of Large Extra Dimensions (LED).

2.2.1 Kaluza Klein Theory of Extra Dimensions

Shortly after the formulation of general relativity by Albert Einstein in 1915, the physicists Theodor Kaluza and Oskar Klein figured out that it is possible to unify general gravity with electromagnetism, which is described by a $\mathbf{U}(1)$ symmetry group, by postulating one additional spatial dimension [7]. This dimension in the Kaluza-Klein-Theory has to be cylindrically compactified with radius R in order to be consistent with known observations, e.g. Newton's law of gravity. Describing both, electromagnetism and gravity, the theory of Kaluza and Klein made following ansatz for the metric tensor with the scalar field ϕ, which is the so-called "dilaton"-field and the vector field A_μ of electromagnetism (Here I, J are used for the coordinates in the whole space, the four standard dimensions plus the extra spatial dimensions. The indices $^{(4,5,6\ldots D)}$ with $D = 3 + 1 + n$, are used to indicate the number of dimensions, where n is the number of extra dimensions):

$$g_{IJ}^{(5)} = \begin{pmatrix} g_{\mu\nu}^{(4)} + \phi^2 A_\mu A_\nu & \phi A_\mu \\ \phi A_\nu & \phi^2 \end{pmatrix} \tag{2.45}$$

Using this tensor, the Maxwell equations of electromagnetism and general relativity can be derived simultaneously. This tensor leads to the infinitesimal line element

$$ds^2 = g_{\mu\nu} dx^\mu dx^\nu + \phi^2 (A_\nu dx^\nu + dy)^2, \tag{2.46}$$

where y represents the coordinate in the extra spatial dimension. As already mentioned, the extra dimension in direction of y has to be compactified with the boundary condition $\phi(x^\mu, y) = \phi(x^\mu, y + 2\pi R)$. This can be used and a Fourier-expansion of the fields can be performed [8]:

$$g_{\mu,\nu}(x^\mu, y) = \sum_{\alpha=-\infty}^{\alpha=\infty} g_{\mu\nu} e^{i\alpha \frac{y}{R}}, \tag{2.47}$$

$$A_\mu(x^\mu, y) = \sum_{\alpha=-\infty}^{\alpha=\infty} A_\mu e^{i\alpha \frac{y}{R}}, \tag{2.48}$$

$$\phi(x^\mu, y) = \sum_{\alpha=-\infty}^{\alpha=\infty} \phi(x^\mu) e^{i\alpha \frac{y}{R}}. \tag{2.49}$$

In order to obtain the equations of motion, the Klein-Gordon equation can be calculated for the (massless) [5] scalar field in extra dimensions

$$^{(D)}\partial_J \partial^J \phi = 0, \tag{2.50}$$

$$(^{(4)}\partial_\mu \partial^\mu + \partial_y^2)\phi = 0, \tag{2.51}$$

$$(^{(4)}\partial_\mu \partial^\mu + \frac{\alpha^2}{R^2})\phi = 0. \tag{2.52}$$

Comparing the last equation with the Klein-Gordon equation with a mass term, one sees that extra dimensions lead to effective masses of the considered field:

$$m_\alpha^2 = \left| \frac{\alpha^2}{R^2} \right|. \tag{2.53}$$

[5] For illustration a massless scalar field is totally adequate and can easily be generalized to vector or tensor fields with masses. In that case the additional mass is just summed with the conventional one.

So in a higher dimensional theory fields gain an (additional) effective mass for lower dimensional subspaces, called Kaluza-Klein (KK) modes. The zero-th mode of the Fourier series can be identified with the conventional field. This is illustrated in the simplified Figure 2.5.

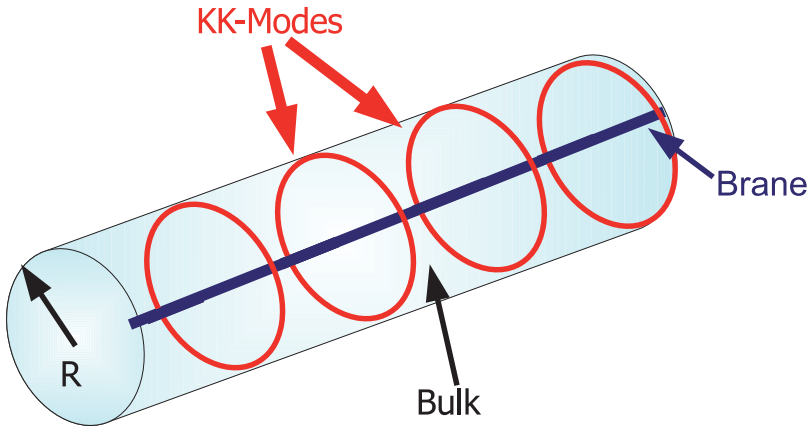

Figure 2.5: Illustration of cylindrical extra spatial dimension with radius R and resulting KK-modes.

2.2.2 Renaissance of Extra Dimensions, the ADD Model

With the upcoming quantum theory and its precise predictions of new phenomena, the theory of Kaluza and Klein has not been developed further. Also the fact that the scalar field ϕ in the metric above did not conserve the chirality of massless particles disfavored this theory [9]. Then in 1998 **A**rkani-Hamed, Savas **D**imopoulos and Gia **D**vali [10] proposed the ADD model of Large Extra Dimensions. They introduced n extra spatial dimensions with a compactification radius of R as shown in Figure 2.5. The extra dimensions, are fully accessible for gravitation only whereas the SM particles are confined to the three dimensional subspace, the so-called brane. The whole space, called the bulk, contains the brane and the extra dimensions). In distinction to the other known three interactions (QED, QFD, QCD) gravity does not couple to any charge, but is a more general interaction and couples to all forms of energy itself. So gravitation can propagate into the LED due the energy of the extra dimensions. For the D-dimensional space-time the Newtonian gravitation can be calculated with the Poisson equation

$$\Delta V_D = -4\pi G_D \rho_m \quad \text{with the mass density} \quad \rho_m = M\delta(\vec{r}) \quad \text{and} \quad G_D = \frac{1}{M_S^{2+n}}. \tag{2.54}$$

M_S represents the counterpart of the Planck scale for higher dimensional theories. Using Gauss' law

$$\int_V \nabla\Phi \, \mathrm{d}V = \int_{\partial V} \Phi \, \mathrm{d}\vec{S} \tag{2.55}$$

to transform the volume integral into a surface integral, the equation assumes the form:

$$\int_{\partial V} \nabla V_D d\vec{S} = 4\pi G_D M. \tag{2.56}$$

This integral has to be computed with D-dimensional spherical coordinates. Thereby the gravitational potential in D dimensions can be written as:

$$V_D(r) = -\frac{2\Gamma\left(\frac{2+D}{2}\right) G_D M}{(1+D)\pi^{D/2} r^{1+D}}, \tag{2.57}$$

with the surface of the z-dimensional sphere $\Gamma(z)$. Considering the compactification of the n LEDs, the potential can be expanded into two asymptotic solutions:

$$V_D \approx \begin{cases} -\frac{G_D M}{\pi r^{n+1}} & r < R, \\ -\frac{G_D M}{2\pi r R^n}\left(1 + 2e^{-\frac{R}{r}}\right) & r \gg R. \end{cases} \tag{2.58}$$

The extra dimensional gravitation spreads like r^{n+1} for distances smaller than the radius R, as it is propagating also into extra dimensions at that ranges, shown in Figure 2.6.

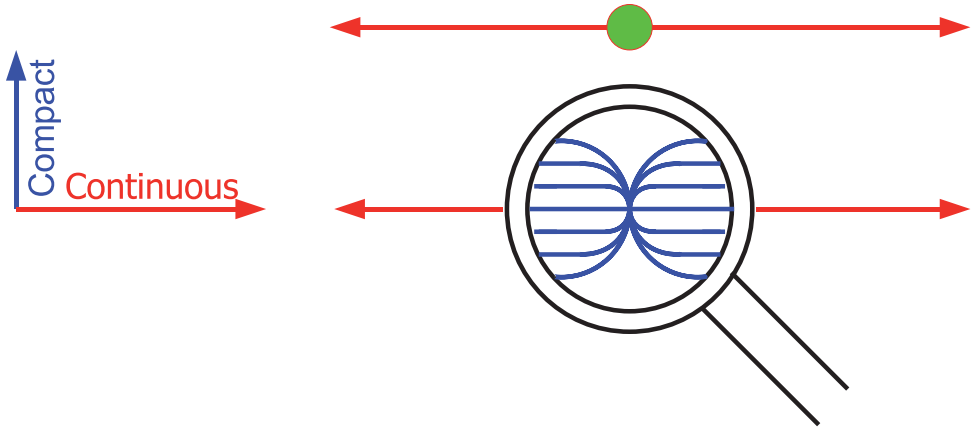

Figure 2.6: The one-dimensional field of a particle has a different spatial dependency for distances smaller than the compactification radius R.

Also for large distances the formula has another form than the Newtonian gravitation $V(r) = -\frac{GM}{r}$. As the behavior of gravity at macroscopic distances is known from experiments, the last equation must be related to Newtonian gravity:

$$\lim_{r \gg R} V_D(r) \stackrel{!}{=} V(r), \tag{2.59}$$

$$G_D \frac{1}{2\pi R^n} = G. \tag{2.60}$$

By comparison the relation of the lowered fundamental scale M_S and the Planck scale M_{Planck} is calculated as follows:

$$M_S^{2+n} R^n \approx M_{Planck}^2. \tag{2.61}$$

So if M_S is actually of the same magnitude as e.g. the electroweak scale (instead of 10^{19} GeV), no fine-tuning of the higgs mass will be required anymore. From Equation 2.61 the compactification radii of extra dimensions for the lowered fundamental scale of $M_S = 1$ TeV can be calculated. For up to four extra dimensions the values for R are listed in Table 2.1.

n	1	2	3	4
R [m]	10^{12}	10^{-4}	10^{-9}	10^{-12}

Table 2.1: Size of the LEDs for $M_S = 1$ TeV.

Except for the case of $n = 1$ which would have been observed already the cases $n > 1$ still have to be tested further [6].

To obtain a quantum theory of LED two pieces have to be calculated: First, the energy scales of the bulk and the brane action have to be matched to determine the strengths of the higher dimensional couplings. Second, an effective Lagrangian of higher dimensional gravity has to be formulated to be able to calculate the couplings.

[6] There are some results from collider experiments for up to 6 EDs. They will be described in the next chapter.

2.2.3 Matching the ADD theory to the $3+1$-dimensional world

As the EDs are supposed to be compactified and only accessible for the graviton, the Einstein-Hilbert action of the ADD theory has to be investigated. The action can be split into the brane and the bulk part.

$$S = S_{\text{brane}} + S_{\text{bulk}}. \tag{2.62}$$

Naturally the bulk consists of the extra dimensions **and** the brane. As the SM is confined to the brane an effective formulation of the brane phenomena is desired. The Einstein-Hilbert action in 4 dimensions for gravitation is:

$$S = d^4x \int \mathcal{L}, \tag{2.63}$$

$$S^{(4)} = -M^2_{Planck} \int d^4x \sqrt{g^{(4)}} R^{(4)}, \tag{2.64}$$

with the Planck constant M^2_{Planck}, the curvature $R^{(4)}$ (which originates from the contraction of the Ricci Fields), and the Minkowski metric tensor in four dimensions $g^{(4)}$. This can be generalized to a higher dimensional theory:

$$S^{(4+n)} = -M_S^{n+2} \int d^{4+n}x \sqrt{g^{(4+n)}} R^{(4+n)}. \tag{2.65}$$

In order to compare these formulae, another assumption has to be made. Let the space-time be nearly flat, so that $g_{\mu\nu}$ can be expanded in a Taylor series:

$$g_{\mu\nu} = \eta_{\mu\nu} + h_{\mu\nu}, \tag{2.66}$$

$$\Rightarrow ds^2 = (\eta_{\mu\nu} + h_{\mu\nu}) dx^\mu dx^\nu - r^2 d\Omega^2_{(n)}, \tag{2.67}$$

where $d\Omega_{(n)}$ are the spherical coordinates of the extra dimensions [11] and $\eta_{\mu\nu}$ represents the totally flat Minkowski metric whereas $h_{\mu\nu}$ is a four dimensional fluctuation around $\eta_{\mu\nu}$. From these constraints the relation between the high dimensional action $S^{(4+n)}$ and the action in four dimensions $S^{(4)}$ is determined and gives the relations of the determinants of the metric g and scalar curvatures R as:

$$\sqrt{g^{(4+n)}} = r^n \sqrt{g^{(4)}}, \tag{2.68}$$

$$R^{(4+n)} = R^{(4)}. \tag{2.69}$$

Here r is the compactification radius of the LEDs to avoid confusion with the curvature R. Using this relation again in $S^{(4+n)}$ the connection between the EDs and the four dimensions assumes the form:

$$S^{(4+n)} = -M_S^{n+2} \int d^{4+n}x \sqrt{g^{(4+n)}} R^{(4+n)} \tag{2.70}$$

$$= -M_S^{n+2} \int d^4x \int d\Omega_{(n)} r^n \sqrt{g^{(4)}} R^{(4)} \tag{2.71}$$

$$= -M_S^{n+2} (2\pi r)^n \int d^4x \sqrt{g^{(4)}} R^{(4)}. \tag{2.72}$$

Matching the coefficient of the above action with the Planck scale M_{Planck}, the fundamental equation of LEDs can be written as (compare to Equation 2.61):

$$M_S^{2+n} R^n \approx M^2_{Planck}, \tag{2.73}$$

where R has been used as the radius of the EDs. This equation shows the essence of this higher dimensional theory. The measured Planck scale M_{Planck} is a derived value of the lowered fundamental scale M_S and the radius of the EDs. The formula above can be derived from geometric constrains by comparing the higher dimensional field with the Newtonian one, as shown in Equation 2.61, but explains also the connection of coefficients in the $4+n$ and four-dimensional theory.

2.2.4 Phenomenology of Extra Dimensional Gravity coupling to the SM

The bulk action in the previous section has been calculated under the assumption of a nearly flat space-time. These fluctuations have to be taken into account to describe the action on the brane, as the brane action is important for the confined SM. Let the bulk coordinate be X^M $(M = 0...D)$, and the position on the extra dimensional bulk (excluding the brane) by $x_m, (m = 4...D)$. To emphasize the position of the brane in the bulk the coordinate Y^M is used.

As only bulk fluctuations are relevant for this theory to describe couplings on the brane, the introduction of the **induced** metric is needed:

$$g_{\mu\nu} = G_{MN}\partial_\mu Y_m \partial_\nu Y_m, \tag{2.74}$$

with the corresponding infinitesimal line element:

$$d^2s = g_{IJ}dY^I dY^J. \tag{2.75}$$

The brane fluctuations can be set to zero by demanding $Y^I = \delta^\mu_\nu x^\mu$. The brane action is then given by:

$$S = \int d^4x\sqrt{g}\mathcal{L}_{SM}(g_{\mu\nu}, \phi, A_\mu...) \tag{2.76}$$

Expanding S around the flat induced metric:

$$S_{SM} = \int d^4x\mathcal{L}_{SM} + \int d^4x \frac{\delta S_{SM}}{\delta g_{\mu\nu}}|_{g=\eta}\delta g_{\mu\nu}(x) + ... \tag{2.77}$$

with

$$\delta g_{\mu\nu}(x) = \frac{1}{M_S^{n/2+1}}G_{\mu\nu}(x)\ , \qquad G_{\mu\nu}(x) : \text{superposition of KK modes.} \tag{2.78}$$

Here it can be seen that the fluctuations of the bulk which have an impact on the brane action are superpositions of KK graviton tensor fields. So in the ADD theory the fluctuations $h_{\mu\nu}$ are identified with the KK tensor fields. Further the energy-momentum-tensor of the Standard Model $T^{\mu\nu}_{SM}$ can be written as:

$$T^{\mu\nu}_{SM} = |g|^{-\frac{1}{2}}\frac{\delta S_{SM}}{\delta g_{\mu\nu}}. \tag{2.79}$$

Remembering that G_{IJ} can be expanded like

$$G_{I,J}(x^\mu, y) = \sum_{\alpha=-\infty}^{\alpha=\infty} g_{\mu\nu}e^{i\alpha\frac{y}{R}}, \tag{2.80}$$

the action assumes the final form :

$$S = -\frac{1}{M_{Planck}}\int d^4x \sum_\alpha G^\alpha_{\mu\nu}T^{\mu\nu}. \tag{2.81}$$

So it is obvious that the bulk graviton couples linearly to SM matter with the coupling strength:

$$\mathcal{L}_{grav} = -\frac{1}{M_{Planck}}\sum_\alpha G^\alpha_{\mu\nu}T^{\mu\nu}. \tag{2.82}$$

Every KK mode couples to SM matter very weakly with $1/M_{Planck}$. The couplings are determined by the energy-momentum-tensor of the SM and the KK mode. The virtual graviton process valid for LHC collisions will be discussed in the next chapter.

Chapter 3

Experimental probes of Models with LEDs

To prove the existence of LEDs (as predicted in the ADD model), several experiments have been performed over the last ten years. In this chapter the three most important ones are listed.

3.1 Tabletop Experiments of the Inverse-Square Law

The Eöt-Wash Group [12] of Washington University has specialized (using new techniques) in high-precision studies of weak-field gravity at short ranges [13]. The torsion-balance instrument, shown in Figure 3.1, consists of a torsion-pendulum detector suspended by a thin 80 cm long Tungsten fiber. The pendulum is positioned above an attractor that rotates with a uniform angular velocity ω by a geared-down stepper motor. The detector's 42 test bodies are formed as (4.767 mm diameter) cylindrical holes machined into a (0.997 mm thick) Molybdenum detector ring. The gravitational interaction between the attractor holes and the masses of the detector apply a torque on the detector which can be measured by an oscillation with an autocollimator system [14].

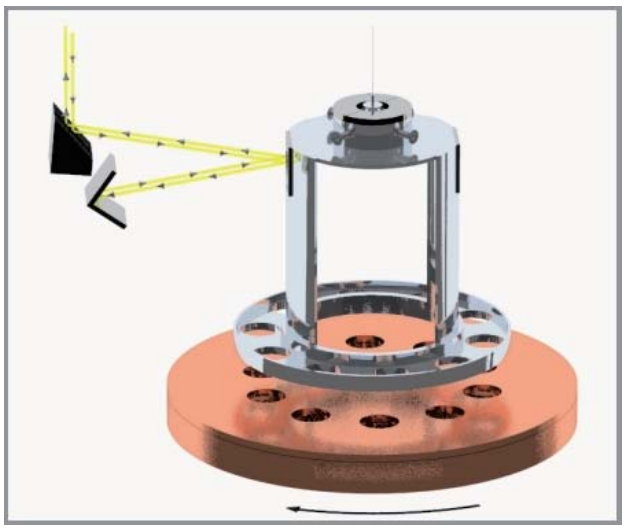

Figure 3.1: Torsion pendulum used by the Eöt-Wash group to measure deviations from the Newtonian gravity law [13].

The interaction is parametrized by a Yukawa-interaction:

$$V(r) = -G\frac{m_1 m_2}{r}\left[1 + \alpha e^{(-r/\lambda)}\right]. \tag{3.1}$$

With a 95 % confidence level the Eöt-Wash group measured that the Newtonian gravity holds to a length scale of $\lambda = 56\,\mu$m so that the compactification radii of LEDs have to be smaller than R= 44 μm shown in Figure 3.2.

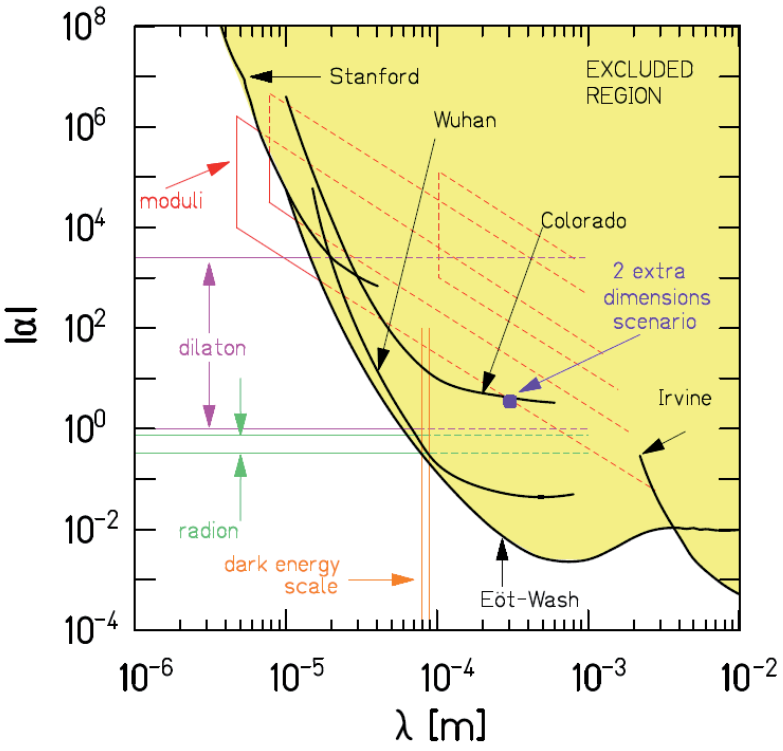

Figure 3.2: Exclusion limits (95% CL) obtained by the Eöt-Wash Group [12]. The parameter α for LED is set to $\alpha = \frac{8}{3}$ which is determined by comparision with Yukawa-interaction.

3.2 Cosmological Constraints

In supernovae the theoretical energy losses due to emissions of gravitons can be used to derive a limit on the lowered fundamental scale M_S [15]. A supernova cools faster if it emits gravitons compared to the cooling without the emission of gravitons, as the normal cooling process is due to the emission of neutrinos. For the temperature $T < R^{-1}$ smaller than the compactification radius no KK modes can be produced, but if $T > R^{-1}$ a large number of KK modes are excited in the supernova. The number $\mathrm{N_{KK}}$ of produced KK modes can be written as:

$$\mathrm{N_{KK}} \sim (T \cdot R)^n. \tag{3.2}$$

As each mode couples with $1/M_{Planck}$, the cooling is expressed using Equation 2.61:

$$\mathrm{N_{KK}} \sim \frac{1}{M_{Planck}}(T \cdot R)^n \approx \frac{T^n}{M_S^{n+2}}. \tag{3.3}$$

Rearranging this equation a limit on M_S can be calculated by measuring the cooling temperature. Due to the measurement of the γ-ray background created by the radiative decays of the KK modes (KK Mode $\rightarrow \gamma\gamma$) of the supernova SN1987A at EGRET (Energetic Gamma Ray Experiment Telescope) in the year 1987, it has been possible to state lower limits for the fundamental scale. The results are listed in Table 3.1.

As there have been huge systematical uncertainties on the knowledge of the core of the supernova, the limits are very sensitive to the fitting procedure which has been used in [15]. E.g. another reasonable fit would lower the limit for $n = 2$ to $M_S = 1\,$TeV.

n	2	3	4
M_S [TeV]	50	4	1

Table 3.1: Exclusion limits from supernova SN1987A cooling with 95% CL [15].

3.3 Collider Physics

The phenomenology of collider processes of theories with ED has been studied exhaustively in [16] and [17]. They have used different conventions in the treatment of the number of extra dimensions and will be called HLZ [16] convention and GRW [17] convention here. There are two main paths in the search for LED at colliders.

- The first one concentrates on the emission of real gravitons schematically shown in Figure 3.3. Due to very weak couplings further interaction of the graviton inside the detector is very improbably. The graviton leaves the detector undetected and creates missing energy in the event. Measuring the missing energy $\not{E}$ of collider events, the production of gravitons can be estimated.

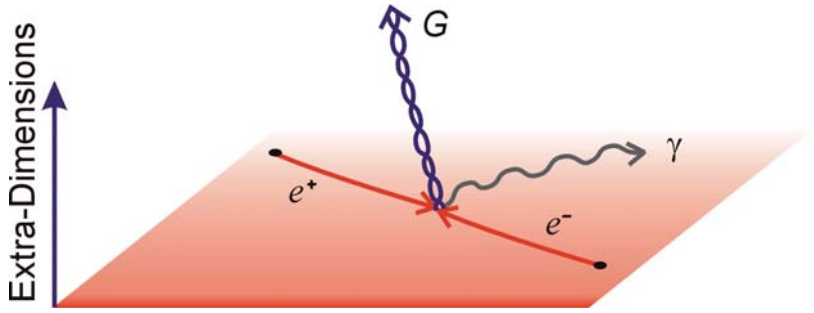

Figure 3.3: Example for the production of real gravitons [8] in e^+e^- scattering.

  Especially for early LHC data where the main challenge will be to properly understand the detector, the analysis of this channel may have difficulties.

- The other attempt is to look for modifications of di-lepton or di-photon cross sections. The virtual graviton contributes to the Drell-Yan process and so more [1] lepton or photon pairs can be produced. The Drell-Yan process has been studied very precisely in theory and therefore is one of the best calculated processes up to NNLO in both, QED and QCD corrections [18, 19, 20], in particle physics. The parametrization of the modified Drell-Yan cross section is as follows:

$$\sigma_{tot}(M_{\mu\mu}, \cos\theta^*) = \sigma_{SM} + \eta\,\sigma_{int} + \eta^2\sigma_{KK}, \tag{3.4}$$

  with $\eta = \frac{F}{M_S^4}$. Here σ_{SM}, σ_{int} and σ_{KK} are the cross sections of the Standard Model, the interference term and the direct Kaluza-Klein graviton coupling, and θ^* is the decay angle of the process and will be described later. The interference process consists of the same initial and final state particles. In Figure 3.4 all possible leading order processes of di-lepton production are shown.

  The factor F depends explicitly on the convention used:

[1] Can also be less, depending on the convention; as only GRW and HLZ are used in this study, the destructive interference is neglected.

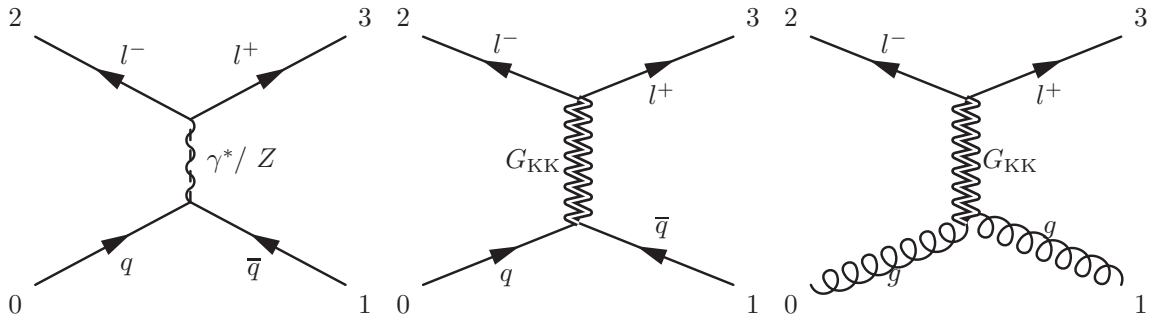

Figure 3.4: Leading order ($2 \to 2$) processes for di-lepton production from hadronic initial states. The first process (virtual γ^*/Z exchange) is occurring in the SM. The second process has the same initial and final state as the SM processes. SM processes and the process $q\bar{q} \to G_{KK} \to l^+l^-$ are not indistinguishable and therefore called interference term. The third process is not included in the SM and only possible with gravitons as intermediate particles.

$$F = \begin{cases} \log\left(\frac{M_S^2}{s}\right) & n = 2 \\ \\ \frac{2}{n-2} & n > 2 \end{cases} \quad \text{(HLZ)} \tag{3.5}$$

$$F = 1 \quad \forall\, n \qquad \text{(GRW)} \tag{3.6}$$

As shown in the previous chapter the graviton can only be described as a tensor field and must therefore be a spin 2 particle. This different spin (as compared to the SM vector bosons) then causes a different angular distribution of the final state particles. So the total cross section of the additional virtual graviton exchange is a function of the invariant di-muon mass and the decay angle θ^*, which is the angle of the positive lepton's momentum w.r.t. the momentum axis of the initial state quark (both quarks are assumed to collide in a head-on collision) in the rest frame of the intermediate particle.

The Feynman rules for graviton couplings have been calculated from its Lagrangian

$$\mathcal{L}_{grav} = -\frac{1}{M_{Planck}} \sum_{\alpha} G^{\alpha}_{\mu\nu} T^{\mu\nu}. \tag{3.7}$$

Here $T_{\mu\nu}$ is the energy-momentum tensor of the SM particle which contains its Hamiltonian $\int \mathrm{d}^3x\, T_{00} = \mathcal{H}$. $G^{\alpha}_{\mu\nu}$ is the α-th Kaluza-Klein graviton mode. So KK gravitons couple to energy in general.

The amplitude of the coupling of the virtual graviton to a SM particle is as follows:

$$A \sim \frac{1}{M^2_{Planck}} \sum_{\alpha} \frac{1}{s - m^2_{\alpha,KK}}. \tag{3.8}$$

The number of excitations is so large that the separation of the masses of the KK-modes is practically not possible. Thus the discrete sum in the Formula above is replaced by an integral over a continuous mass distribution:

$$A \sim \int_0^{\infty} \mathrm{d}m^2_{\alpha,KK}\, \rho(m_{KK})\, \frac{i}{s - m^2_{\alpha,KK} + i\epsilon}, \tag{3.9}$$

where

$$\rho(m_{kk}) = \frac{\pi^{n/2} R^n m^{n-2}_{\alpha,kk}}{\Gamma(n/2)}. \tag{3.10}$$

Here $\Gamma(n)$ is the familiar Gamma function. The cross section of the virtual graviton exchange is proportional to the number of KK modes, so the fundamental scale M_S cannot be measured directly. As the number of KK modes would naturally diverge, the ADD theory is only valid up to a certain cutoff, called M_f. The exact relation of M_S and M_f is not known, but as the fundamental scale of the ADD model is in the range of M_S, it is assumed in phenomenology that these values are of the same order [21].

In addition to the above processes, QCD correction have to be taken into account which means that the initial quarks can emit QCD bremsstrahlung or quark gluon and additional gluon gluon couplings take place. These processes contribute to the Drell-Yan cross section and cannot be neglected. Examples are shown in Figure 3.5.

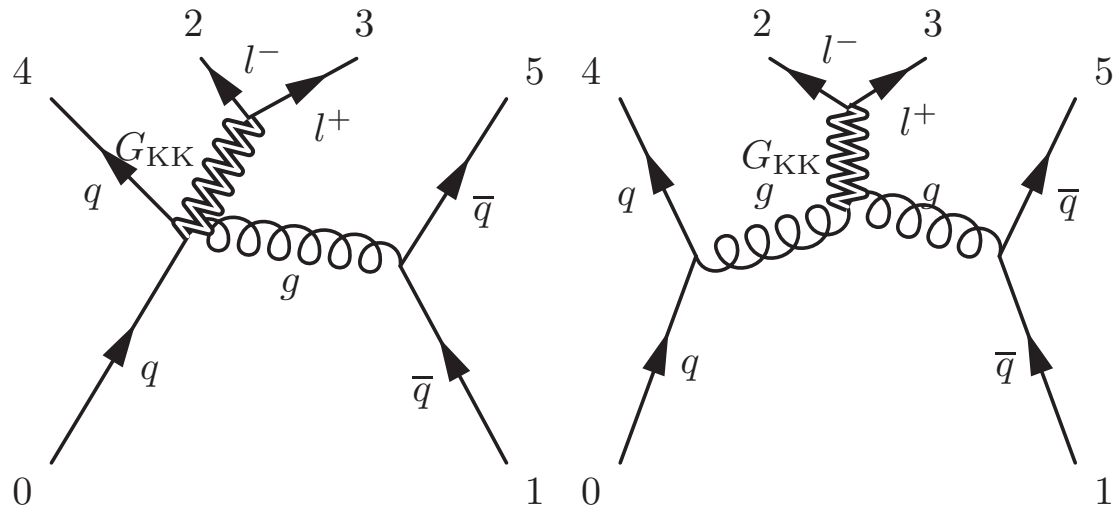

Figure 3.5: Examples for di-lepton production with additional QCD corrections ($2 \rightarrow 4$ processes) with hadronic initial state. The large variety of graviton couplings cannot be neglected and contributes significantly to the cross section.

Virtual graviton exchanges have already been studied in collider experiments. The recent best limits in the Drell-Yan channel for ADD have been set at the D∅-detector at the Tevatron [22, 23] in $p\bar{p}$ collisions at a centre of mass energy of 1.96 TeV, shown in Table 3.2 and Figure 3.6.

Convention	di-muon channel	electromagnetic channel
GRW	1.07 TeV	1.66 TeV

Table 3.2: D∅ limits at 95 % CL for the fundamental scale M_f [22, 23].

In this thesis the analysis will be done with simulated Monte Carlo events of the upcoming LHC data collected with the CMS detector. Due to the significantly higher centre of mass energy it will be possible to probe di-muon events in the **TeV** scale.

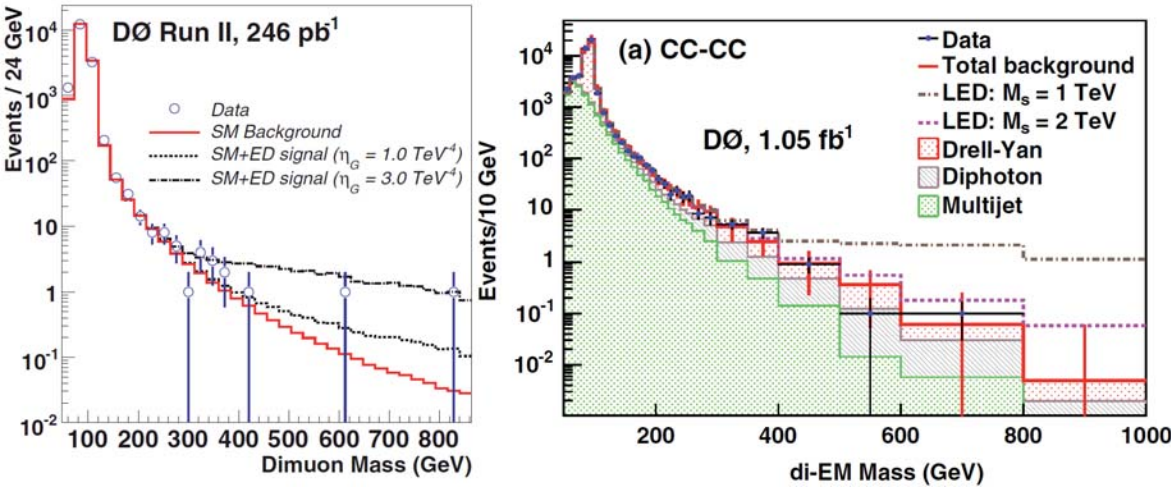

Figure 3.6: Drell-Yan mass distribution for the di-muon channel (left) and the electromagnetic (di-electron and di-photon) (right) at D∅.

Chapter 4

Experimental Setup LHC and CMS

CERN (original name "**C**onseil **E**uropéen pour la **R**echerche **N**ucléaire") is the world's largest particle physics laboratory sited close to Geneva in Switzerland on the border to France shown in Figure 4.1. CERN hosts a large number of accelerators and experiments where accelerated particles are being collided, e.g. at the Large Hadron Collider (LHC).

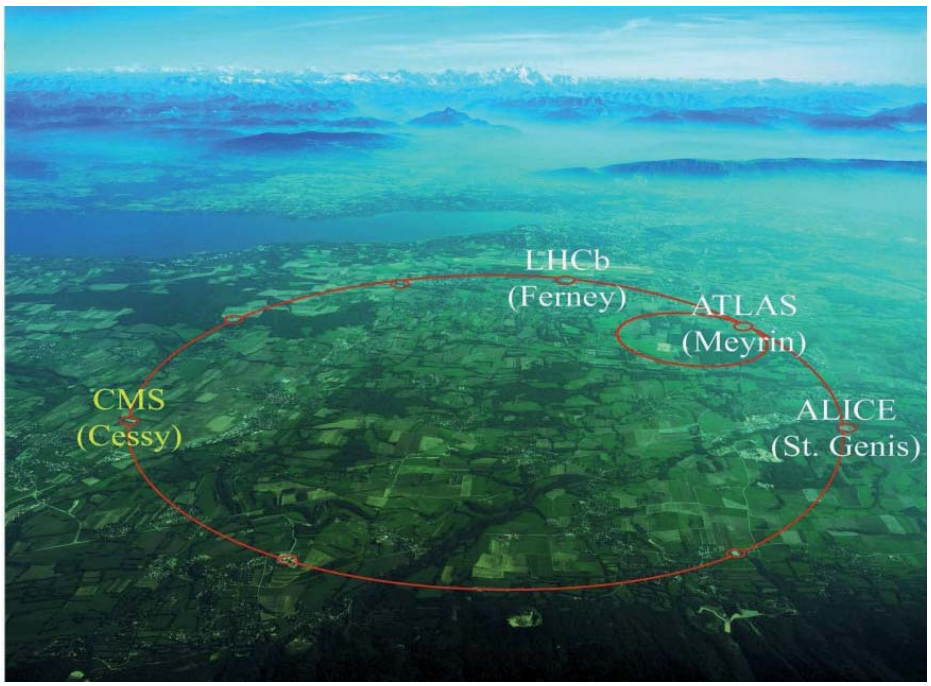

Figure 4.1: LHC design and hosted experiments [24].

4.1 LHC

The Large Hadron Collider (LHC)[25] is a two-ring-superconducting-hadron accelerator and collider installed in the existing 26.7 km tunnel that was constructed between 1984 and 1989 for the CERN LEP machine (Large Electron Positron (Collider)). The LEP ring has been replaced by proton-proton technologies which are now used for the LHC accelerator. It is designed for collisions with a centre of mass energy of 14 TeV, which has never been achieved before in any other experiment. Also the design luminosity (see Equation 4.2) of $10^{34}\,\mathrm{cm}^{-2}\,\mathrm{s}^{-1}$ is much higher as compared to other collider experiments.

It is also planed to accelerate lead ions at LHC in the near future in order to perform heavy ion experiments. There are four main experiments located at LHC. ATLAS[26] and CMS[27] are

both multi-purpose detectors and designed to investigate physics at the Tera-scale. ALICE [28] is a heavy ion experiment and designed to be sensitive to lead nuclei collisions. The LHCb [29] experiment focuses on measurements of quark mixing and CP-violation in the b quark sector. The

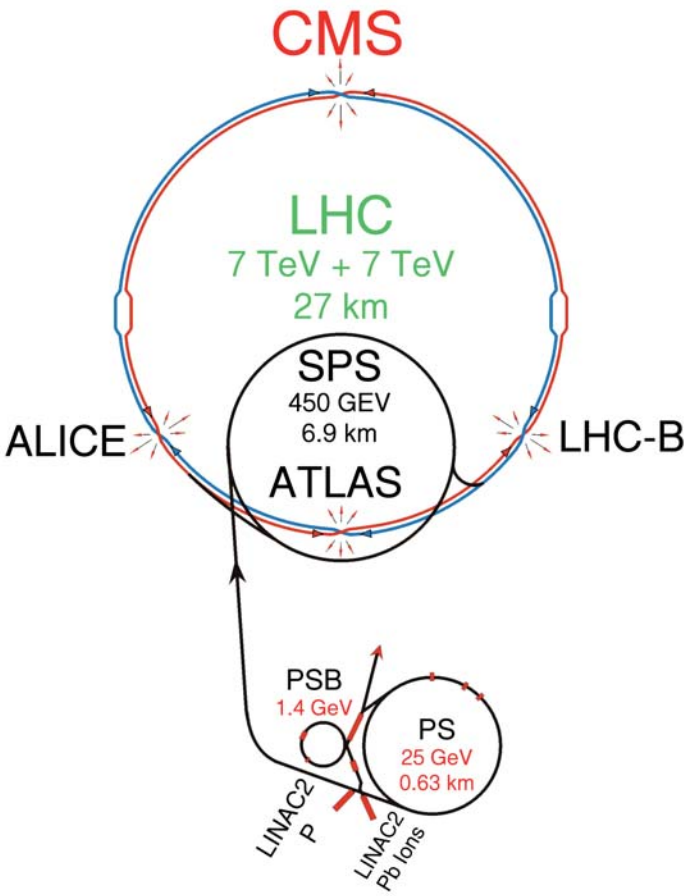

Figure 4.2: Schematic figure of all accelerators at CERN, including the LHC.

whole acceleration procedure is done as follows (Figure 4.2):

Protons are produced by ionizing hydrogen. They are let to the linear accelerator *LINAC2*. The proton bunches delivered by the *LINAC2* are collected in the *Proton Synchrotron Booster* (PSB) and *Proton Synchrotron* (PS) where they are grouped into bunches and later directed to the *Super Proton Synchrotron* (SPS), which is the last pre-accelerator before the bunches reach the LHC, where they are accelerated to their final energy. Taking into account the boundary conditions like pre-accelerators, magnets etc., an optimization procedure has resulted in the LHC proton beam parameters as seen in Table 4.1.

Parameter	Units	**Injection**	**Collision**
Energy	[GeV]	450	7000
Luminosity	[$\mathrm{cm^{-2}s^{-1}}$]		2.5×10^{34}
n_B Number of bunches		2808	
Bunch spacing	[ns]	24.95	
N_B protons per bunch	[p/bunch]	1.7×10^{11}	
Beam current	[A]	0.86	
Energy spread, total (4σ)	10^{-3}	1.9	0.45

Table 4.1: LHC proton beam parameters [24] at design conditions.

To keep the beam on the circle track, dipole magnets are used. They provide a field of 8.4 T. As the two proton beams run in different directions, the magnets need to have different polarities for each beam. The so called *cryodipole* carrying the two proton beams, has a complex design and is also hosting the superfluid helium to cool the magnets down to a temperature of T= 1.9 K, shown in Figure 4.3. Superconducting magnets are used to provide these high magnetic fields.

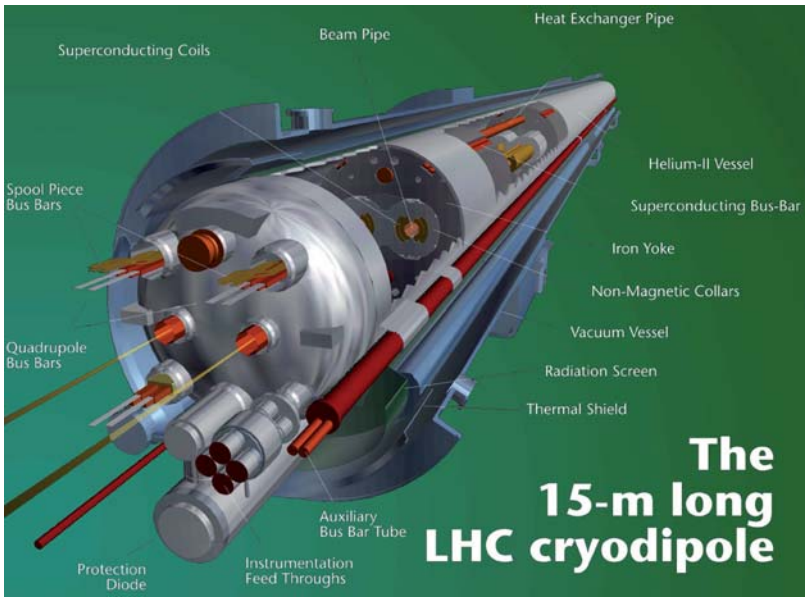

Figure 4.3: Schematic figure of the cryodipole (including the cross section view) carrying the beam pipe [30].

4.1.1 Collider related physics

At colliders the centre of mass energy $\sqrt{s}$ equals $2E$, twice the beam energy of one beam due to frontal collisions of the beams [1]. As previously mentioned besides the centre of mass energy, the luminosity is a characteristic parameter of a collider. With N_B particles per bunch and n_B bunches, the luminosity L is calculated as

$$\mathsf{L} = \frac{n_B N_B^2}{4\pi\sigma_x\sigma_y} \cdot f. \tag{4.1}$$

Here σ_x and σ_y are the Gaussian widths of the beam, and f is the revolution frequency. The relation of event rate and luminosity is given by

$$\dot{N}_{\text{Events}} = \mathsf{L} \cdot \sigma. \tag{4.2}$$

Here σ is the total cross section of the process. Often the total number of events after a certain time t_1 is important to know. The integrated luminosity is given by

$$\int_0^{t_1} \dot{N}_{\text{Events}}(t)\ \mathrm{d}t = \int_0^{t_0} \mathsf{L}(t)\ \mathrm{d}t \cdot \sigma, \tag{4.3}$$

$$N_{\text{Events}} = \mathsf{L}_{int} \cdot \sigma. \tag{4.4}$$

Protons are no elementary [2]particles, but consist of partons. So at high energy collisions at LHC the protons are destroyed and the fractional centre of mass energy called $\hat{s}$, is distributed to

[1] The Mandelstam variable for a two body reaction is: $s = (p_1 + p_2)^2$.

[2] Here the particles of Figure 2.1 are assumed to be elementary, because up to now there is no experimental evidence for them to have inner structure. This will also be probed at LHC.

the constituents:

$$\hat{s} = x_a \cdot x_b \cdot s. \tag{4.5}$$

The $x_{a,b}$ denote the energy fractions of the partons defined as $x_a = \frac{2E_a}{\sqrt{s}}$.

The total cross section of a certain process $pp \to X$ at a centre of mass energy $\sqrt{s}$ can be written as:

$$\sigma = \sum_{i,j} \int \hat{\sigma}_{ij}(\hat{s}) d\hat{s} \int_0^1 dx_1 \int_0^1 dx_2 \, f_i(Q^2, x_1) f_j(Q^2, x_2) \delta(\hat{s} - x_1 x_2 s). \tag{4.6}$$

Here, $f(Q^2, x)$ is the parton distribution function and gives the probability of a parton to interact with the fractional energy x at the energy scale Q.

4.2 CMS

The Compact Muon Solenoid (CMS) [31] is a multi-purpose detector operating at the LHC, CERN. It is consisting of several detector types to detect different types of particles in one apparatus. The main features of the detector are that it is built in a relatively compact way with a length of 21.6 m and a diameter of 14.6 m, and hosts a superconducting solenoid magnet inside.

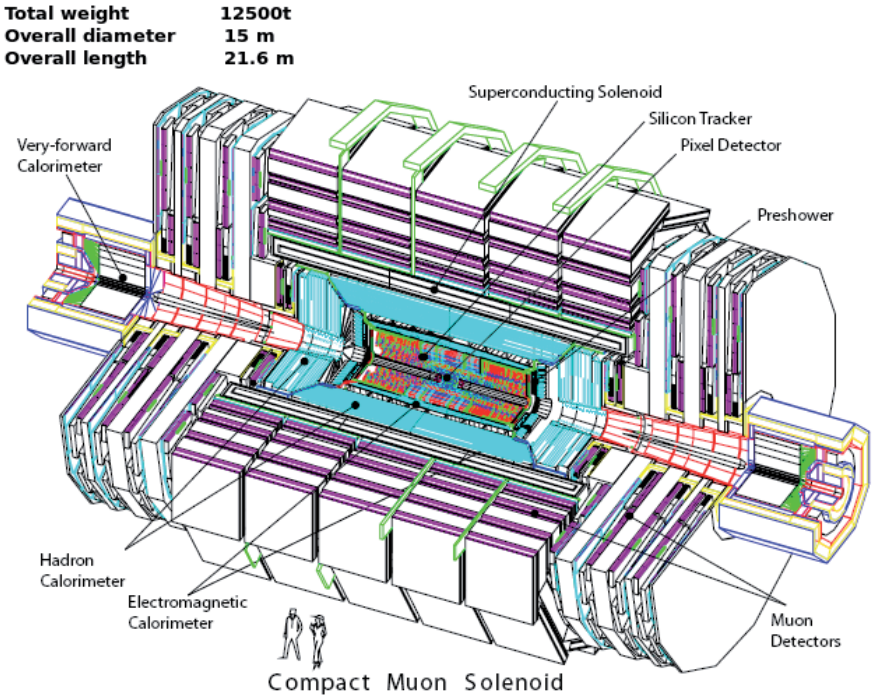

Figure 4.4: A full overview of the CMS detector at LHC [30]. All parts are listed showing both, the endcaps and the barrel region.

The overall structure is shown in Figure 4.4. The most central part of the detector is the 4 T superconducting solenoid, whose coil surrounds the tracker and calorimeter. At the outside of the solenoid the return yoke of the magnet and the muon system are located, consisting of four muon stations. One muon station itself consists of several layers of aluminium drift tubes (DT) in the barrel region, and cathode strip chambers (CSC) in the endcap region, complemented by resistive plate chambers (RPC). All parts will be described briefly.

4.2.1 The Tracker

The CMS tracker is entirely based on silicon detectors [32]. It is surrounding the beam pipe in radial direction and forms the most inner part of the whole detector which is shown in Figure 4.5.

The CMS tracker is composed of 1440 pixel modules and 15 148 strip detector modules. According to the position, the silicon detector size differs $(100 \times 150)\,\mu\text{m}^2$ to $10\,\text{cm} \times 80\,\mu\text{m}$. Also the thickness changes going from $500\,\mu\text{m}$ in the outer tracker region to $320\,\mu\text{m}$ in the inner tracker.

Pixel detector

The silicon pixels [33] consist of highly n-doped implants. The junction to the p-doped area forms a ring structure. The read-out is performed in three parts: a data link to the pixel driver, a fast control link from the pixel driver to the pixel controller and a control link. The granularity of pixels and the high coverage around the interaction point guarantee a resolution of the vertex within an uncertainty of $\sim 10\,\mu\text{m}$. It has been built to provide measurements of primary (immediately after the collision) and secondary (for processes where a short living particle, like b-mesons) vertices. At radii of (4.4, 7.3, and 10.2) cm, three cylindrical layers of pixel detector modules surround the interaction point, and two disks of pixel modules on each endcap side, as shown in Figure 4.5. In

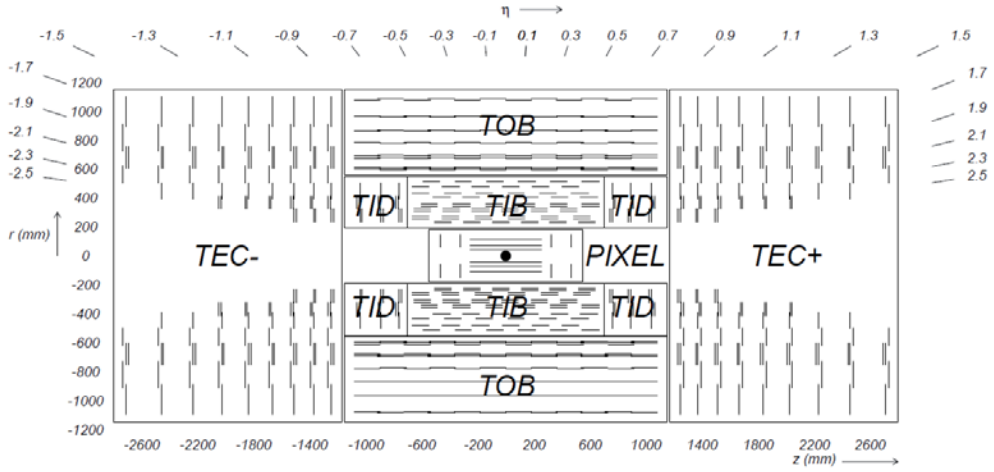

Figure 4.5: The Tracker System [30] of the CMS detector.

total the pixel detector covers an area of about $1\,\text{m}^2$ and consists of 66 million pixel sensors.

Silicon strip tracker

The outer radial region between 20 cm and 116 cm of the tracker system is occupied by the silicon strip tracker, Figure 4.6. It is built of four subsystems (TIB, TID, TOB, TEC). The Tracker Inner Barrel and Disks (TIB/TID) extend radially up to 55 cm and are composed of four barrel layers, supplemented by three disks (endcaps) at each end. The TIB/TID is surrounded by the Tracker Outer Barrel (TOB). It has an outer radius of 116 cm and consists of six barrel layers. The Tracker EndCaps (TEC+ and TEC-) are sited beyond the z axis and cover a larger z region. Overall (as seen in Figure 4.5) the tracker system covers a η-region of 2.5. The silicon strip tracker consists of 15 148 detector sensors implemented in 24 244 modules, covering a total area of $210\,\text{m}^2$. As shown in Figure 4.6 the double sided modules (in blue) consist of two one sided modules (in red) mounted back to back. It is built for precision measurement of tracks [34]. If charged particles cross a silicon sensor as shown in Figure 4.7, electron-hole pairs are produced along the particle trajectory within the n-bulk. The applied electrical field forces the electrons of the bulk to drift to the n^+ layer and the holes to the p^+ implants with a drift time of 10 ns (a typical value for silicon) and can be read out further.

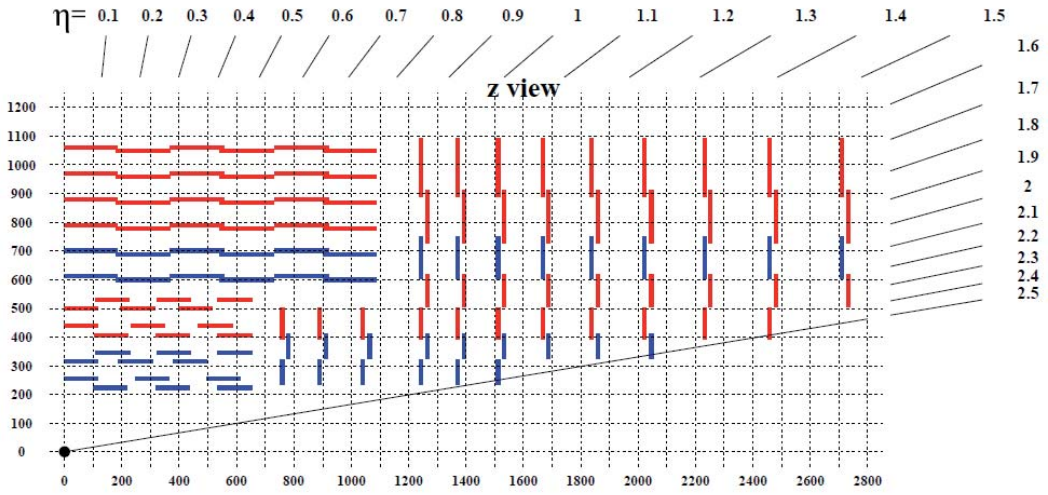

Figure 4.6: Silicon strip tracker system. Shown in red the one sided modules and in blue the double sided modules [30]. The numbers at the edges of the dashed lines represent the value of the pseudorapidity η.

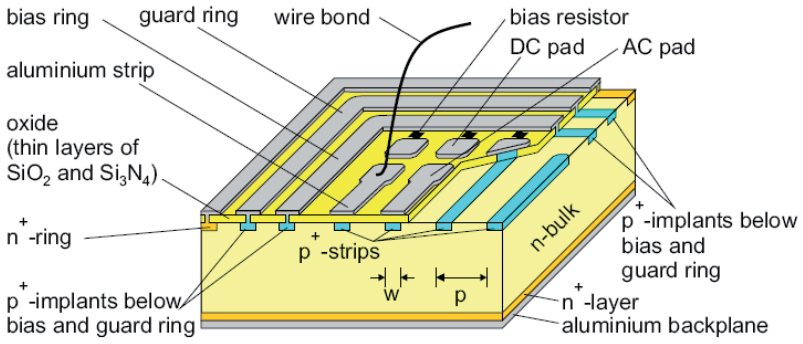

Figure 4.7: Schematic design of a CMS silicon microstrip sensor [34].

The silicon strip detector is operating at $-20°$ C in order to reduce damage from hard radiation. The mechanical accuracy of the tracker adjustment by construction precision [3] is in the range of $50\,\mu$m. This unique detector part in CMS makes it possible to measure the transverse momentum of charged particles with an accuracy of

$$\frac{\sigma(p_t)}{p_t} = 0.15\,\frac{p_t}{\text{TeV}} \oplus 0.5\% \tag{4.7}$$

depending on the energy of the particle [4].

4.2.2 ECAL/HCAL

Calorimeters are detectors to measure the energy of passing particles [35] [36]. In CMS there are two different calorimeter systems used, named ECAL and HCAL. They are positioned inside the solenoid [5] and need to withstand a high radiation level.

[3] No alignment with cosmic data considered here.
[4] Example for muons as can be seen in the Reconstruction chapter.
[5] HCAL HO, the outer calorimeter of the HCAL is positioned outside the solenoid, see next section.

Electromagnetic calorimeter

The electromagnetic Calorimeter (ECAL) is a homogeneous calorimeter, meaning that it is consisting of one material type only. The ECAL is built to measure electrons and photons mostly, which interact electromagnetically in the detector. The measurement of weakly interacting particles is performed with the missing transverse energy.
The ECAL is made of 61 200 lead tungstate ($PbWO_4$) crystals in the barrel part and 7 324 crystals in each of the two endcaps (Figure 4.8). $PbWO_4$ has appropriate characteristics for operations at LHC, a high density of ρ =8.28 g/cm^3, a short radiation length of $X_0 = 0.89$ cm, and a small Molière radius[6] of $R = 2.2$ cm which favor the use of ($PbWO_4$) for the ECAL of the CMS detector.

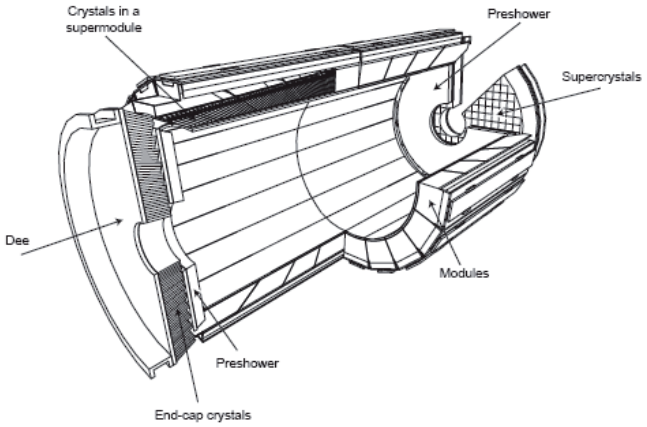

Figure 4.8: The CMS Electromagnetic Calorimeter [34].

The scintillating light of the calorimeter is read out via photodetectors. They have to be radiation tolerant and to be able to operate at a strong magnetic field of 4 T. Two kinds of photodetectors are used in the ECAL. In the barrel region ($|\eta| < 1.479$) avalanche photodiodes are used. They have an excellent quantum efficiency of 75 % for light at a wavelength of 430 nm. In the endcaps ($1.479 < |\eta| < 3$) where the radiation rate is higher, vacuum phototriodes are used, e.g. photomultipliers with a single gain stage [35] [36]. The inferior quantum efficiency of 22 % is compensated by the larger surface coverage of the phototriodes. The CMS ECAL has an expected design energy resolution of:

$$\left(\frac{\Delta E}{E}\right)^2 = \left(\frac{2.8\%}{\sqrt{E}}\right)^2 + \left(\frac{0.12}{E}\right)^2 + (0.3\%)^2. \tag{4.8}$$

HCAL

The CMS Hadron calorimeter (HCAL) is built to measure hadron jets and (indirectly) neutrinos or other particles due to missing transverse energy. The HCAL consists of four parts, the barrel (HB) $|\eta| < 1.3$ and the endcaps (HE) $1.3 < |\eta| < 3.0$, both located inside the solenoid, the outer calorimeters (HO) which is also positioned in the barrel range but outside the solenoid and the forward calorimeter which is located at the very margin of the detector right above the beam pipe covering a range up to $\eta = 5.2$, as shown in Figure 4.9. The CMS HCAL (including the HO) is expected to reach an overall energy resolution of [37]:

$$\left(\frac{\Delta E}{E}\right)^2 = \left(\frac{120\%}{E}\right)^2 + (5\%)^2. \tag{4.9}$$

[6]Radius of a cylinder around the particle trajectory which contains $\sim$ 95 % of the original energy.

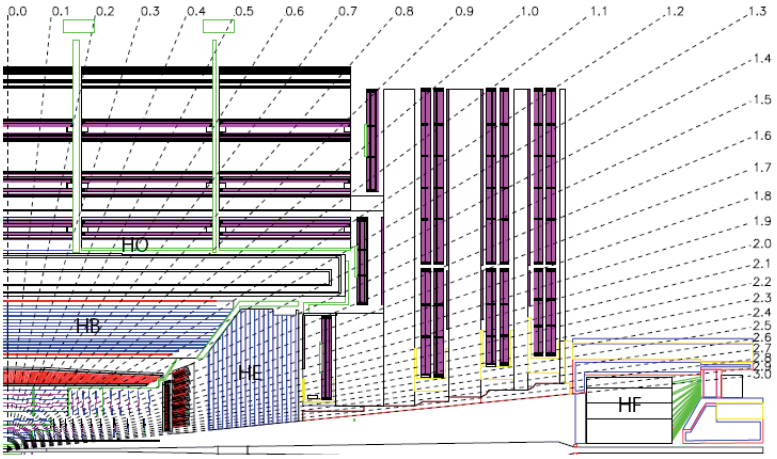

Figure 4.9: The CMS Hadron Calorimeter parts HB, HE, HO and HF, and their η coverage [30] is shown.

Barrel design (HB) and Outer calorimeter design (HO)

The HB is a sampling calorimeter using brass absorber plates (50.0 mm − 56.5 mm thick) to generate hadronic showers and several layers of 3.7 mm thick plastic scintillator tiles with embedded wavelength shifting fibers to collect the emitted light. To ensure sufficient sampling depth for showers that are produced very late in the detector, the barrel region of the HCAL is extended with an additional outer calorimeter (HO) outside of the solenoid. It utilizes the solenoid as absorber material so it consists of plastic scintillators only. The scintillator light is read out via hybrid photodiodes.

Endcap design (HE)

The calorimeter endcaps are positioned at the ends of the solenoid. Non-magnetic brass plates are used as absorbers while 18 layers of trapezoidal-shaped scintillators create light which is read out by hybrid photodiodes.

Forward calorimeter design (HF)

The forward calorimeter is made of radiation tolerant quartz fibers and steel absorbers. The fibers provide fast collection of the Cerenkov light produced in the HF. The Cerenkov light itself is lead to photomultipliers in order to be read out. This construction makes the HF sensitive to the electromagnetic part of the shower.

4.2.3 Muon System

As presented in this thesis the muon final state is very important for the searches of new phenomena. That is why the CMS experiment was built paying attention to the central importance of detecting muons. The tasks of the muon system (Figure 4.10) can be summarized as follows: Identification of the muon, measuring the (transverse) momentum and charge, and triggering. The layout of the muon system [30] [36] is highly influenced by the geometry of the solenoid. So the muon system consists of a cylindrical barrel section $|\eta| < 1.2$ completed by two planar endcaps $0.9 < |\eta| < 2.4$. Three types of detectors are used in the muon system corresponding to the requirements and the positions they are used at.

- Drift tube (DT) chambers are used in the barrel region as the muon rate is low and the magnetic field is weak. Also the background rate generated by neutrons is small. These facts favor the use of DTs.

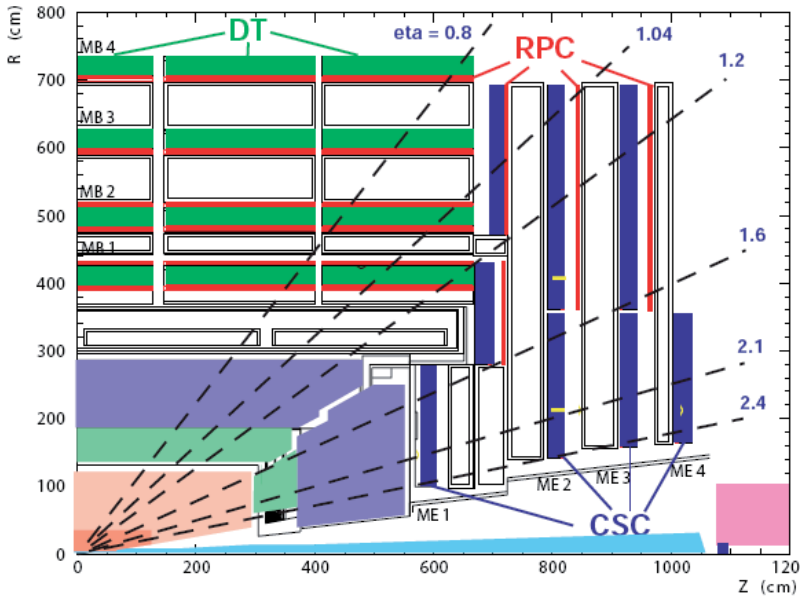

Figure 4.10: The CMS muon system consisting of the barrel and the endcaps [30]. In the barrel region DTs are used whereas CSCs are used in the endcaps to identify muons. Endcaps and barrel are completed with RPCs.

- In the two endcaps where the magnetic field is strong ($|\vec{B}| > 3\,\mathrm{T}$) and non-uniform, and the background rates are high, Cathod Strip Chambers (CSC) are used. With their superior radiation resistance and fast response time, CSCs are more adequate to identify muons in the endcaps. DT and CSC are also capable to trigger an event with muons.
- A much better trigger property is provided by Resistive Plate Chambers (RPC) embedded in both, the barrel region and endcaps. The RPCs provide a fast (a few ns) and independent trigger due to their fast response and good time resolution. The position resolution is coarser as compared to the DT and the CSC.

Drift tube chambers

The functionality of a drift chamber is similar to a wire chamber. Inside a gaseous (CMS DTs use a mixture of 85 % Ar and 15 % CO_2) filled chamber an anode wire is located at which a high potential (+3600 V) is applied where the walls of the chamber have to be grounded or a opposite signed potential has to be appied (-1200 V). The particle passing the DTs ionizes the gas. The electron generated by the ionization move to the anode wire whereas the ions move to the cathode walls. The ionization caused by electrons and ions then is read out as an electric signal. Knowing the drift time (CMS DT 380 ns for 21 mm $\sim$ 55 μm/ns) in the gas a reasonably precise knowledge of the position of the passing particle is acquired. The DT chambers are built concentrically around the beam pipe with growing diameter depending on the distance to the beam. One wheel consists of twelve chambers each covering 30° of the azimuthal angle. A DT chamber is made of three (only two for the last chamber) Superlayers (SL), each consisting of four layers of rectangular drift cells that are shifted by half of a cell, as shown in Figure 4.11. The two outer SL are parallel to the beam direction and measure the track in the plane of the magnetic bending (the $r - \phi$-plane). The SL in the center is rotated by 90° and measures the track in z-direction to provide a 3D measurement.

Not all drift cells in CMS are built with the exact same design. Their scales depend on the type of the SL. The outer width is 42 mm and the height 13 mm whereas the length (direction of the beam pipe) is varying (2.5 m for the r-ϕ-SLs). A traversing particles through a drift cell can be measured with a precision of $\sim$ 200 μm.

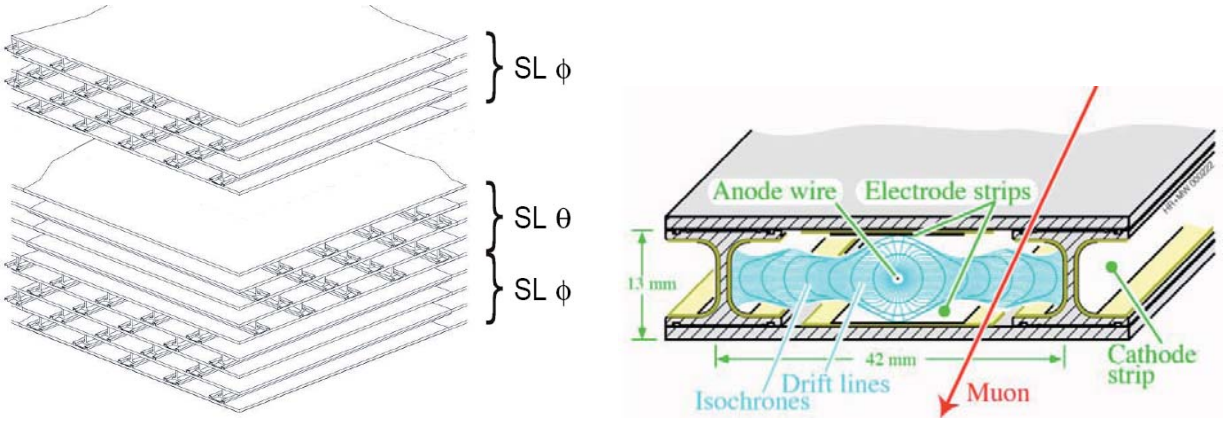

(a) Superlayer (b) Drift cell

Figure 4.11: Superlayer consisting of drift cells (left) and cross section of a drift CMS drift cell (right) [30].

Cathode strip chambers

The CSCs are multiwire proportional chambers made of six anode wire planes and seven cathode strip planes perpendicular to the wires as shown in Figure 4.12. In the endcap regions CSC are

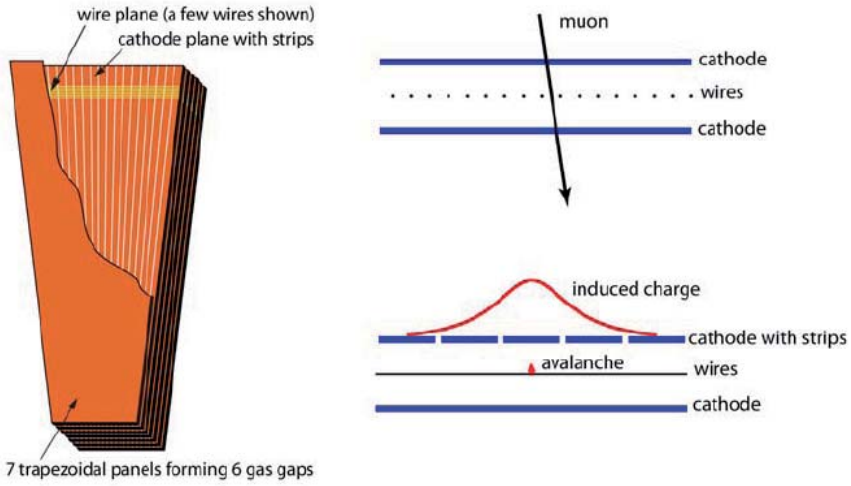

Figure 4.12: The CMS CSC used in the endcaps of the muon system [30].

used due to their radiation tolerance and fast response time. Particles passing the CSCs lead to gas ionization along the track. The electrons of the ionized gas drift to the array of wires and develop an avalanche near the wires. The moving charges induce charges in the cathode strips. These signals are measured and the track of the passing particle can be interpolated later. The endcaps consist of 540 CSCs divided into four endcap disks ME1 to ME4. One endcap is divided further into two rings (the inner most into three), where one inner ring is consisting of 18 trapezoidal chambers (36 for the others). Each wire plane consists of about 1000 wires with a gap of 3.2 mm. They provide a measurement in ϕ-direction. The cathode strips have a changing width due to their trapezoidal form and cover a constant $\Delta\phi$ slice of 2 mrad and 5 mrad. The seven cathode planes are separated by a 9.5 mm gas gap (mixture of Ar, CO_2, and CF_4).

Resistive plate chamber system

The third segment of the muon system is the resistive plate chamber system which has a fair spatial resolution but a time resolution (of a few nanoseconds) comparable to that of scintillators. This feature makes RPCs especially usable for trigger purposes. RPCs are used in both, barrel and endcaps. Six layers are embedded in the barrel and three in the encaps. RPCs are able to operate in avalanche mode or in streamer mode (discharge mode). Each RPC detector consists of a double-gap bakelite chamber (Figure 4.13), operating in avalanche mode. The gaps have a 2 mm width.

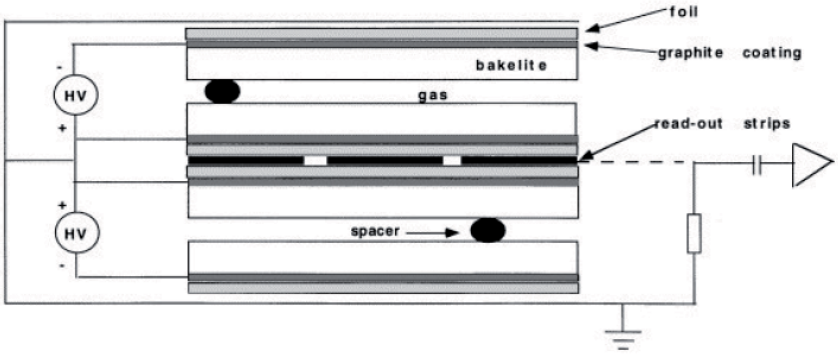

Figure 4.13: The CMS RPC system used in both the barrel and the endcaps of the muon system [30].

The gas gap is sandwiched between the two resistive electrode plates. These plates are painted with a graphite coating, which is used to distribute the high voltage on the electrodes. The plates are separated from the graphite coating by an insulating foil. In avalanche mode the release of the primary charge by the incoming ionizing radiation is followed by the propagation and multiplication of the electrons. This is shown schematically in Figure 4.14:

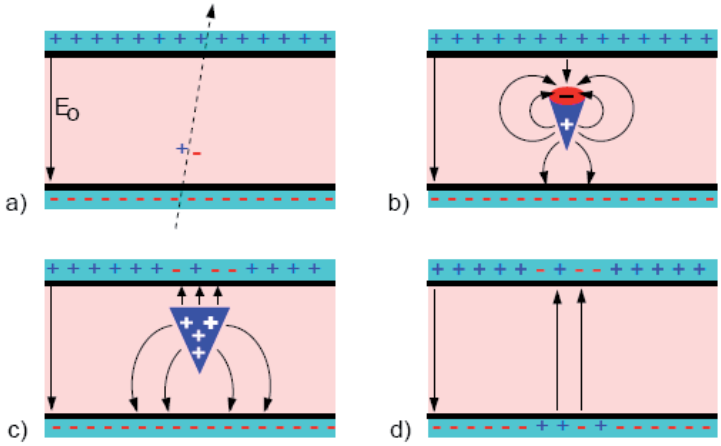

Figure 4.14: Schematic draw of the avalanche mode of the RPCs [38].

4.2.4 Solenoid

The worlds largest superconducting solenoid (Figure 4.15) with a mass of ~ 300 t, is sited in the center of the CMS detector. It is designed to reach a 4 T magnetic field to secure a sufficiently curved track of charged particles to measure the momentum and sign of their charges. With a 6 m diameter it surrounds the full tracker and calorimeter system (Figure 4.4) and stores 2.6 GJ energy

at full current. The 10 000 t weighing return yoke located in between the muon system guarantee the return of the magnetic flux. The solenoid is cooled with a helium refrigeration system plant [35] [36].

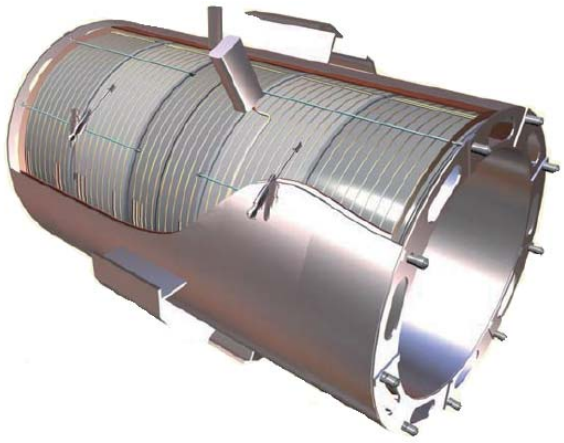

Figure 4.15: The Superconducting Solenoid [35] in CMS.

4.2.5 Trigger

LHC at its design luminosity will lead to particle collisions every 25 ns (time for each bunch crossing). Most of the events are soft, meaning that the collision did not produce new particles but the protons did change their direction or emitted a photon due to bremsstrahlung. Storing all this event data is technically not possible for today's computing performance. Therefore a trigger system has been developed for the CMS detector. It consists of two parts: The level 1 trigger (L1) is a hardware based trigger and provides decisions every 25 ns in order to reduce the event rate from 40 MHz to 100 kHz. The software based trigger called high level trigger (HLT) is an offline trigger and has more time for making decisions, and reduces finally the event rate from 100 kHz to 100 Hz, which is possible to manage. Detailed lists of trigger thresholds are given in [39] [36].

4.3 Running conditions and data taking

In fall 2008 the first beam successfully circumnavigated the LHC circle. Unfortunately an incident concerning several dipole magnets made it impossible to get data from collisions. To avoid another incident and understand the response of all components used, a strategy for the first beams has been performed [40] starting at the end November.

Month	Comment	Beam energy [TeV]	Bunch number	protons / bunch	Peak Lumi. $cm^{-2}s^{-1}$	Integrated luminosity
1	Commissioning					
2	"Pilot physics"	0.45	43	3×10^{10}	8.6×10^{29}	$\sim 200\,nb^{-1}$
3-5	bunch intensity	1.1	156	10×10^{10}	6.9×10^{31}	$\sim 50\,pb^{-1}$
6-7	move to 3.5 TeV	3.5	156	7×10^{10}	4.9×10^{31}	$\sim 30\,pb^{-1}$
8-11	increase lumi.	5	432	9×10^{10}	2.1×10^{32}	$\sim 200\,pb^{-1}$

Table 4.2: LHC luminosity performance plan (preliminary) [40] and corresponding beam energies.

Chapter 5

Monte Carlo and Computing Setup

Nowadays the theory of particle physics is described by quantum field theory. In this theory perturbative calculations for interactions have shown to predict experimental results precisely. This is not true for QCD processes, where the quark and gluon fields are confined asymptotically due to the scaling behavior of the coupling constant of QCD, α_s, which becomes small only for large momentum transfers (large energies or small distances). This confinement to some extent restricts the validity of perturbative calculations in QCD. Thus, a quantum-mechanically correct treatment of a collision is currently not possible [41]. Besides the already mentioned non-perturbative confinement, even for perturbatively accessible energy scales a full calculation is restricted to a relatively small number of particles involved, as the number of Feynman amplitudes to be calculated grows factorially with the number of involved particles. A realistic description of QCD bremsstrahlung is beyond this limit, and can be performed only by imposing further approximations and phenomenological models.
Numerical methods like Monte Carlo simulations [42] have been used to describe scattering processes at colliders. Monte Carlo simulations rely on random or pseudo-random numbers.

5.1 MC Generators & SHERPA

Approaches such as the PYTHIA [43] Monte Carlo event generator have succeeded describing former and recent data [44]. A scattering process is evaluated at tree level $2 \to 2$ (two initial and final state particles) only (no loop diagrams or higher order QCD radiations) matrix element. The QCD corrections are computed via a parton shower algorithm [1]. The non-perturbative confinement is treated by phenomenological hadronization models [45]. Facing new challenges at LHC (c.o.m. energy up to $\sqrt{s} = 14\,\text{TeV}$), this procedure is insufficient [41] for the description of higher jet multiplicities and QCD corrections of a scattering event. To describe LHC collisions more precisely higher jet multiplicities have to be estimated not only via the parton shower algorithm but already by the phase-space integration of the higher order matrix elements as the matrix elements have to be evaluated at scales, which are far from the hadronization scale.
SHERPA is a C++ based event generation framework [46] able to simulate all stages of high energy scattering, from the hard scattering up to the final state particles observable in the detector as shown in Figure 5.1. Also the underlying events due to multiple parton interactions in one event can be simulated in SHERPA as well. A crucial point of any generator is the combination of the matrix element and the parton shower as this predicts the evolution of the initial state partons of the matrix element to a hadronizing jet. In SHERPA this has been improved by the CKKW [48, 49] merging method. CKKW allows to consider higher order tree level processes contributing to the cross section of the process. Therefore CKKW divides the phase space for parton emission into a regime of jet production, described by the corresponding matrix element, and a regime of the evolution of the jet, performed by a parton shower [50]. The borderline of these regimes is defined by the $k_\perp$ algorithm (in the literature also called "Durham algorithm") [51]. In the $k_\perp$

[1] Several other generators calculate the matrix element but also use the PYTHIA parton shower generator.

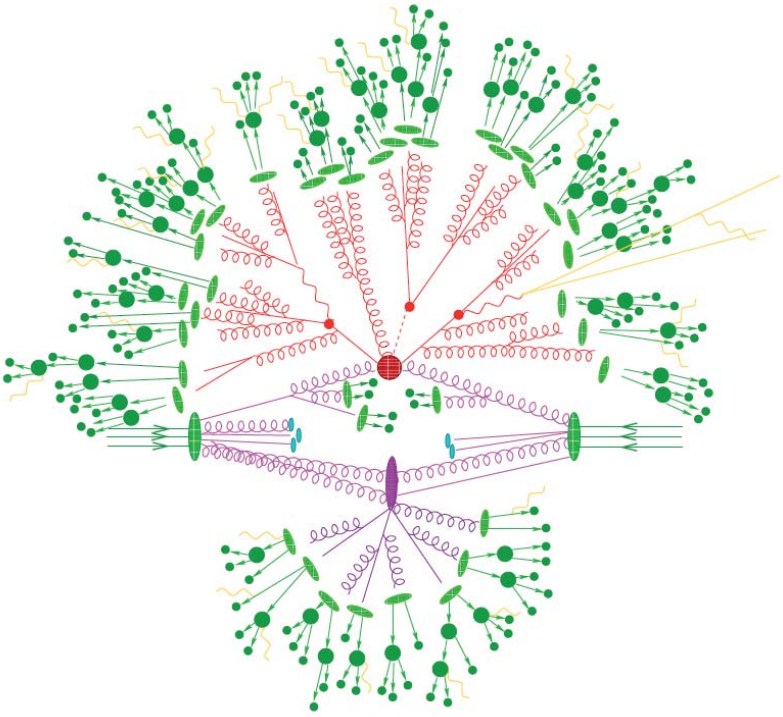

Figure 5.1: Schematic view of a p-p collision [47]. The hard process (dark red blob) followed by the decay of unstable particles (red blobs). From the red blob the parton shower invokes and emits hadrons. These hadrons finally hadronize and become jet shown in the green blobs. Underlying events are shown in the purple blob. Finally the hadrons decay further or radiate final state photons.

algorithm two particles i and j belong to different jets if they are separated by a distance

$$y_{ij} \equiv 2\min(E_i^2 E_j^2)(1-\cos\theta_{ij})/E_{\mathrm{CM}}^2 \leq y_{cut} \ , \tag{5.1}$$

where $E_{i,j}$ are the energies of the particles, $\theta_{i,j}$ is the angle between their momenta and E_{CM} is the center of mass energy of the collision [48]. These distances are compared to the resolution variable y_{cut}, which is a free parameter in SHERPA . Numerous hadronic final states do not necessarily come from different jets, but can be reduced to an initial jet that hadronized or emitted additional QCD bremsstrahlung. So the $k_\perp$ algorithm clusters (color charged) particles which were produced in QCD processes and matches them to one colorless jet. Thus, y_{ij} is the minimum distance of two particles which is resolved in the momentum space. If two particles are not resolved, they are clustered by combining their four momenta $p_{i,j} = p_i + p_j$. If $y_{cut} < y_{i,j}$ the two particles are resolved and Sudakov form factor [52] reweightings are applied to the matrix element. Descriptively the Sudakov form factors represent the probability for a quark or gluon to evolve from a scale Q to Q_1 without any branches. So the Sudakov form factors take care of the probability that the resolved particles originated from partons of the matrix element. For $y_{cut} > y_{ij}$ the particles originate from the same jet and SHERPA treats these particles as objects that have been separated due to parton showering.

Goal of the SHERPA framework is to describe *any* hard n-particle final state configuration to a certain order (where n is currently limited to ≤ 5 for computational reasons). The general scheme of the SHERPA algorithm including the procedure of CKKW merging can be summarized in following steps [49]:

1. A process to be studied is selected and the maximum parton multiplicity to be generated is specified. The cross section for all requested parton multiplicities is calculated. SHERPA

does not use pre-calculated matrix elements but integrates the phase space. For N possible Feynman graphs of the selected process the probability to select the matrix element i ($i = 1...N$) with jet multiplicity n is:

$$P(n,i) = \frac{\sigma_{n,i}}{\sum_{k,j}^{k=N} \sigma_{k,j}}, \tag{5.2}$$

where $\sigma_{n,i}$ is the i-th tree-level cross section of the multi jet process with the jet multiplicity n at a fixed strong coupling scale α_s.

2. The kinematics of the matrix element is calculated after a parton multiplicity has been chosen. The parton momenta are distributed to the jets corresponding to the matrix element squared $|\mathcal{M}_{n,i}|^2$. This is done by phase space sampling.

3. The next step is to determine the QCD energy scales at which the $k_\perp$ clustering of the jets is performed. These scales are called *nodal* values and due to the high energy dependency of the coupling constant α_s it is very important to know these values. To determine the nodal values the resolution values y_j (compare with $y_{i,j}$) are calculated by the $k_\perp$ clustering for each jet. So every particle in the distance of y_j has been clustered to the j-th jet. After this is done for every jet, the nodal values are set as $q_j = E_{\mathrm{CM}}/y_j$.

4. After the nodal values have been determined, they are applied as a coupling constant weight for the strong coupling $\alpha_s(q_j)$ in order to take care of the energy dependency of α_s.

5. The event is now reweighted with the product of Sudakov form factors and the coupling strength. If it exceeds the limits of the matrix element sampled in step 2, it is discarded and the algorithm returns to step 1, otherwise it is used further.

6. The previous reweightings and coupling constants are taken as initial conditions for the parton shower. Once the parton showers are attached to the outgoing particles, phenomenological models are used to determine the evolution of the parton shower. Inside the parton shower, additional emissions are vetoed that lead to additional jets that are beyond the scale y_{cut}.

Hence, there is a maximal number n_{max} of jets covered by the matrix elements (due to computational reasons), higher jet multiplicities must be accounted for by the parton shower. This leads to a modified treatment of the parton shower for those events with n_{max} jets stemming from the matrix elements.

However there is still the non-vanishing probability to cluster a jet from the parton shower with one jet which has been radiated due to initial state radiation (double counting). This is avoided by a possible jet veto, which is technically performed considering once again the Sudakov form factors and the probability for the jet to branch.

The following main modules are used in SHERPA .

- AMEGIC++ (A Matrix Element Generator in C++) which is based on Feynman diagrams, using PHASIC++ (the Phase Space Integrator in C++) for integrating the Monte Carlo phase space.
- The evolution of each parton shower is computed by APACIC++ (A Parton Cascade in C++).
- AMISIC++ (A Multiple Parton Interaction in C++). This module simulates multiple parton interactions, crucial for realistic scenarios at hadron colliders. The multiple parton interactions are further treated with APACIC++.
- AHADIC++ (A Hadronization (Module) in C++). This module translates initial partons (gluons and quarks) into final state hadrons, detectable in the experiment.

The ADD model implementation of SHERPA [53] provides additional vertices and couplings to the Standard Model. The Kaluza-Klein graviton coupling to the Standard Model is included according to Equation 2.82. The implementation of the ADD model is constructed upon a helicity formalism of spin-2 particles. The helicity amplitudes are integrated in order to get the graviton couplings.

In general the user has to edit the configuration file `Run.dat` where the process, physics model, and other parameters like kinematic constraints are defined (see appendix). All necessary ADD-model parameters can be set like in the following example.

```
N_ED          = 2        ! Number of extra dimensions in ADD model
M_S           = 2.50e3   ! string scale for ADD model [TeV], meaning depends
                         ! on KK_CONVENTION
M_CUT         = 10.00e3  ! cut-off scale [TeV] for the c.m. energy.
KK_CONVENTION = 5        ! Sum(HLZ) (1=simple, 2=exact)
                         ! 5=GRW (Lambda_T(GRW)=M_S)
```

`M_CUT` is a parameter that bans ADD-like couplings at energy scales larger than `M_CUT`. The configuration file `Run.dat` is used to create the libraries of the process defined in the configuration file [54]. These libraries are used to calculate the cross section of the process. Libraries and cross sections are needed in order to create MC events.

5.2 CMSSW

The CMS Software (CMSSW) [55] is a framework of software needed for the simulation, calibration, alignment, and reconstruction of data (Monte Carlo). CMSSW provides different modules so that special analyses can be performed. A specific analysis module is a piece (or component) of code that can be plugged into CMSSW. So all physicists in CMS benefit from the same framework and core software but are able use their own modules for their special needs.

5.3 Generation of MC Samples

The general chain of MC production is shown in Figure 5.2. Firstly there is the collision data

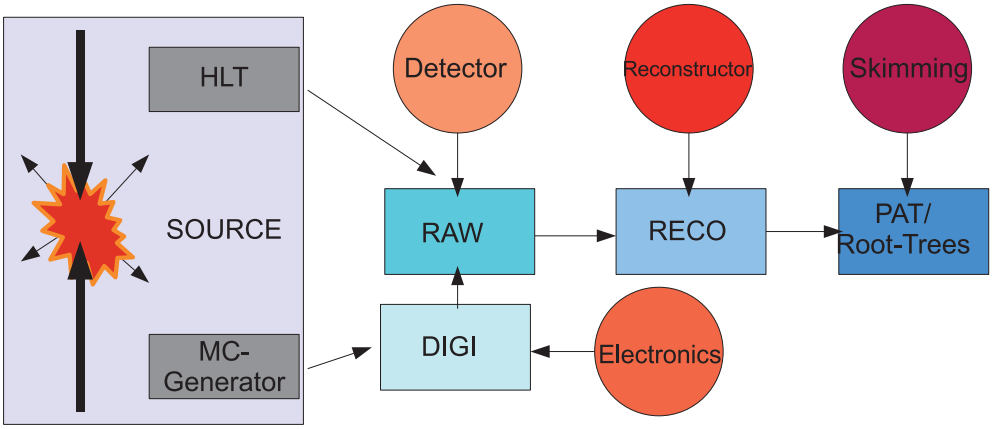

Figure 5.2: Production chain of MC production and collision data taking. Up to the step of detector response (RAW format), the computing chain is fixed. The desired Reconstructor and the data format for skimming is depending on the needs of the end user.

(the event needs to be triggered by the HLT) or, as presented in this thesis, Monte Carlo (MC)

generated data. For MC data the response of the detector material has to be simulated. This is done with the program GEANT [56, 57] and stored in the DIGI format. Now the information of the detector material interacting with the particles are transformed into the RAW format, which contains the response of the different detector parts and the digitalizing of the taken detector signals (like converting a electronically signal in the RPC into a digital information). The simulation of the detector response is redundant for collision data as the detector information is digitized by the electronics immediately. The reconstruction step, more precisely explained in the next chapter, applies algorithms to the digitalized signals so that physical objects can be reconstructed and their properties (charge, track, energy) can be measured. This is called the RECO format. The end-user can work on RECO files. To further reduce the amount of data the collaboration uses PAT (Physics Analysis Toolkit) [58] where the user decides how much information is necessary to keep and can drop the rest. For a cut based analysis like the presented one, even PAT data contains unnecessary information to some degree. So PAT files themselves are skimmed (skimming is an expression for pre-selection) using Root trees [59] provided by the CMS Aachen 3A SUSY group.

Chapter 6

Muon Reconstruction and Selection

In this chapter the reconstruction and selection of muons is presented. As the ADD model of LEDs predicts theoretical deviations from the Standard Model in the invariant di-muon mass distribution $M_{\mu\mu}$ and the decay angle $\cos\theta^*$, both distributions are reconstructed and discussed. According to Figure 5.2 the detector signals are treated with different algorithms in order to reconstruct physical objects. The impact of different outer conditions such as a not perfectly aligned detector is discussed, too.

6.1 Muon Reconstruction

The identification of muons is to some degree straightforward compared to other particles. Muons are the only particles passing the whole detector and creating a signal in the muon system. The muon's properties (e.g. charge or p_t) are mainly derived from its curved track in the magnetic field of the solenoid. The track itself is reconstructed according to the hits of the muon traversing the detector. In CMS the muon reconstruction is performed with three algorithms, one basic reconstruction algorithm and two advanced algorithms.

- Reconstruction of the muon from local pattern recognition is the basic reconstruction algorithm. Here the local hits in the detectors are used and the track of the muon is fitted. The algorithm starts from a seed. A seed consists of a set of reconstructed hits in a certain detector part.
- Standalone muon reconstruction is limited to the muon system, only taking signals from the DTs, CSCs, and RPCs as input.
- Global muon reconstruction: The track of the muon in the muon system is extrapolated to the inner tracking system and a combined reconstruction is performed.

Standalone muon reconstruction

The standalone muon reconstruction is built upon the local reconstruction where the tracking detectors (DT and CSC) and the (timing) detector RPC are used. The reconstruction begins with the innermost track segments of the muon system. These track segments are used as seeds for the muon trajectory building. A Kalman-Filter [60] is used to define a cone inside the next chambers. Inside this cone the trajectory of the former chambers is extrapolated and hits are sought that match to the trajectory. If there is no matching hit in a following chamber, the search is continued in the next chamber. The search is applied backward to the innermost chambers after the procedure has reached the outermost measurement system. After each step the track parameters are updated and material effects are taken into account. Also a loose χ^2-cut is applied to the trajectories to reject bad hits, mostly due to showering or cosmic hits. This procedure of reconstruction is basically the same for the track and hit reconstruction of the particles passing the tracker system. The silicon strip detectors are used to reconstruct the track whereas the pixel

signals deliver the seed positions.

Global muon reconstruction

After the construction of standalone muons the trajectories can be extended into the tracker system and the hits of the muon in the tracker can be included. Again material effects are considered as uncertainties. Track parameters and uncertainties define a region of interest in the tracking system where additional hits are expected. The final reconstruction is done after trajectory building (all seeds are recognized and all possible trajectories), trajectory cleaning (cleans ambiguities of several trajectories originated from one single seed using the number of hits and the χ^2 of track fit) and finally a fit that smoothens the track using all information gained in the steps before.

In addition to these three standard reconstructors the CMS collaboration also developed several special muon reconstruction algorithms. They are optimized to the non-perfectly aligned detector and the special constraints of so-called high-p_t or TeV-muons. After a critical energy E_C a muon looses more energy due to bremsstrahlung than by ionization. A (very simple) approximation for muons is $E_C \approx \frac{24\text{TeV}}{Z}$ meaning for iron $\sim 1\,\text{TeV}$ [61]. There have also been attempts to reconstruct muons only with properties delivered by the tracker system (or the "tracker plus first muon station"). This has been studied in the CRAFT'08 CMS-paper [62] and will be compared to the global muons in this chapter.

The perfectly aligned detector geometry is simulated with the IDEAL_V12 scenario inside CMSSW. Section 6.1.1 deals with the ideal geometry scenario and introduces to basic properties such as efficiency and resolution of global muons. In Section 6.4 the impacts of different detector alignments will be discussed further for both global and tracker only muons.

6.1.1 Muon Selection Criteria

The goal within this study is to separate the *signal* events (ADD) from the *background only* (Standard Model (SM)) by cuts on different muon properties. As discussed in Section 3.3 the virtual graviton exchange is a Drell-Yan process with an additional $g\,g \rightarrow G_{KK} \rightarrow \mu^+\,\mu^-$ contribution and the interference process $q\,\bar{q} \rightarrow G_{KK} \rightarrow \mu^+\,\mu^-$. So the *signal* events have a signature as follows:

- As the two muons originate from a non-charged virtual particle they have to have opposite charges.
- Due to the additional processes there will be more di-muon -pairs produced at high invariant masses.
- Compared to the SM the angular distribution will be different as the graviton is a spin-2 (tensor-) particle and not a vector boson like a photon or a Z-boson.

Backgrounds with a di-muon final state are:

- **Standard Model Drell-Yan** Quark and antiquark $q\bar{q}$ annihilate to a virtual photon or Z-boson. The intermediate particle then decays into a di-muon pair. This is the main background of the studied signal and gives an almost (differences in the angular distribution) identical final state.
- **Top anti-top quarks** Two oppositely charged top quarks $t\bar{t}$ are also likely to produce di-muon pairs. A top decays with almost 100 % probability into a b quark and a W boson. The b quark hadronizes, called b-jet whereas the W boson may decay in a muon (and neutrino). Due to the b-jet $t\bar{t}$ events will have a higher jet-multiplicity than Drell-Yan events.
- **Double vector bosons** The pair production of vector bosons is also possible at the LHC. The two bosons can also decay into two muons in the final state. Possible occurrences are (ordered in decreasing cross sections) WW, WZ, ZZ.

- **W+Jets** A quark pair annihilating into a $W^{\pm}$ boson where one of the quarks has emitted a gluon in the initial state (before the hard process). The W-boson may possibly decay into a muon and a muon-neutrino. The other muon may come from the hadronizing jet. As one muon stems from a jet, it has a different signature compared to muons which originates from hard scattering processes.

- **Multi-Jet** Multi-jet events have a huge cross section for hadron colliders at processes with low fractional momentum transfer. Hadronizing jets can decay further into muons. Multi-jet events will have a very different signature from the other backgrounds and are discussed separately.

The reconstruction of these events is mainly depending on the acceptance and the triggering of the CMS detector. Therefore the following two preselection cuts are applied:

1. Triggering. As described in Section 4.2.5 an event needs to be triggered in order to be stored. The CMS experiment provides a large variety of triggers with different thresholds. Several triggers have been studied concluding that the single muon trigger HLT_Mu9 combined with the double muon trigger HLT_DoubleMu3 is the best and sufficient choice for the presented analysis. The single muon trigger is based on the global muon (combining muon system and tracker) reconstruction and requires at least one global muon with $p_t > 9$ GeV [63]. The double muon trigger HLT_DoubleMu3 requires two global muons, with each $p_t > 3\,\text{GeV}$. To reconstruct the event the muons have to be inside the acceptance range of the CMS detector (or else they are not seen by the detector). The detector is limited to a $|\eta|$-range less than $|\eta| \approx 2.5$ whereas the muon trigger electronics is limited to $|\eta| < 2.1$. Muons which are produced outside this range cannot be triggered. Taking the trigger efficiency into account the η-range is restricted to be smaller than $|\eta| < 2.1$.

2. A reconstructed event has to contain at least two muons in order to be able to reconstruct the invariant di-muon mass.

To ensure a clean and trustworthy muon signature several selection cuts have to be applied. The Muon Physics Object Group (POG Muon) [64] of the CMS collaboration evaluated different cuts very intensely to ensure that the muons originate from a hard process [1] with high accuracy. The cuts listed in [65] are the best choice for most muon analyses.

The POG muon cuts been adapted for this analysis. The requirements of criteria that both muons have to fulfill are as follows:

- The muon has to be reconstructed in the tracker and the muon system, this is called a global muon.

- The transverse momentum has to be higher than $p_t > 20\,\text{GeV}$. A higher requirement of the transverse momentum (up to ~200 GeV) would not harm the ADD signal as it is in the TeV scale, but would cut away the Z-peak at $\sim 90\,\text{GeV}$. The Z-peak is needed for calibrations of the invariant di-muon distribution and measuring the luminosity.

- Number of hits in the detector (tracker and muon system) $\text{N}_{\text{Hits}} > 11$.

- The quality of the track fit normalized to the degrees of freedom $\chi^2/\text{ndf} < 11$. The degrees of freedom are calculated from the number of hits and the parameters of the fitted track.

- Vertex compatibility of the reconstructed track with the measured primary vertex in a range of $|d_0| < 2\,\text{mm}$ in the xy-plane. $|d_0|$ is the impact parameter.

[1] It is also possible that muons do not come from a vector boson but are created inside the detector due to material effects or from multi-jet effects.

- Muons from a $\gamma^*/Z/G_{KK}$-decay do not have additional particles next to their tracks in general. This is called isolation. Isolation is calculated in the ϕ-η-plane by $\Delta\mathrm{R} = \sqrt{(\Delta\phi)^2 + (\Delta\eta)^2}$, where ΔR is a Lorentz invariant distance in the ϕ-η-plane, shown in Figure 6.1. For high energetic muons it is more favorable to consider *relative* isolation instead of static isolation. The static isolation is suggested by the muon POG. In a cone $\Delta\mathrm{R} < 0.3$, calculated in the tracker system, there must not be more than 10 % of the muon's p_t, excluding the muon's itself, along the muon track.

$$\mathrm{Iso}_{track} = \frac{\sum_{\Delta R<0.3} p_t}{p_t} < 0.1 \tag{6.1}$$

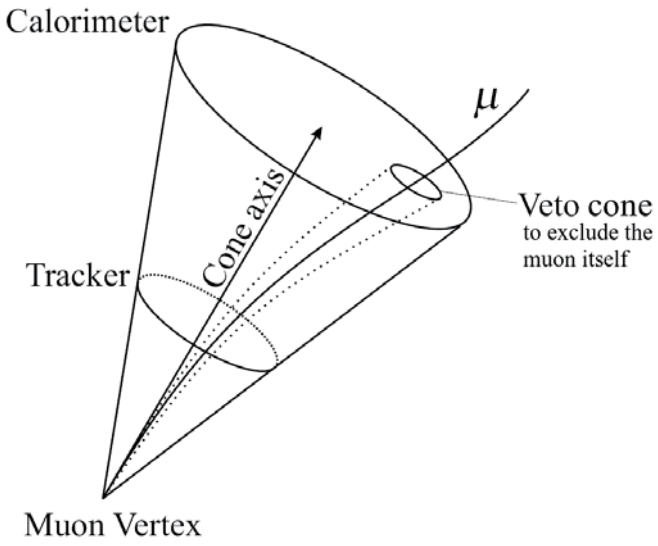

Figure 6.1: Definition of the isolation cone for a muon $\Delta\mathrm{R} = \sqrt{(\Delta\phi)^2 + (\Delta\eta)^2}$. The direction at the vertex defines the cone axis [35]. The dashed cone defines the veto area to exclude the muon itself.

It is a very efficient cut to reduce multi-jet background due to the signature of muons which are coming from jets. In this case a lot of energy is stored in a cone surrounding the muon. Thus a prompt muon must be isolated.

- The muons arising from a neutral gauge boson have opposite charges. So the last cut demands opposite sign from the two highest energetic muons selected. This cut has only very little effect on Drell-Yan muons (neither SM Drell-Yan nor ADD Drell-Yan) but reduces the number of background events.

To illustrate the different signatures of the processes the CMS-Event display Fireworks [66] can be used. Exemplary one ADD Drell-Yan and event one multi-jet event are shown with very loose cuts applied in order not to cut away too many particles, shown in figures 6.2 and 6.3.

6.1.2 Muon Reconstruction Efficiencies

The term "efficiency" is very widely used which makes it necessary to define it clearly for this study. In this study efficiency means the number of selected events corresponding to the ones generated in Monte Carlo. This includes the acceptance of the detector in the η-plane, the trigger efficiency of the detector, and the quality cuts as explained above. This will be called selection-efficiency as it represents all muons after applying the selection criteria. Technically the efficiency is estimated with the following procedure: In every event each generated muon is scanned for at most one selected muon inside a cone (Figure 6.1) of $\Delta R < 0.01$ (this value has been chosen according to

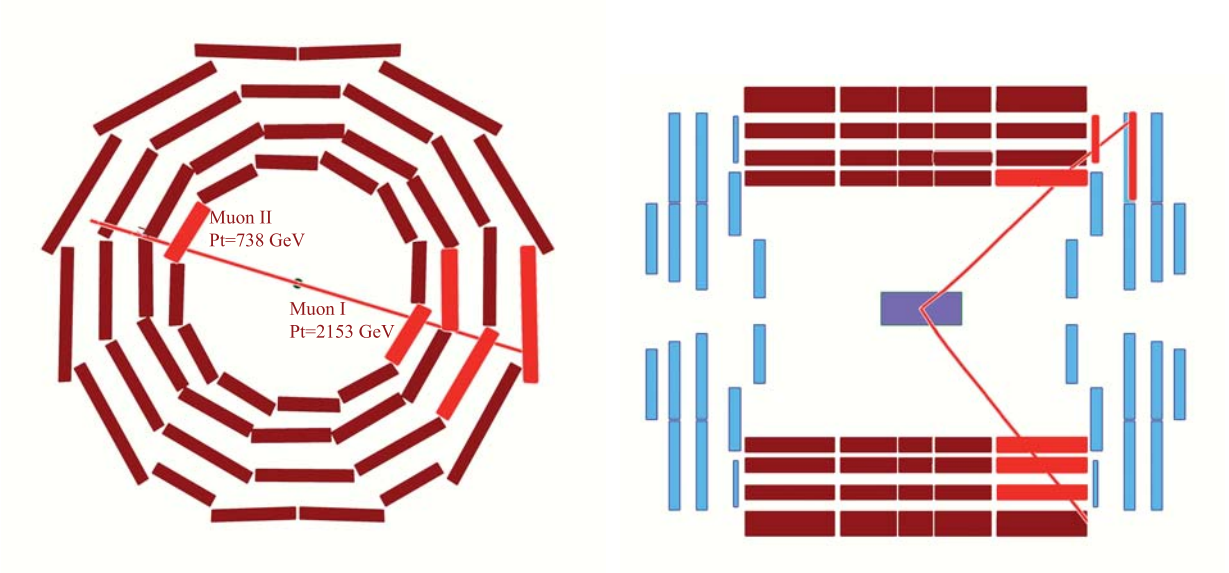

(a) ϕ-plane (b) z-plane

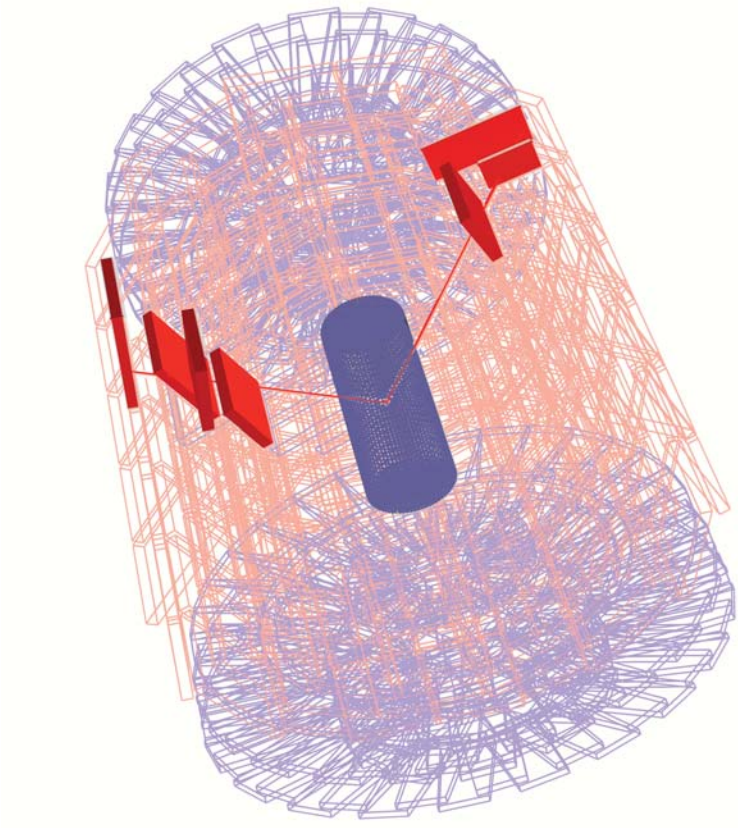

(c) Full detector view

Figure 6.2: ADD Drell-Yan event plotted with the event display CMS-Fireworks. The event is consisting of two muon tracks only without any (or very little so that it is not shown by Fireworks) energy deposit in the calorimeter system. The highlighted muon chambers denote that the muon passed the detector at that positions.

Figure 6.4). If there is one generated muon in this cone, the muon is called matched (the muon

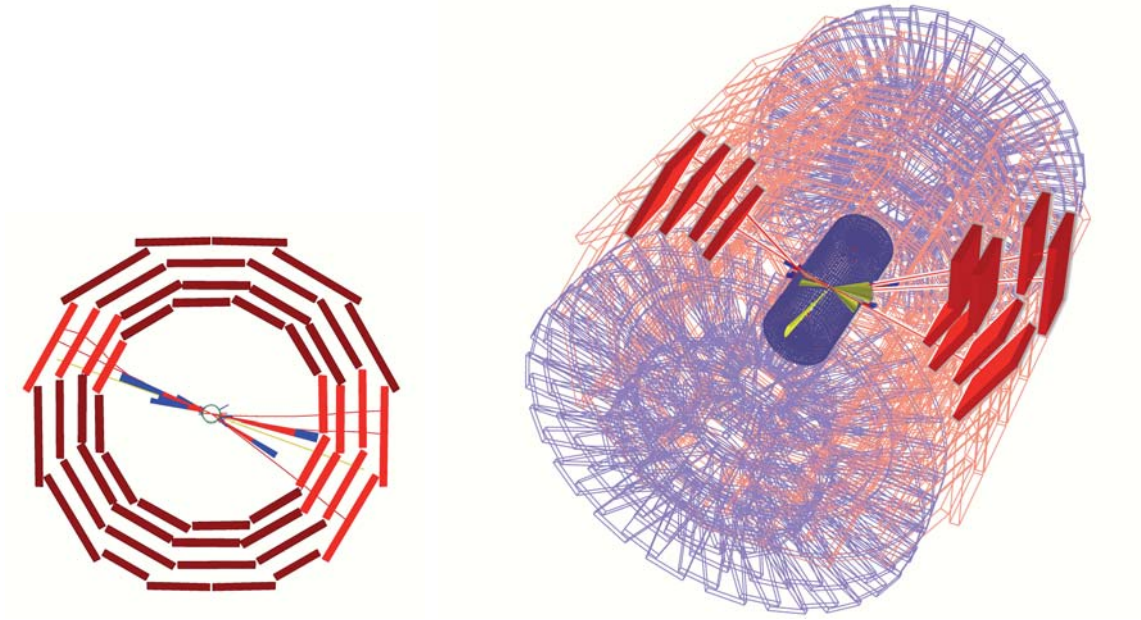

(a) ϕ-plane (b) Full detector view

Figure 6.3: Multi-Jet event plotted with the event display CMS-Fireworks. In both views the energy deposit in the calorimeter system (blue and red towers) illustrate that the event contains electromagnetic and hadronic constituents. The yellow cones in view (b) are symbols for the jets. It can be seen that the created muons originate geometrically from the jet cone and therefore have a very "low" isolation.

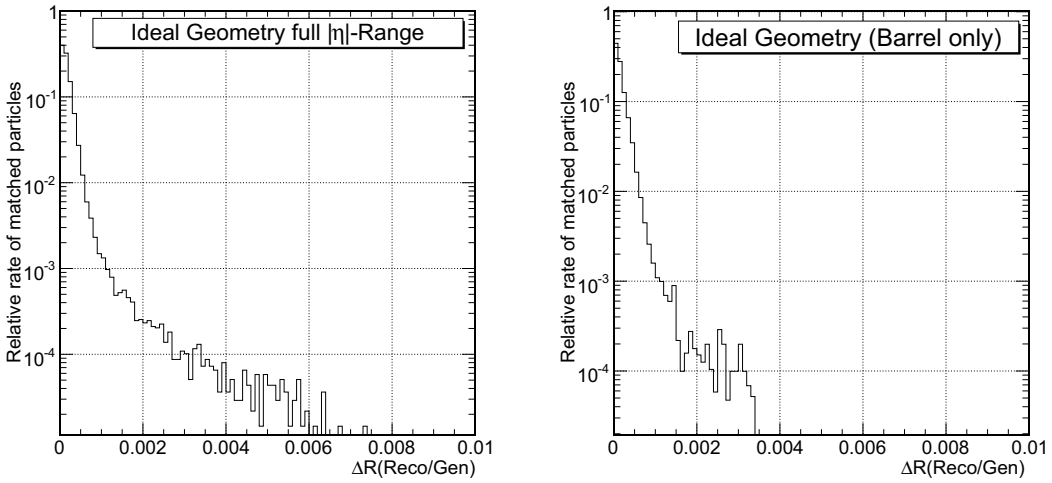

(a) The whole triggered $|\eta|$-range (<2.1) (b) The barrel region only ($|\eta| < 0.9$)

Figure 6.4: Cone ΔR between reconstructed and generated particles. A Drell-Yan dataset has been used for this illustration.

must not be matched twice) [2].

$$\epsilon_\mu = \frac{\mathrm{N}_{\mathrm{selected,matched}}}{\mathrm{N}_{\mathrm{generated}}} \tag{6.2}$$

The efficiency is a function of mainly η (Figure 6.6) and p_t (Figure 6.5). Alternatively, instead

[2]The selection efficiency is also corrected to the acceptance of the detector which means that only muons inside the acceptance range of η are matched.

of the transverse momentum p_t the invariant di-muon mass $M_{\mu\mu}$ can be used shown in Figure 6.6(a).

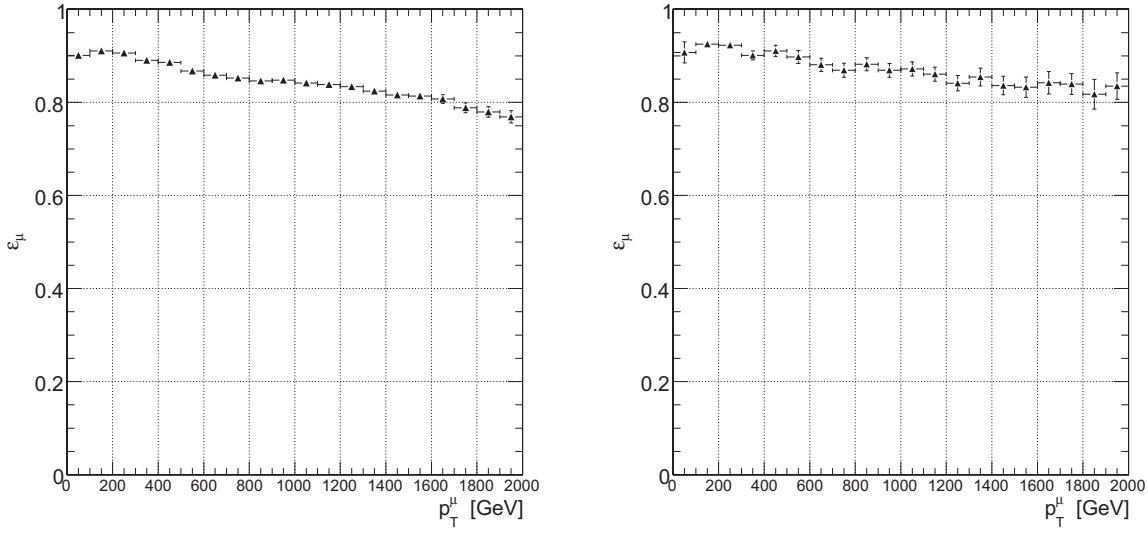

(a) Full $|\eta|$-range < 2.1 (b) The barrel region only ($|\eta| < 0.9$)

Figure 6.5: Muon reconstruction efficiency depending on the transverse momentum p_t shown for a high-p_t Drell-Yan process (generator cut on the invariant di-muon mass: 500 GeV$< M_{\mu\mu}<$ 10 TeV). It can be seen that the efficiency drops with rising p_t. In Figure (b) only the barrel region $|\eta| < 0.9$ has been used to reconstruct the muons. The efficiency in the barrel region is better than in the endcaps.

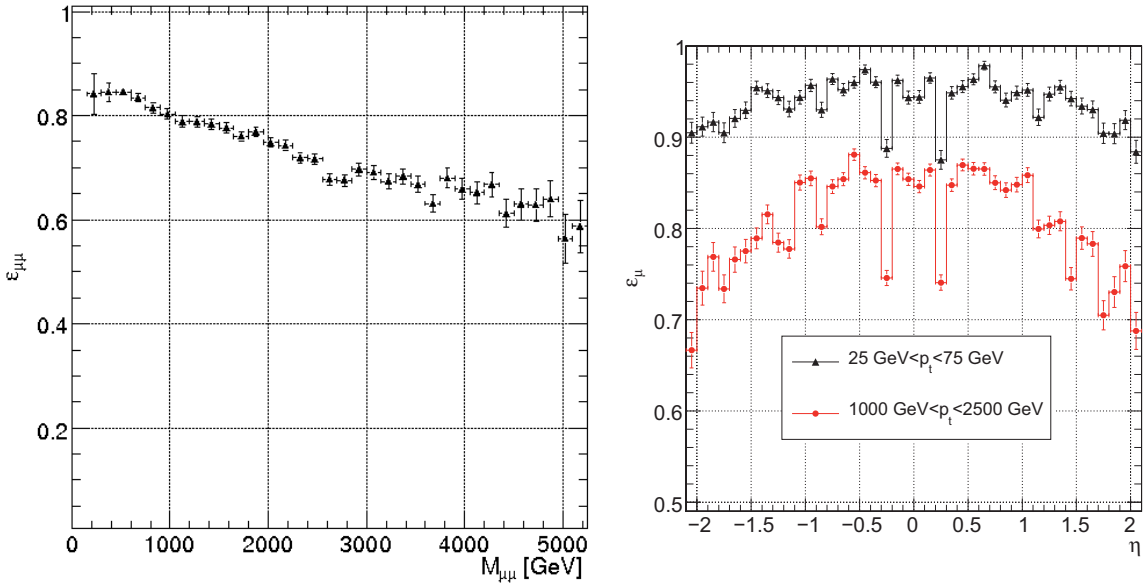

(a) di-muon efficiency for a high-p_t Drell-Yan sample (b) Efficiency for two different Drell-Yan samples w.r.t η

Figure 6.6: Muon reconstruction efficiency as function of the invariant di-muon mass $M_{\mu\mu}$ and $|\eta|$. The high-p_t Drell-Yan sample has been used in both plots, on the left and red on the right. Figure (b) shows that high-p_t muon reconstruction is significantly less efficient compared to low-p_t muons (in the Z peak area). Also the η dependency is shown as the efficiency drops significantly for high pseudorapidities.

The efficiency is decreasing with rising transverse momentum and high pseudorapidities $|\eta|$ as

shown in Figures 6.5 and 6.6. The efficiency drops down to a value of 60 % for the selection of two muons in the $M_{\mu\mu}$-distribution. This is mainly due to the cut on the track quality $\chi/\mathrm{ndf} < 11$. As previously mentioned muons with energies above ∼1 TeV are no more minimum ionizing particles but loose more energy due to bremsstrahlung in matter than due to ionization. Also in Figure 6.6 it can be seen that the efficiency significantly decreases in the transition region of the wheels 0 and 1 of the muon system at $|\eta| = 0.3$.

6.1.3 Muon Reconstruction Performance

Although the identification of muons with the CMS detector is straight forward (Section 6.1) the reconstruction of high energy muons is a very challenging task. The trajectory of muons are reconstructed using Kalman filter techniques, where the track is fitted iteratively in the muon system and tracker. Charge and p_t of the muons are obtained from the fit parameters. The dependency of p_t on the track parameters is shown in Appendix B.1 [3] and assumes the form:

$$s = \frac{1}{8} L^2 Q B \cdot \frac{1}{p_t}, \tag{6.3}$$

where L is the length of the lever arm, B the strength of the magnetic field, Q the charge of the particle, and s the size of the sagitta. A Gaussian uncertainty on the sagitta s propagates to the transverse momentum like $\sigma(s) \sim \sigma(1/p_t)$. In Figure 6.7 the core [4] p_t-resolution is shown. Up to

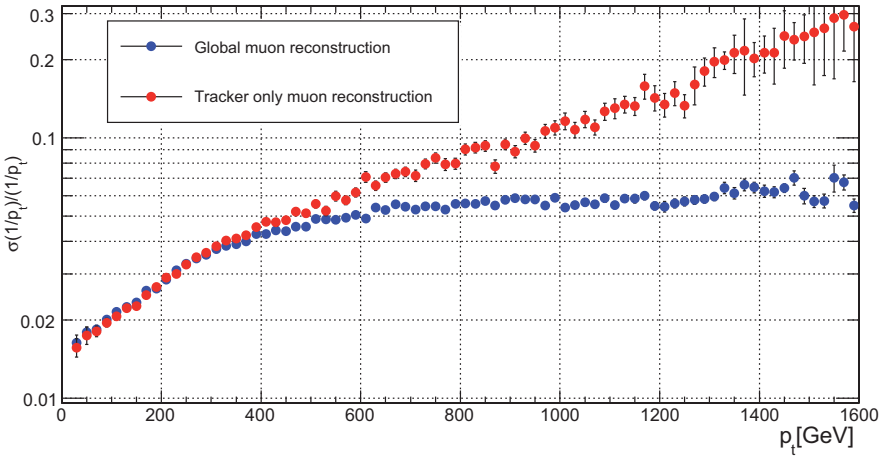

Figure 6.7: p_t-resolution for global and tracker only muons of the CMS detector ($|\eta|$<2.1). The transverse momenta up to 400 GeV are dominated by the tracker resolution. For higher momenta the muon system is dominating the resolution as the large lever arm is needed to measure the curvature of the tracks of the high energy muons.

(400 − 500) GeV the tracker fit dominates the global resolution. For higher transverse momenta the measurement of p_t is dominated by the muon system. This is due to the large lever arm which makes it possible to measure even small curvatures that are characteristic for high energy muons. The corresponding $M_{\mu\mu}$-resolution is shown in Figure 6.8.

[3] Although the reconstruction is done differently the illustration with the of the sagitta s has the same dependency of p_t.

[4] Core resolution means that the correlation as shown in Figure 6.14 at the center of the curve is assumed to be Gaussian. The tails of this distribution are not Gaussian and have to be treated differently.

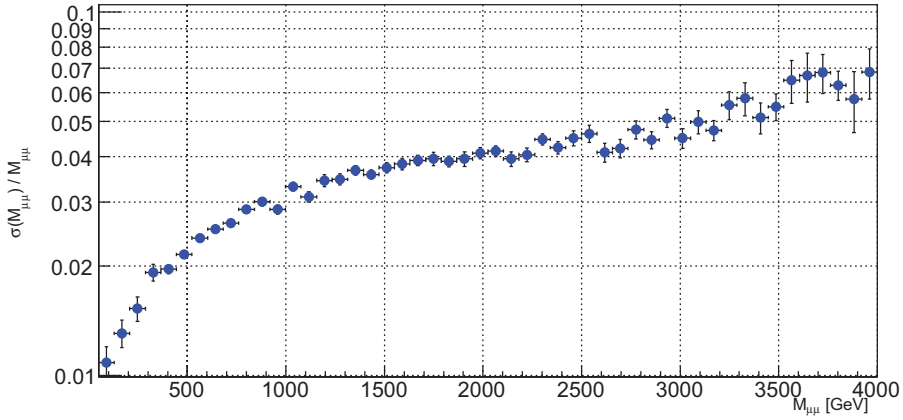

Figure 6.8: $M_{\mu\mu}$-resolution for global muons of the CMS detector ($|\eta|$<2.1). It can be seen that the uncertainty of the $M_{\mu\mu}$-resolution rises from 1 % at the Z-peak up to 7 % in the TeV region.

6.2 Invariant Mass Reconstruction

The reconstruction of the invariant di-muon mass of the selected muons is a simple task. After the two muons have been selected, their four momenta $p = (E, \vec{p})$ are summed as:

$$M_{\mu\mu} = \sqrt{\left(\sum_{i=1}^{2} E_i\right)^2 - \left|\sum_{i=1}^{2} \vec{p}_i\right|^2}, \tag{6.4}$$

$$M_{\mu\mu} = \sqrt{\underbrace{E_1^2}_{=m^2\approx 0} + \underbrace{2E_1E_2}_{2|\vec{p}_1|\cdot|\vec{p}_2|} + \underbrace{E_2^2}_{=m^2\approx 0} - \underbrace{|\vec{p}_1|^2}_{=0} - 2\vec{p}_1\cdot\vec{p}_2 \underbrace{|\vec{p}_2|^2}_{=0}}, \tag{6.5}$$

$$M_{\mu\mu} = \sqrt{2|\vec{p}_1|\cdot|\vec{p}_2|(1-\cos(\alpha_{1,2}))}. \tag{6.6}$$

where $\alpha_{1,2}$ is the angle between the two muon momenta, $E_{1,2}$ the muon energies, and $\vec{p}_{1,2}$ the three momentum of the muons. In CMS the energy is set in relativistic approximation to $E = |\vec{p}|$ and so the muon masses can be neglected. The invariant di-muon mass distribution is shown in Figure 6.9 for all listed processes (*background* and *signal*) and normalized to an integrated luminosity of $\int \mathsf{L} = 100\,\mathrm{pb}^{-1}$:

Three different ADD parameter points have been chosen as reference. The Drell-Yan processes for SM only and SM+LED (ADD) are slightly moving apart at $\sim 600\,\mathrm{GeV}$. For large invariant di-muon masses the SM Drell-Yan process dominates to the background as the applied cuts are optimized to select Drell-Yan muons.

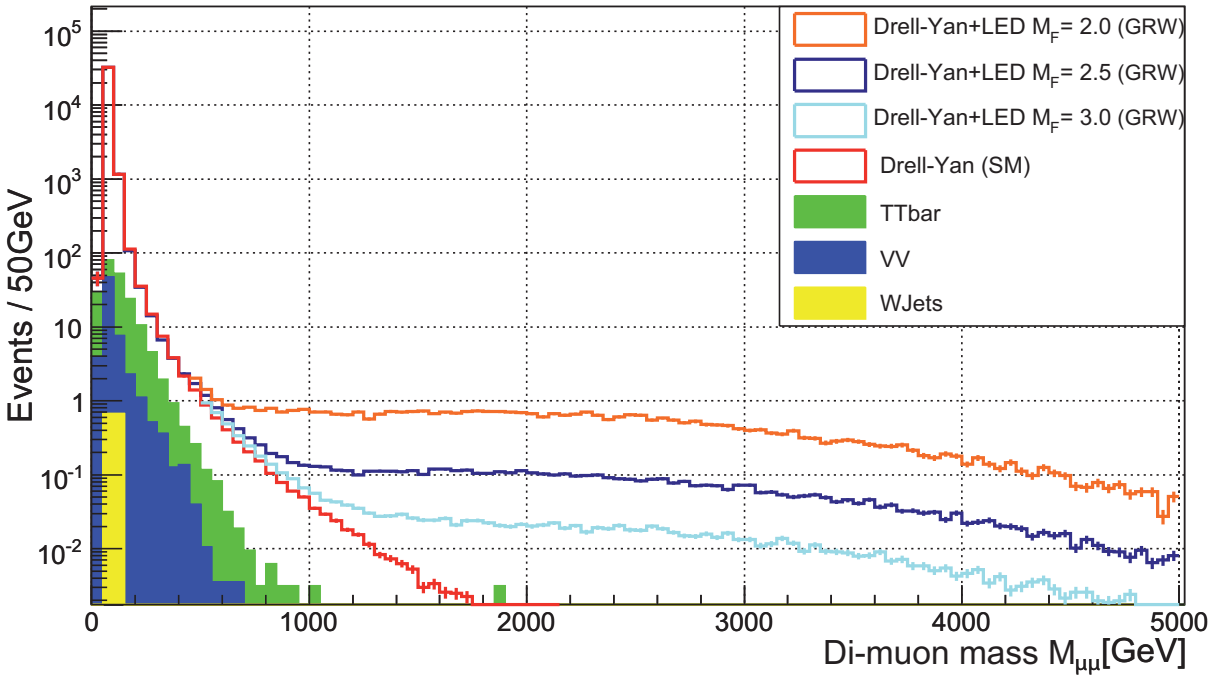

Figure 6.9: Di-muon invariant mass distribution after simulated detector reconstruction for an integrated luminosity of $\int \mathsf{L} = 100\,\mathrm{pb}^{-1}$.

6.2.1 Multi-Jet Estimation

The Multi-jet contribution is not shown in Figure 6.9. This is due to the fact that no multi-jet event [5] survives the applied cuts. As multi-jet Monte Carlo simulations are very untrustworthy (see Section 5.1) multi-jet events need special treatments. To estimate the multi-jet contribution "data-driven" techniques [67] can be used. Although in this study no LHC data has been used, this method is practised on MC events only and prepared to be exercised on real data. One method is the *cut factorization method* which has been used in this study. The goal of this method is to estimate the invariant di-muon mass distribution of multi-jet events. The procedure is comprised of the following steps:

- A single muon variable not correlated to the invariant di-muon mass has to be found. In this case it is sufficient for the variable not to be correlated to the muon p_t, as p_t and invariant di-muon mass are almost 100 % correlated (neglecting the dependency of the angle between the muons). For multi-jet samples the isolation variable is almost independent (less than 1 % correlation) from the muon p_t as shown in Figure 6.10. This means that there is the same probability for a high-p_t-muon to have a low isolation and vice versa.

- The di-muon invariant mass distribution is divided into a control and a signal region. As shown in Figure 6.9 the signal region starts at $\sim$ 700 GeV. To be more conservative, the control region is set to 400 GeV.

- Two different $M_{\mu\mu}$-distributions are needed. One distribution is gained by inverting the isolation cut (here the absolute isolation and not the relative one is used) and plotting the invariant di-muon mass. The other distribution is gained by holding the isolation fixed [6].

[5] The official Multi-jet samples are divided into *low* p_t *hat* bins, meaning that the lowest p_t of a jet within the sample is limited to a p_t cut on generator level.

[6] Unfortunately the inversion of the isolation cut did not provide enough statistics in the control region so that also the χ^2-cut had to be relaxed. But this will not be a problem as soon as real data is taken and more statistics is available.

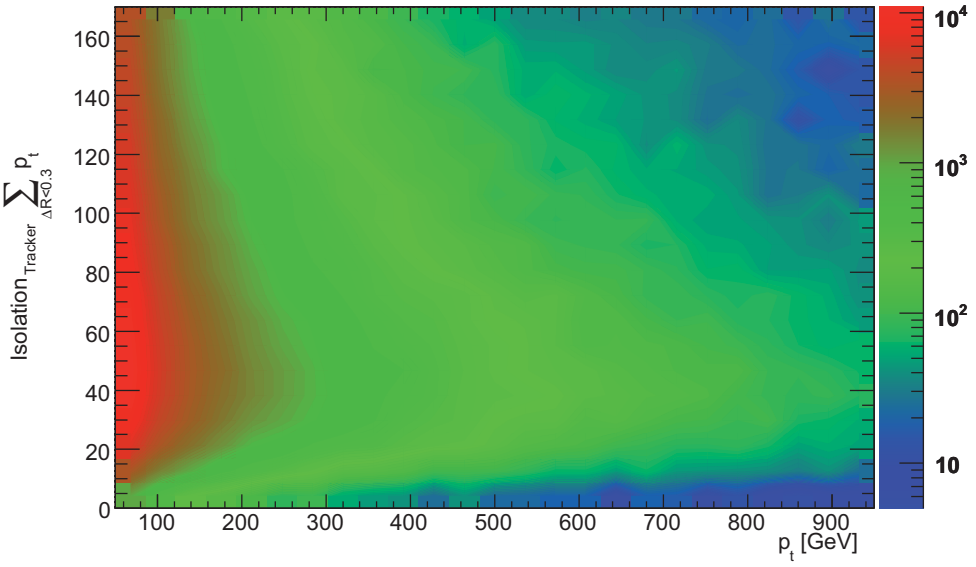

Figure 6.10: Correlation of isolation and p_t of muons from multi-jet processes. The tracker isolation is shown for different muon transverse momenta for a multi-jet Monte Carlo sample. As the two-dimensional plot is nearly uniform in direction of the isolation (slices in y-direction), no correlation between p_t and isolation can be derived.

- The distribution with inverted isolation is scaled down to the fixed-isolation distribution. This is possible because isolation and transverse momenta are not (or very little) correlated. This has been done in figures 6.11 and 6.12.

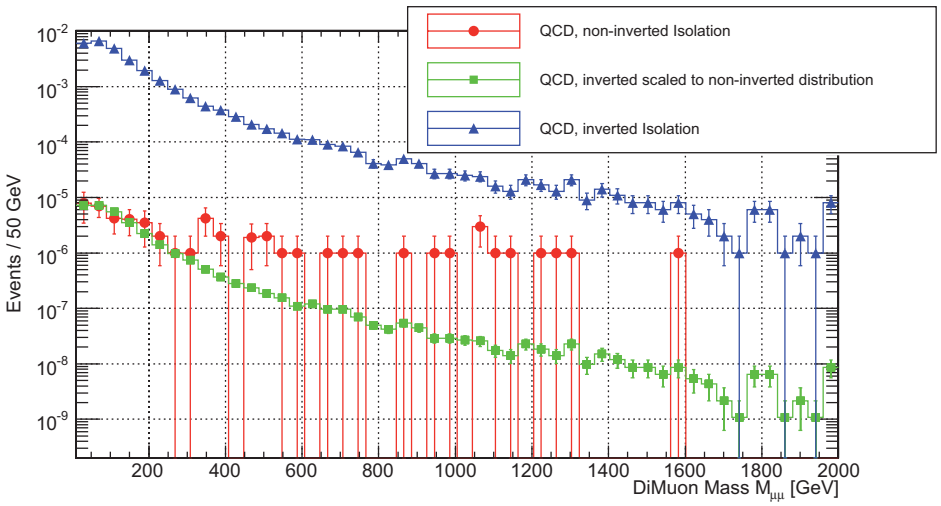

Figure 6.11: Estimation of multi-jet (QCD) events with the cut factorization method for 100 pb^{-1}.

- The multi-jet contribution is estimated from the scaled distribution. As shown in Figure 6.11 the estimated green distribution of multi-jet events is several orders of magnitude below the event rate of the SM Drell-Yan background and so can be neglected for the further analysis.

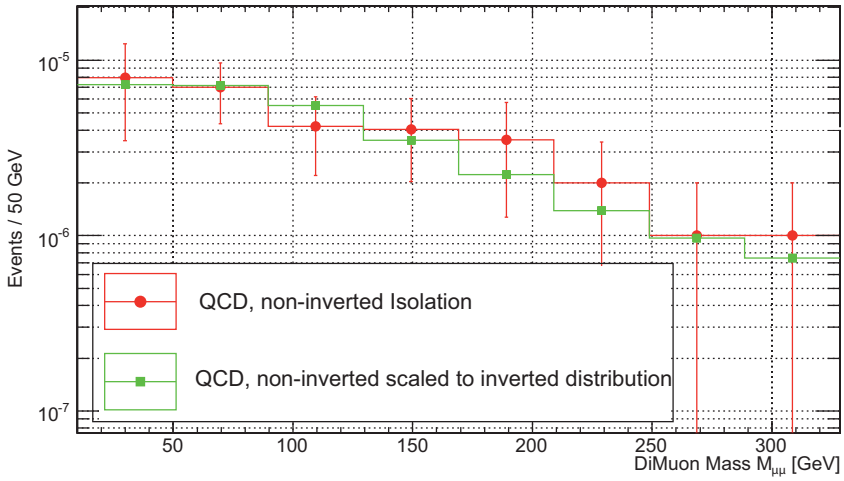

Figure 6.12: Control region of the cut factorization method for $100\,\mathrm{pb}^{-1}$.

6.3 Reconstruction of the Decay Angle

Besides the invariant di-muon mass the decay angle θ^* of the muon will also have deviations from the Standard Model according to the ADD theory. In this study the decay angle is defined as the angle between the positive charged muon and the beam axis in the *rest frame* of the decaying intermediate particle [21], as shown in Figure 6.13.

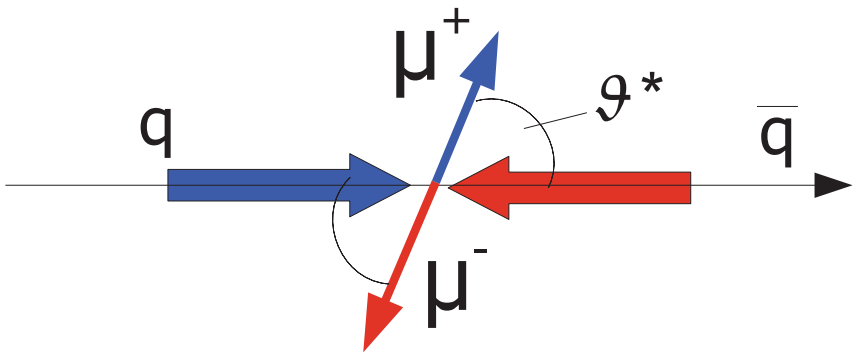

Figure 6.13: Definition of the decay angle θ^*. The choice of the angle between the positive charged muon and the beam axis is conventional.

This is done technically by a Lorentz transformation for which the rest frame for the sum of the four vectors $p_{sum} = p_1 + p_2$ of the selected muons is calculated.

$$\begin{pmatrix} m'_{sum} \\ 0 \\ 0 \\ 0 \end{pmatrix} = \begin{pmatrix} \gamma & -\beta_x\,\gamma & -\beta_y\,\gamma & -\beta_z\,\gamma \\ -\beta_x\,\gamma & 1+(\gamma-1)\frac{\beta_x^2}{\beta^2} & (\gamma-1)\frac{\beta_x\beta_y}{\beta^2} & (\gamma-1)\frac{\beta_x\beta_z}{\beta^2} \\ -\beta_y\,\gamma & (\gamma-1)\frac{\beta_y\beta_x}{\beta^2} & 1+(\gamma-1)\frac{\beta_y^2}{\beta^2} & (\gamma-1)\frac{\beta_y\beta_z}{\beta^2} \\ -\beta_z\,\gamma & (\gamma-1)\frac{\beta_z\beta_x}{\beta^2} & (\gamma-1)\frac{\beta_z\beta_y}{\beta^2} & 1+(\gamma-1)\frac{\beta_z^2}{\beta^2} \end{pmatrix} \begin{pmatrix} E_{sum} \\ p_{x,sum} \\ p_{y,sum} \\ p_{z,sum} \end{pmatrix} . \tag{6.7}$$

Solving this system of equations for the boost parameters β one gets $\vec{\beta} = (-\frac{p_x}{E}, -\frac{p_y}{E}, -\frac{p_z}{E})$. These boost parameters $(\beta_x, \beta_y, \beta_z)$ then are applied to the single muon four vectors separately. By this procedure both muons are boosted to the rest frame of the decaying particle. The angle between the positive charged muon momentum and the beam axis is reconstructed as decay angle θ^*.

6.4 Impact of the Detector Misalignment

Alignment is the orientation and adjustment of objects in relation to each other or to a static coordinate system, this means that misalignment is the uncertainty of positioning of the various detector components w.r.t. the others in the CMS experiment. As the CMS experiment did not take any collision data so far, up to the year 2008 the alignment of CMS was only known with the precision of mechanical (also laser adjustment methods) adjustments [68]. The CRAFT (CMS Run At Four Tesla) [69] data taking helped understanding the present alignment. While the CRAFT data taking [62] cosmic muons have been measured with the CMS detector. This helped in understanding the present alignment of the CMS detector.

Three different alignment scenarios are studied: STARTUP_V12 [70], $50\,\mathrm{pb}^{-1}$ [71], and the already mentioned IDEAL_V12 alignment:

- **STARTUP** represents the conditions before the CRAFT data have been used to improve the alignment of the CMS detector. The tracker and muon system uncertainty is listed in the Table 6.1

	Pixel Barrel	Pixel Endcap	TIB	TID	TOB	TEC±	DTs	CSCs
Radial uncer. [μm]	105	120	482	445	106	95	1200	1400
Angular uncer. [μrad]	270	100	412	250	75	50	1600	570

Table 6.1: Uncertainty of positioning in radial direction and angular justification for the STARTUP alignment scenario [72].

- **$50\,\mathrm{pb}^{-1}$** is an alignment scenario which has been derived utilizing the cosmic data from the CRAFT. Especially the muon system took advantage from the cosmic rays as most of the data has been cosmic muons. The Tracker conditions are identical to the STARTUP scenario. The muon system's precision has changed compared to STARTUP as given in 6.2

	DTs	CSCs
Radial uncer. [μm]	500	1200
Angular uncer. [μrad]	400	570

Table 6.2: Uncertainty of positioning in radial direction and angular justification for the $50\,\mathrm{pb}^{-1}$ scenario [72].

- **IDEAL** assumes a perfectly aligned detector in every component. So the intrinsic resolution is not spoilt by misalignment effects.

6.4.1 p_t-Resolution

For one ADD Drell-Yan sample ($450\,\mathrm{GeV} < M_{\mu\mu} < 10\,\mathrm{TeV}$) the relation between the transverse momenta at generator and reconstruction level of global muons have been compared in Figure 6.14 with a two dimensional diagram.

In the IDEAL and $50\,\mathrm{pb}^{-1}$-scenario there is a strong correlation of the generated and reconstructed muon p_t up to 2000 GeV. In the $50\,\mathrm{pb}^{-1}$-scenario the diagram gets wider as compared to the IDEAL-scenario in the high-p_t region. There are also more mis-reconstructed muons [7] in the $50\,\mathrm{pb}^{-1}$-scenario. In the STARTUP-scenario there is a very wide core area and the number of mis-reconstructed muons is much higher than in the other two alignment scenarios. For high-p_t-muons (higher than $\sim 1400\,\mathrm{GeV}$) there is almost no correlation for generated and reconstructed

[7] Here mis-reconstructed muons are muons, whose p_t is significantly not inside the Gaussian core area. The Gaussian area has been estimated with three standard deviations (3σ) from the mean.

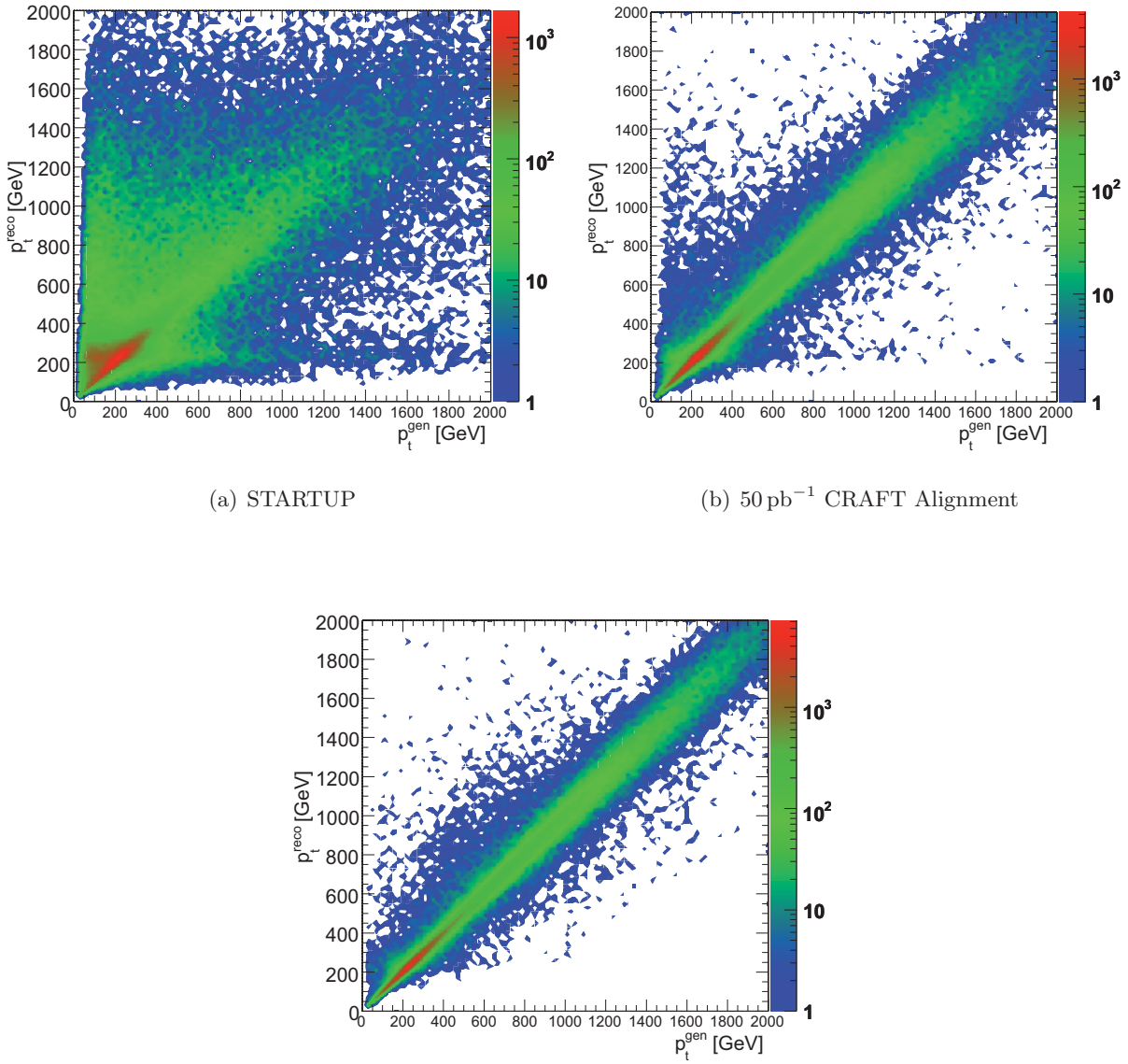

(a) STARTUP

(b) $50\,\mathrm{pb}^{-1}$ CRAFT Alignment

(c) IDEAL

Figure 6.14: Comparison of reconstructed and generated transverse momenta for one Drell-Yan sample for global muons. The widths of the distributions indicate the precision of the muon reconstruction. The points outside the main cone (outside a $3\,\sigma$ CL of a fitted Gaussian distribution in vertical slices) are called mis-reconstructed muons.

muons. The core resolutions for global muons in all three alignment scenarios are shown in Figure 6.15.

The resolution for the STARTUP scenario is very different from the $50\,\mathrm{pb}^{-1}$ and IDEAL scenario. For high transverse momenta the relative uncertainty on the momentum is more than 100 %. As explained previously one alternative procedure of reconstructing muons is the usage of tracker only muons. This reconstructor uses only the information which is delivered by the tracker system. The core resolutions for tracker only muons are shown in Figure 6.16.

For the STARTUP scenario tracker only muons have the better p_t resolution. The huge uncertainty of the transverse momentum of global muons in the STARTUP scenario is caused due to the bad alignment in the muon system. This has been mainly improved by the CRAFT'08 data. As shown in Figure 6.15 and Figure 6.16 the $50\,\mathrm{pb}^{-1}$ is based on the same tracker alignment

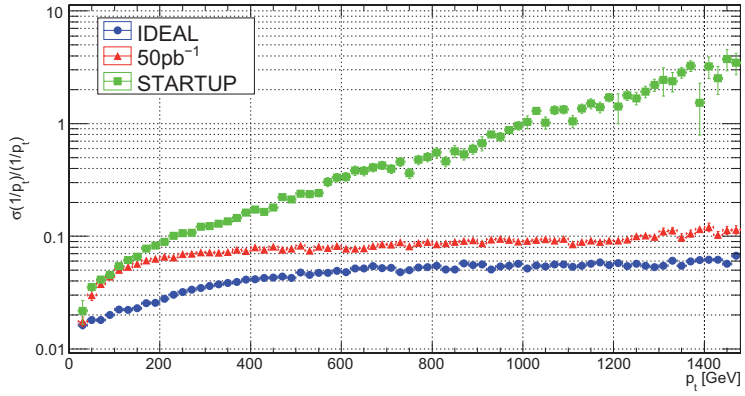

Figure 6.15: p_t-resolution of global muons for the three different alignment scenarios listed for $|\eta| < 2.1$.

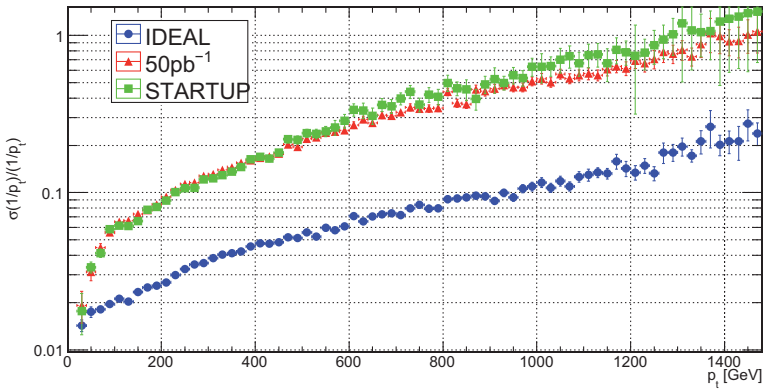

Figure 6.16: p_t-resolution of tracker muons for the three different alignment scenarios for $|\eta| < 2.1$.

as the STARTUP scenario but the muon system alignment is much closer to the IDEAL scenario.

6.4.2 Charge Mis-Assignment

Another important point of interest is the probability of muons to be reconstructed with the wrong sign of charge. In single muon analyses this might not play an important role. But in this study where a di-muon analysis is performed, the sign of the muon charge is very important to know as in every event two opposite charged muons are selected. For a Drell-Yan sample (same one as used in the resolution studies) the charge mis-assignment has been studied (Figure 6.17). In the IDEAL scenario the probability of charge mis-assignment is flat and at $\sim 10^{-3}$. In the $50\,\mathrm{pb}^{-1}$ scenario the probability is flat at $\sim 10^{-2}$, but rising at the endcap-region ($|\eta| \geq 1.4$). This can be explained by cosmic muons that mostly cross the detector perpendicular to the beam axis meaning through the barrel region and less cosmic muons through the endcaps. As there has been less statistics of cosmic muons in the endcaps, the alignment has been improved in the barrel region mainly. The charge mis-assignment probability in the STARTUP scenario is one order of magnitude higher compared to the other alignment scenarios, especially in the endcap region. For the IDEAL-scenario this has also been studied in the CMS Note [73] with very comparable results.

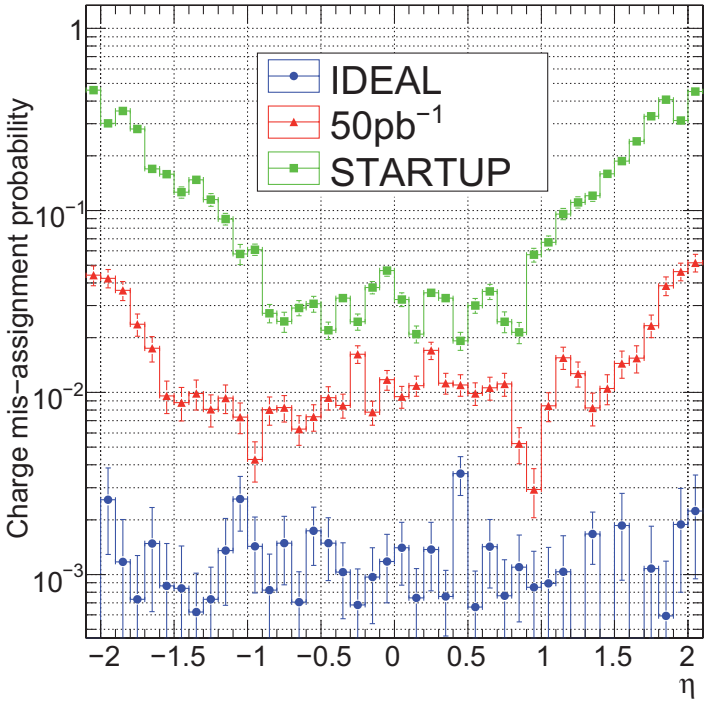

Figure 6.17: Probability of mis-assignment of the global muon charge w.r.t η for a SM Drell-Yan sample ($450\,\text{GeV} < M_{\mu\mu} < 10000\,\text{GeV}$).

6.4.3 $M_{\mu\mu}$-Distributions for Different Alignments

In Figure 6.18 the invariant di-muon mass distribution of global muons is shown for an integrated luminosity of $\int \mathsf{L} = 100\,\text{pb}^{-1}$. Within the statistical uncertainty there is no difference between the IDEAL and the $50\,\text{pb}^{-1}$ scenarios while the STARTUP scenario differs significantly. The difference can be explained due to the bad efficiency of high-p_t muons in the STARTUP scenario and the inferior momentum resolution.

6.4.4 Muon Mis-Reconstruction

The probability to mis-reconstruct muons is addressed in this section. Mis-reconstructed muons are significantly displaced (here $3\,\sigma$ deviation from the core area in Figure 6.14 is meant) muons according to Figure 6.14 and can be estimated by plotting the p_t-ratio of reconstructed muons over the generated p_t in Figure 6.19. In contrast to the core resolution where a Gaussian fit is used, the mis-reconstructed muons form a non-Gaussian tail. Although the invariant di-muon mass distribution for $50\,\text{pb}^{-1}$ and IDEAL scenario are equivalent, the probability to mis-reconstruct global muons in the $50\,\text{pb}^{-1}$ alignment is higher compared to the IDEAL scenario but still the better choice compared to the tracker only muons in the $50\,\text{pb}^{-1}$ scenario.

Consolidating all findings up to here, the choice has been made to use global muons for the further analysis. Without the improvement of CRAFT'08 data the better choice would have been to use tracker muons. But as shown in this chapter, global muon have been improved and have several advantages compared to the tracker-only muons. As soon as first collisions take place, the alignment of the CMS detector will improve further.

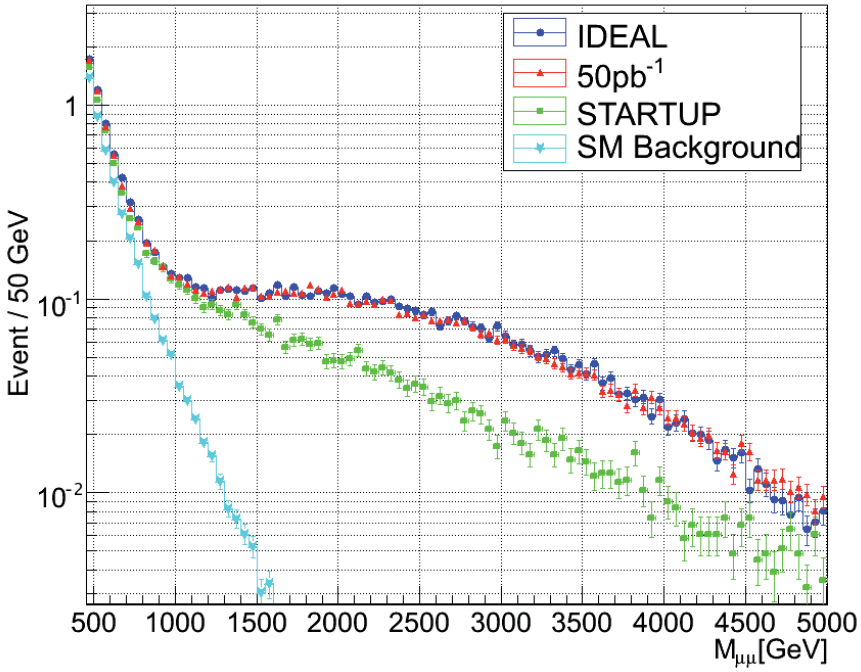

Figure 6.18: Di-muon invariant mass distribution for $\int \mathsf{L} = 100\,\mathrm{pb}^{-1}$ in three different alignment scenarios for global muons for a ADD Drell-Yan sample and the SM background. The IDEAL and $50\,\mathrm{pb}^{-1}$ CRAFT alignment scenarios are identical within the statistical uncertainty whereas the STARTUP scenario reproduces the $M_{\mu\mu}$ distribution very differently.

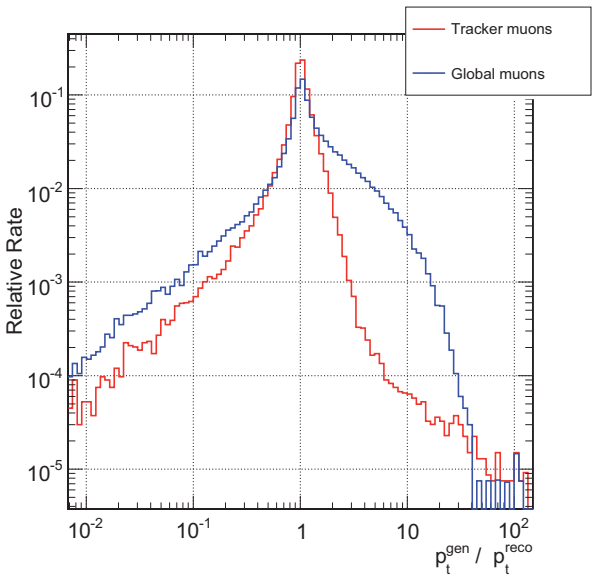

(a) STARTUP

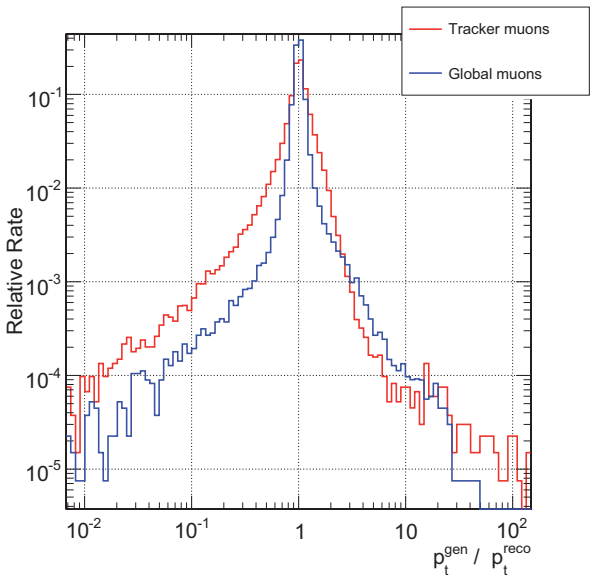

(b) $50\,\mathrm{pb}^{-1}$ CRAFT Alignment

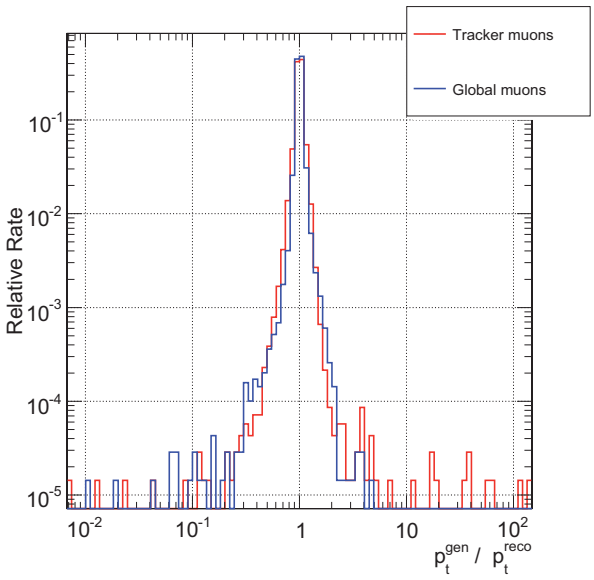

(c) IDEAL

Figure 6.19: Comparison of reconstructed and generated transverse momenta for one ADD Drell-Yan ($450\,\mathrm{GeV} < M_{\mu\mu} < 10\,\mathrm{TeV}$) sample. As shown the tracker only muons in the STARTUP scenario are mis-reconstructed with a lower probability compared to global muons. As the STARTUP and $50\,\mathrm{pb}^{-1}$ alignment use the same tracker alignment the tracker only muons are mis-reconstructed with the same probability in the CRAFT alignment scenario. The mis-reconstruction probability for global muons in the $50\,\mathrm{pb}^{-1}$ alignment is lower compared to tracker only muons.

Chapter 7

Analysis

After the reconstruction of the events of the Standard Model (SM) *background* and the LED *signal* (ADD) of the Monte Carlo events, the question arises, how the signal can be separated and identified in data. Therefore it is important to know how likely the background can fluctuate and "fake" a signal. The intermediate particles ($Z\,/\,\gamma*\,/G_{KK}$) are not directly detectable in data but only the final state (which is di-muon in this analysis), so a statistical decision has to be taken if a graviton signal is present according to the number of observed di-muon events and the integrated luminosity. To determine the significance of a potential signal different techniques and *estimators*[1] can be used. The parametrization of the total cross section has been done in Equation 3.4. Invariant di-muon mass $M_{\mu\mu}$ and decay angle $\cos\theta^*$ are analyzed in this chapter.

7.1 Hypothesis test

Hypothesis tests are methods to evaluate the statistical significance of observed data according to different competing hypotheses, and are used to distinguish between the *null* hypothesis H_0 and an *alternative* hypothesis H_1. The null hypothesis assumes that there is no signal whereelse the existence of a signal in addition to the background is described by the alternative hypothesis. The hypotheses are evaluated using a test statistic variable t which is calculated from the data. To estimate whether the observed data favors the null or the alternative hypothesis a critical value t_c has to be set [74]. In Figure 7.1 two different hypotheses are plotted, the *null* hypothesis H_0 and the *alternative* hypothesis H_1. After the choice of the critical value t_c, the areas α and β are fixed, shown in Figure 7.1. In statistics the area α is called rejection region of the *null* hypothesis and β is called the rejection region of the *alternative* hypothesis. E.g. t_c has been chosen so that β corresponds to 5 % (0.05) of the full integral of $f_{H_1}(t)$ (see Figure 7.1). So if the test statistic t, is in the rejection area of the alternative hypothesis β, the alternative hypothesis is rejected [2] with 95 % confidence level (CL). The more confident the rejection is supposed to be, the smaller β has to be set (by choosing t_c). If a 99 % CL is desired, β has to be chosen to be 1 % of the full integral of $f_{H_1}(t)$. So β is the conditional probability that t is less or equal to the critical value t_c for the alternative hypothesis, and α the conditional probability that t is greater or equal to the critical value t_c for the null hypothesis. This can be summarized as follows:

$$P(t \leq t_c|H_1) \quad = \quad \beta = \int_{-\infty}^{t_c} f_{H_1}(t)\mathrm{d}t, \tag{7.1}$$

$$P(t \geq t_c|H_0) \quad = \quad \alpha = \int_{t_c}^{\infty} f_{H_0}(t)\mathrm{d}t\ . \tag{7.2}$$

[1] An estimator is a statistical method to estimate statistical significances. Basic estimators like $\frac{s}{\sigma(b)}$ (signal count over fluctuation of the background) can be used to make a rational choice of cuts.

[2] Actually the alternative hypothesis is not rejected but one can only say that there has not been enough statistics to reject the null hypothesis.

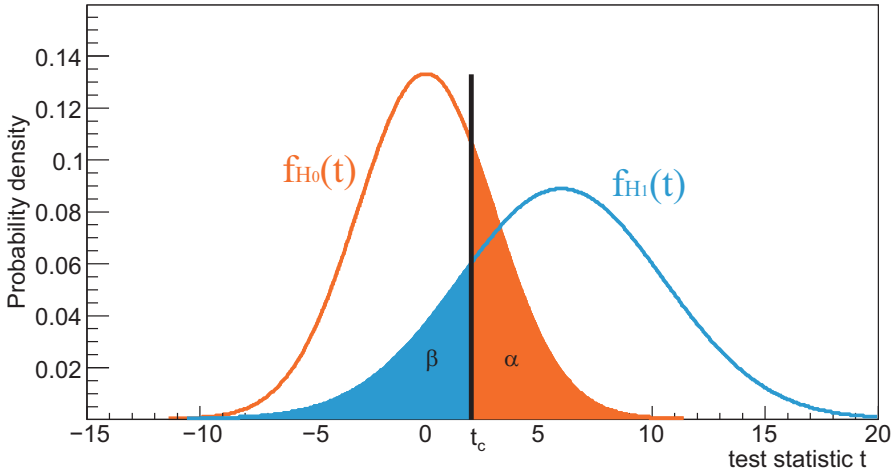

Figure 7.1: Null- and alternative hypothesis w.r.t the test statistics t. The two different hypotheses are analytically described by the functions $f_{H_0}(t)$ for the null- and $f_{H_1}(t)$ for the alternative hypothesis. Both functions are normalized to $f_{H_{1,2}}(t)$ and represent probability densities.

α and β are interpreted as confidence intervals and specify to which degree the rejection or acceptance of one hypothesis is statistically significant [75].

Generally two types of errors are distinguished concerning false rejection of the null hypothesis in favor of the alternative hypothesis and false rejection of the alternative hypothesis and keeping the null hypothesis. These two *errors* are summarized in Table 7.1.

	Conclusions from the hypothesis test	
Reality ↓	Do not reject H_0	Reject H_0
H_0 true	√	Type I Error
H_1 true	Type II Error	√

Table 7.1: Possible conclusions obtained from a hypothesis test. The Type I error is called a false discovery and the Type II error is called false exclusion.

7.1.1 Usage in particle physics

According to the Lemma of Neyman and Pearson [76] the separation power $(1-\beta)$ of a hypothesis test for small statistics is maximal if the test statistic is chosen to be the likelihood ratio

$$Q = \frac{L_{(s+b)}}{L_{(b)}} \tag{7.3}$$

of the null and the alternative hypothesis, where Q is the ratio of the likelihood functions of *signal + background*, $L_{(s+b)}$ and *background only*, $L_{(b)}$. In this analysis the SM will be treated as null hypothesis (*background only*) and the ADD theory as alternative hypothesis *signal + background*, $L_{(s+b)}$. Another advantage of the likelihood ratio Q is that it can be used to combine different search channels, which can be different distributions, e.g. invariant di-muon mass and the decay angle θ^*, or even entirely different experiments (e.g. combination of data which has been collected in different detectors). Combining $i = 0, 1, ..., N$ search channels the test statistic Q then can be written as [77] :

$$Q = \prod_{i=1}^{N} Q_i \tag{7.4}$$

The CL_S-method (also called the modified frequentist approach [78]) is one way to implement a hypothesis test in particle physics. In this method the negative log likelihood ratio $t = -2\ln Q$ is used as test statistic [3]. In Figure 7.2 the alternative (*signal + background*) hypothesis is described

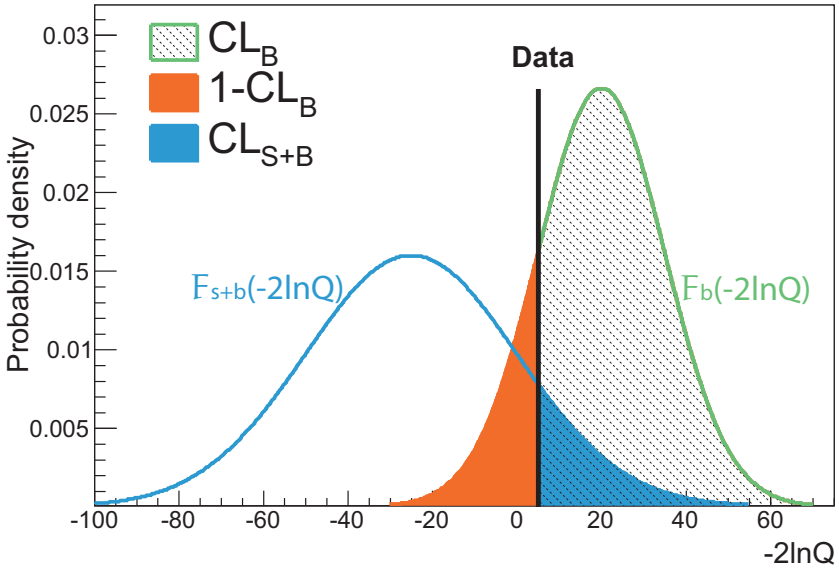

Figure 7.2: $-2\ln Q$-distribution for *signal + background* and *background only*. The test statistic value t_{data} of the data point separates the regions of rejection, named CL_{S+B} (corresponding to β) and $1 - CL_B$ (corresponding to α). The *signal + background* hypothesis is described by the normalized distribution $\mathcal{F}_{s+b}$ and the *background only* hypothesis by $\mathcal{F}_b$.

by the normalized blue distribution, named $\mathcal{F}_{s+b}(-2\ln Q)$ where the null (*background only*) hypothesis is described by the green one, named $\mathcal{F}_b(-2\ln Q)$. Both distributions are shown for the test statistic $t = -2\ln Q$. The test statistic value t_{data} of the $-2\ln Q$ distribution is calculated from the data point (Section 7.1.2).

Comparing Figure 7.2 with Figure 7.1 the following relation can be found:

$$1 - \alpha = \mathrm{CL_B} = \int_{x_{\mathrm{Data}}}^{\infty} \mathcal{F}_b(x)\mathrm{d}x, \tag{7.5}$$

$$\beta = \mathrm{CL_{S+B}} = \int_{x_{\mathrm{Data}}}^{\infty} \mathcal{F}_{s+b}(x)\mathrm{d}x, \tag{7.6}$$

where x is the substitution for $-2\ln Q$ and $\mathcal{F}_{b,s+b}(x)$ are the normalized distributions of the *background* and of *signal + background*. Conventionally the limits for discovery and exclusion are set as follows in the CL_S-method: If the region of rejection of the *background only* distribution (area to the left of the data point) is

$$1 - \mathrm{CL_B} < 2.85 \cdot 10^{-7}, \tag{7.7}$$

which corresponds to $5\,\sigma$ confidence level of a one sided Gaussian distribution, the data is claimed to be incompatible with the *background only* hypothesis .So in a frequentistic sense this means

[3] This choice of test statistic has some advantages for computational needs. The logarithm reduces the amplitude of the likelihood function but as a monotone function it does not change the position of the likelihood's extrema. Most computer algorithms are trained to minimize numerically, so instead of maximizing the likelihood, the negative likelihood can be minimized. The factor 2 is added to the definition to make it more similar to the χ^2-value.

that the background does look like the observed data with a probability of $\sim 2 \cdot 10^{-7}$ only. If a discovery is not possible an exclusion limit can be set with 95 % CL corresponding to $1.96\,\sigma$ confidence level of a one sided Gaussian distribution. In the CL_S-method the exclusion limit is therefore set as:

$$CL_S = \frac{CL_{S+B}}{CL_B} < 0.05, \tag{7.8}$$

which is more conservative than setting only $CL_{S+B} < 0.05$ in order to reduce unphysical occurrences described in [77]. As shown in Figure 6.9, the event counts in this analysis are very small. Many analyses in the CMS collaboration therefore require additionally a minimum of five signal events $N_S > 5$ in order to avoid the optimization of the analysis to regions (in the di-muon or another distribution) where the exclusion of one parameter point is possible earlier than discovery w.r.t. the integrated luminosity. This has also been investigated and discussed (shown in Figure 7.14) in this analysis.

7.1.2 Technical Implementation

In reality when the CMS detector will take data there will only be one value of $-2\ln Q$, the data point in Figure 7.2 (the marked data line). To estimate the the prior probability density of the $-2\ln Q$ distribution numerous toy-Monte Carlo experiments have to be performed.
In this study the HybridCalculator of the RooStats CMS-package [79] has been used. The HybridCalculator uses extended log likelihood ratios [80] as test statistic with:

$$L_{ext} = \frac{e^{-\nu}\nu^N}{N!} \prod_{i=1}^{N} f(x_i), \tag{7.9}$$

where $f(x_i)$ is the (conditional) normalized probability density function (p.d.f.), the number of expected events (mean) ν, and the number of observed events (data points) N, where x is the variable depending on the distribution (in this study the invariant di-muon mass). As N is the total number of observed events in the whole distribution, the HybridCalculator estimates this value by dicing N w.r.t. a Poisson distribution with the mean value ν. The extended log likelihood L_{ext} describes both, the different numbers of events in the signal [4] region of the *background only* and *signal+background* distribution (therefore the normalization factor of extended log likelihood is used), and the shapes of the *background only* and *signal + background* distributions.

The test statistic $-2\ln Q$ then assumes the final form:

$$-2\ln Q = -2\ln \frac{L_{ext}(s+b)}{L_{ext}(b)}, \tag{7.10}$$

$$-2\ln \prod_{i=1}^{N} Q_i = -2\ln \left(\frac{\frac{e^{-\nu_{s+b}}\nu_{s+b}^N}{N!}}{\frac{e^{-\nu_b}\nu_b^N}{N!}} \prod_{i=1}^{N} \frac{f_{s+b}(x_i)}{f_b(x_i)} \right). \tag{7.11}$$

Here N denotes how often the HybridCalculator dices data points into the p.d.f. $f_{s+b,b}(x_i)$ for each $-2ln$Q of the *background only* and *signal+background* hypotheses by performing toy-Monte Carlo experiments and so represents a fixed number.

7.2 Systematic Uncertainties

Another feature of the HybridCalculator is the treatment of systematic uncertainties. They can be implemented as prior probability densities, which means that systematic uncertainties are not due to a fluctuation in the statistics but more a lack of knowledge in the experiment. A prior probability distribution is a probability distribution representing knowledge about an unknown quantity before any data have been observed. The unknown quantity can be a parameter or a hypothesis. In this study the following systematic uncertainties have been taken into account:

[4] Region of the invariant di-muon mass which is used to study the existence of LEDs.

- **Luminosity**. Since the luminosity and the event rate is connected by the equation :

$$N_{\text{Event}} = \mathsf{L}_{int} \cdot \sigma, \tag{7.12}$$

a precise knowledge of the luminosity is needed. For early data two measurement techniques can be used.
First one is the measurement of the luminosity according to Equation 4.2:

$$\mathsf{L} \sim \frac{1}{\sigma_x \sigma_y} \tag{7.13}$$

directly by scanning the width of the beam spot σ_x and σ_y [81]. Due to the uncertainties of the tails of the beam spots for the first runs of the LHC, σ_x and σ_y can not be measured well enough to estimate the luminosity in a range better than (8-10) %.
Another possibility is to use a very well calculated process like the inclusive Z-production. The electroweak physics group of CMS [82] estimated the uncertainty of the cross section of the Drell-Yan process for early data ($\sim 100\text{pb}^{-1}$) [83]. For a luminosity of $\int \mathsf{L} = 45\,\text{pb}^{-1}$ it is expected to be able to measure the cross section with an uncertainty of less than 3 %. Taking into account the theoretical uncertainty of the Z-boson production cross section at the Z-peak, a 5 % luminosity uncertainty is a reasonable expectation.

- **Cross sections**. Although the cross section for the Z-peak is calculated very precisely, the cross section in the tails of the high invariant di-muon mass region has a high theoretical uncertainly. They are due to the rising PDF (Parton Distribution Function) uncertainties which have been recently studied by the CMS TeV Muon reconstruction group [84]. The PDF uncertainties were calculated using the LHAGLUE interface to the parton distribution functions library LHAPDF [85]. The CMS TeV Muon reconstruction group generated 26 Drell-Yan di-muon samples with masses from 40 to 6000 GeV at a center of mass energy of $\sqrt{s} = 14\,\text{TeV}$ and applied a reweighting technique with asymmetric errors [86]. The transformation has been done to the $\sqrt{s} = 10\,\text{TeV}$ scenario in 2009 [87]. At invariant masses $M_{\mu\mu}$ of 700 GeV or higher the uncertainty is rising from 15 % at 700 GeV to 19 % at $M_{\mu\mu} >$ 2500 GeV. Although the PDF uncertainties have been studied for the SM Drell-Yan process only, the same uncertainly for the ADD signal is reasonable.
Unfortunately the CKKW merging method has not been validated for the ADD implementation in SHERPA so far, and therefore only the $2 \rightarrow 2$ process without additional jet will be used (Figure D.1). The next to leading order (NLO) QCD corrections of the Drell-Yan process have been calculated w.r.t. the differential cross section as a function of the invariant di-muon mass [88]. They have been applied to the produced Monte Carlo samples for the ADD and the SM processes shown in Figure 7.3. Overall an uncertainty of up to 25 % is realistic for the NLO cross section for both SM Drell-Yan and ADD Drell-Yan for invariant di-muon masses of 800 GeV and higher at $\sqrt{s} = 10\,\text{TeV}$.

- **Shape uncertainty.** The uncertainty of the shape of the invariant di-muon mass distribution is estimated by a comparison of two different Drell-Yan samples with a di-muon final state. Therefore the private production of SHERPA samples has been used and compared with the event generator PYTHIA. As the uncertainty of the tails are important, the Z-peak has been used to normalize the samples to each other. The resulting difference is according to the considered bin of the magnitude of up to factor two to three as shown in Figure 7.4. This difference has been parametrized (shown in Figure D.4) and used as uncertainty in each corresponding bin.

- **Extrapolation of the CL_B-distribution.** In practice it is difficult to perform the toy-Monte Carlo experiments more than $2 \cdot 10^7$ times which is necessary to estimate the significance of a possible discovery. As in the critical region 1-CL_B the probability density of the -2lnQ-distribution of the background is very low (Figure 7.2), the toy-Monte Carlo

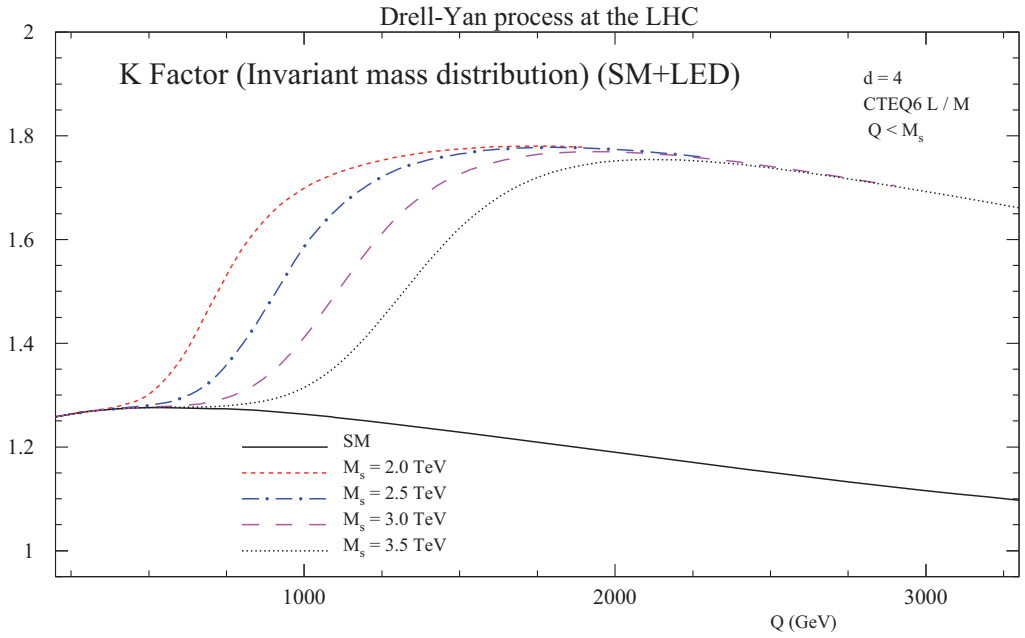

Figure 7.3: QCD NLO corrections for SM and shown ADD parameter points [89].

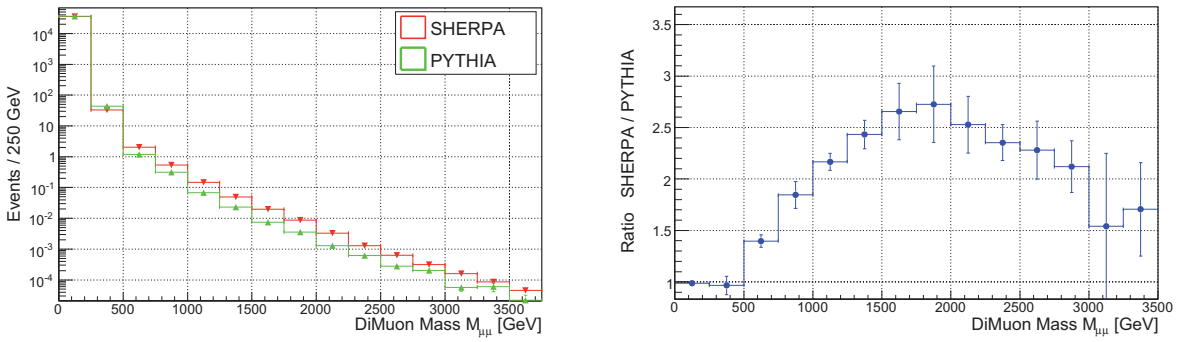

(a) Shapes of SHERPA and PYTHIA

(b) Ratio SHERPA / PYTHIA

Figure 7.4: Comparison of SHERPA and PYTHIA Drell-Yan processes in di-muon final state for $100\,\mathrm{pb}^{-1}$. The absolute difference of the shown distributions has been parametrized and taken into account as systematic uncertainty.

statistics is insufficient in that region. Thus an extrapolation of the $\mathrm{CL_B}$ distribution is needed. The extrapolation of the $\mathrm{CL_B}$-distribution is done with an exponential function. As small deviations of the fit cause a large change in the discovery significance (shown in Figure 7.5), this fit has to be validated before. This has been done by performing once at least two million toy-Monte Carlo experiments (running for at least one week on the local computer) for each parameter point of the lowered fundamental scale M_f. The most robust fit has been estimated considering the quantity χ^2/ndf of the fit and by comparing the significance with other estimators such as the p_N estimator of the Aachen MUSiC group [90].

- **Limited number of MC statistics.** The statistical error of each bin of a certain distribution is dependent on the number of simulated MC events N_{Sim}. The number of expected events nevertheless is given by the relation $N_{\mathrm{Exp}} = \mathsf{L}_{int} \cdot \sigma$. N_{Sim} and N_{Exp} are

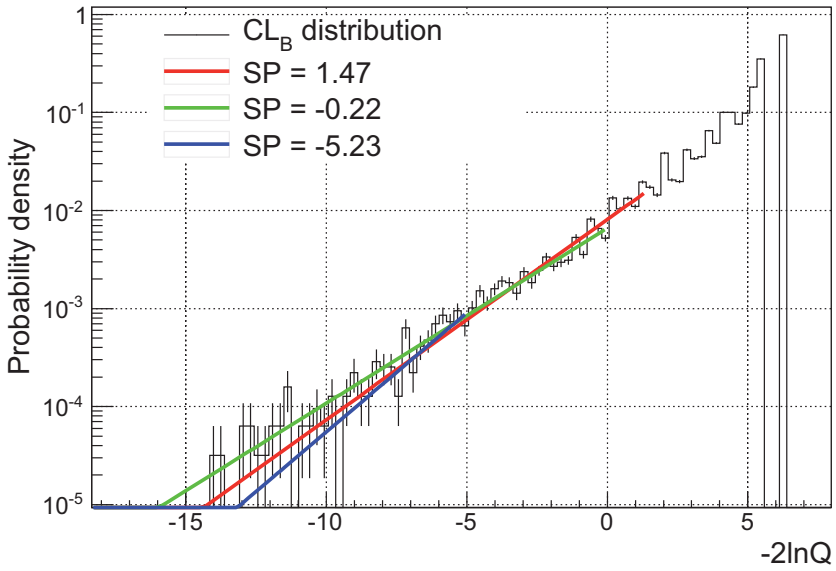

Figure 7.5: Systematic uncertainty of the extrapolation of the CL_B-distribution. Three fits with different starting points (SP) and their extrapolations are shown. All extrapolations have been fitted with an $\chi^2/ndf < 1.6$.

not necessarily equal. Thus each simulated event has an additional uncertainty of a factor:

$$\xi = N_{\text{Exp}}/N_{\text{Sim}} = \mathsf{L}_{int} \cdot \sigma / N_{\text{Exp}}. \tag{7.14}$$

This uncertainty is negligible in this study as the ratio of expected and simulated events $\xi = N_{\text{Exp}}/N_{\text{Sim}}$ is of the order of 10^{-4}. This will be discussed further in Section 7.4.

All these priors are implemented as Gaussian distributions (characterized by the expectation value (mean) and the standard deviation (width)) for which the width is chosen as the relative respective uncertainty. The technical implementation is as follows. E.g. the prior probability density of the luminosity is handled by a Gaussian distribution where the mean is set to the expectation value (the corresponding luminosity for which the CL_B is evaluated at). The uncertainty of the luminosity is set as the standard deviation of this Gaussian distributions. So the value of the luminosity is diced according the Gaussian distribution for every toy-Monte Carlo experiment. In the CL_S-method the systematic uncertainties broaden the CL_{S+B} and CL_B distributions.

7.3 Invariant Di-muon Mass Distribution Analysis

The invariant di-muon mass distribution is the most promising analysis channel for the search of LED as shown in 7.6 and has been used for the di-muon analysis at Tevatron only. As no uncertainty due to a limited number of MC statistics has been taken into account, a cut on the $M_{\mu\mu}$-distribution has to applied in order not to be sensitive to statistical fluctuations, e.g. in the region of the Z-peak. The best separation can be achieved for a cut on $M_{\mu\mu}$ at 650 GeV as the distributions for SM and ADD at that invariant mass begin to separate. The mass where the separation gets relevant of course depends on the parameter point but a variation of the cut on $M_{\mu\mu}$ between 600 GeV and 800 GeV has negligible impact on the significance. So only events with $M_{\mu\mu}$>650 GeV are used for this analysis.

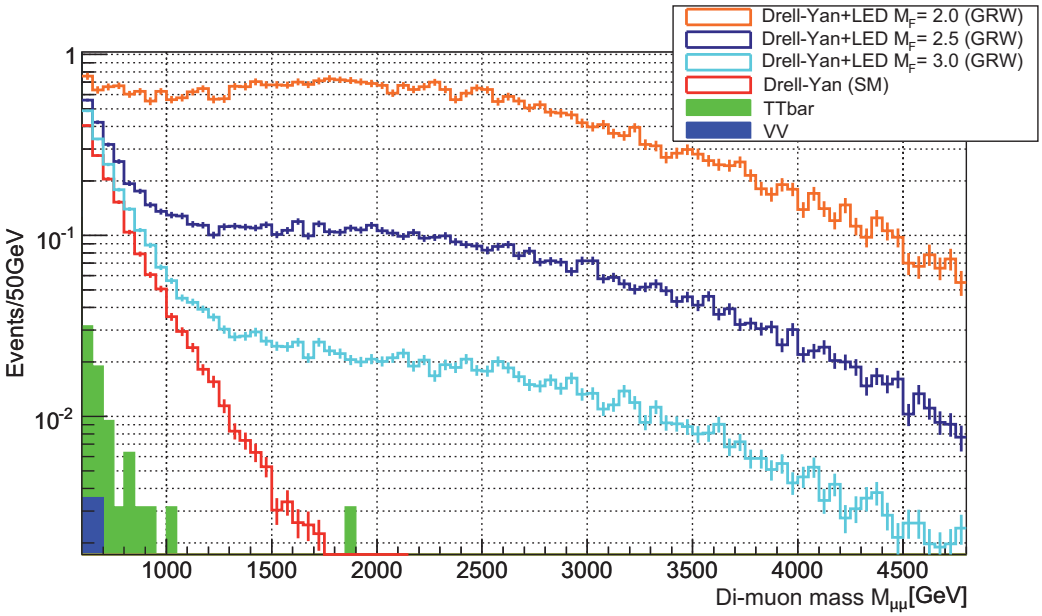

Figure 7.6: The invariant di-muon mass distribution in the signal region for an integrated luminosity of $100\,\mathrm{pb}^{-1}$.

7.4 Decay Angle Distribution Analysis

The theory of LEDs predicts a different angular distribution of the di-muon pair compared to the Drell-Yan process in the SM. The decay angle $\cos\theta^*$ (as defined in chapter 6.3) has been calculated [91, 92] and its distribution is shown in Figure 7.7. Where the SM Drell-Yan vector boson exchange results in the known $1+\cos^2\theta^*$-distribution, the decay angle of the ADD theory is different as the graviton is a spin 2 particle. Also for the different initial state particles (gluon + gluon or quark + anti-quark) the decay angle assumes different distributions.

So the processes $gg \rightarrow G_{KK} \rightarrow f\bar{f}$ and $q\bar{q} \rightarrow G_{KK} \rightarrow f\bar{f}$ lead to different distributions w.r.t. the decay angle $\cos\theta^*$. The contributions of gg and $q\bar{q}$ depend on the mass of the decaying graviton [91], as shown in Figure 7.8.

Different cuts an the invariant di-muon mass have been applied in order to illustrate the $\cos\theta^*$ distribution. This has been done with reconstructed events and also with events on generator level to estimate the reconstruction effects of the CMS detector, as shown in Figure 7.9.

It can be seen that the higher the invariant di-muon mass cut the more the ADD and SM distributions describe different shapes as predicted in the figures 7.7 and 7.8. As discussed, these differences are due to the spin of the graviton which is not present in the SM. But these plots have been obtained with 100 000 generated events according to an integrated luminosity [5] of $500\,\mathrm{fb}^{-1}$. Even then, shapes for ADD and SM for an invariant di-muon mass higher than 3500 GeV are dominated by statistical fluctuations, as shown in Figure (7.9, e and f) as the cross section drops with the invariant di-muon mass. This channel is therefore not advantageous for the first data being taken but is promising for analyses with more statistics in a combined channel with the invariant di-muon mass.

[5] The parameter point GRW, $M_f = 2.5\,\mathrm{TeV}$ has a total cross section of $\sim 0.2\,\mathrm{pb}$ for a generator cut on the invariant di-muon mass of (450 to 10 000) GeV.

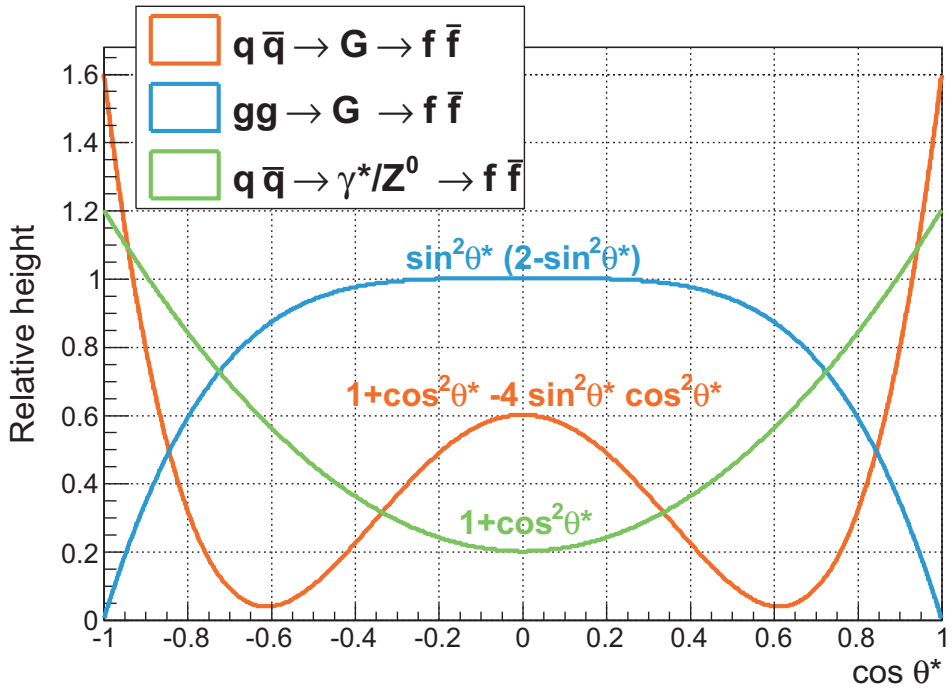

Figure 7.7: Decay angle $\cos\theta^*$-distribution for the processes $gg \to G_{KK} \to f\bar{f}$ and $q\bar{q} \to G_{KK} \to f\bar{f}$. For comparison the SM prediction is also shown. The distributions are only depending on the spins and orbital angular momenta of the interacting particles.

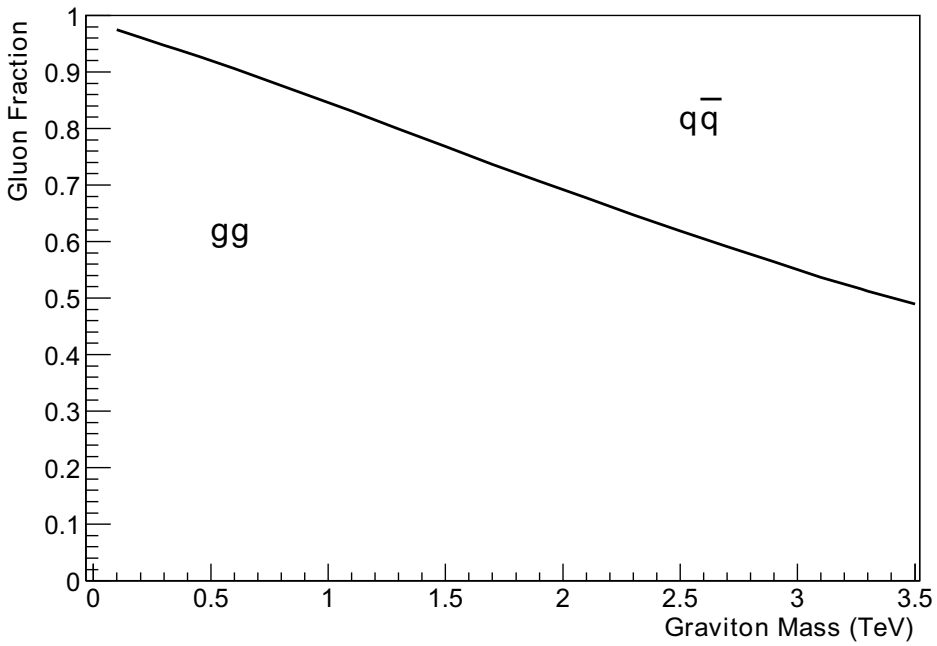

Figure 7.8: Contribution of gluon-gluon and quark-antiquark fusion for graviton production w.r.t. the graviton mass in the ADD theory [91].

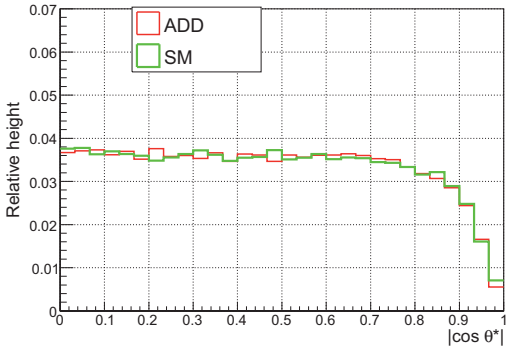

(a) di-muon mass $> 150\,\text{GeV}$ Generated, $|\eta| < 2.1$

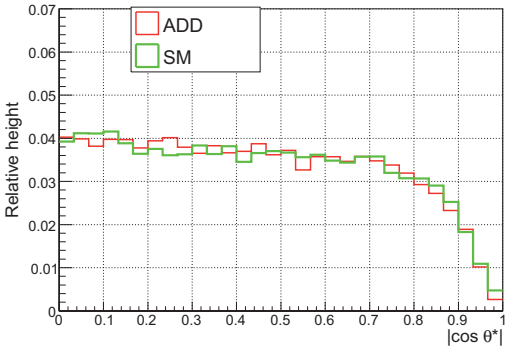

(b) di-muon mass $> 150\,\text{GeV}$ Reconstructed, $|\eta| < 2.1$

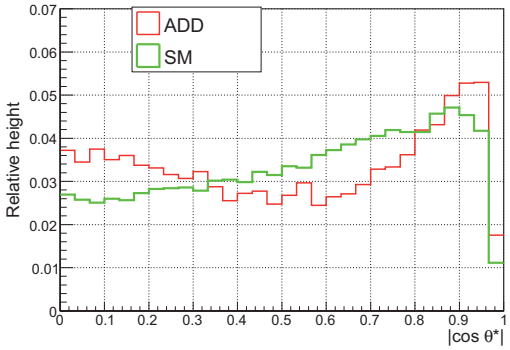

(c) di-muon mass $> 2500\,\text{GeV}$ Generated, $|\eta| < 2.1$

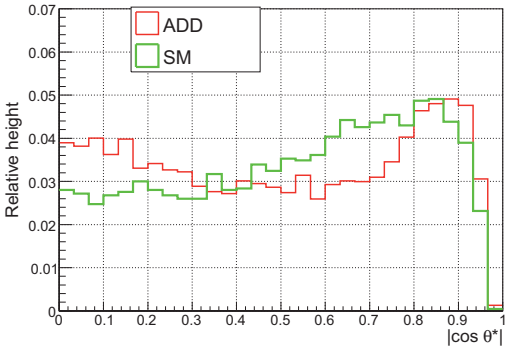

(d) di-muon mass $> 2500\,\text{GeV}$ Reconstructed, $|\eta| < 2.1$

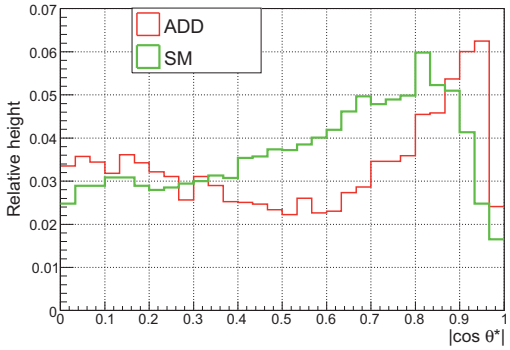

(e) di-muon mass $> 3500\,\text{GeV}$ Generated, $|\eta| < 2.1$

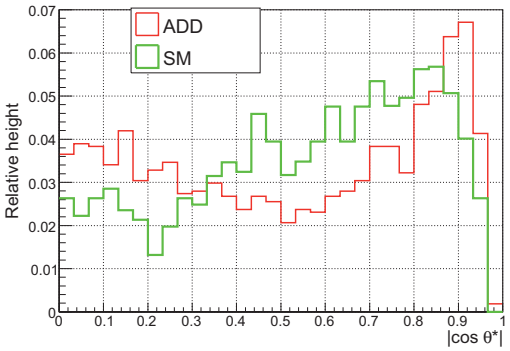

(f) di-muon mass $> 3500\,\text{GeV}$ Reconstructed, $|\eta| < 2.1$

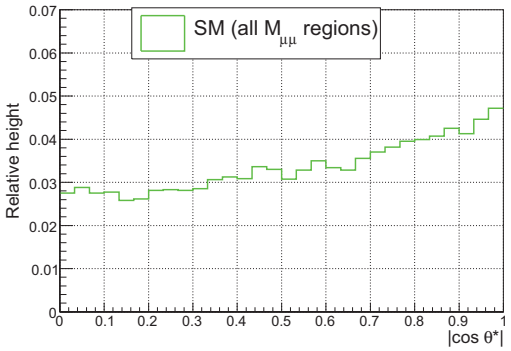

(g) SM $|\cos\theta^*|$ for all $M_{\mu\mu}$ regions Generated, no η-cut

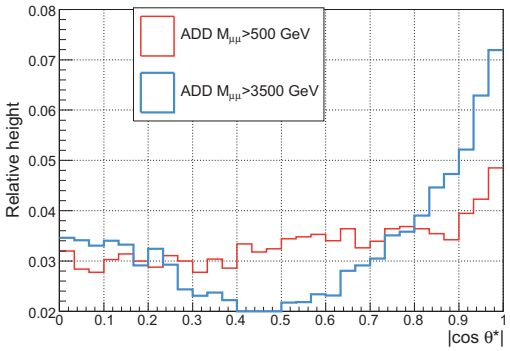

(h) ADD $|\cos\theta^*|$ Generated, no η-cut

Figure 7.9: Comparison of the decay angle $|\cos\theta^*|$ at generator level and after reconstruction (for both an $|\eta| < 2.1$ has been applied). ADD in the legend always means SM+LED. With rising invariant di-muon mass cut the contribution of the SM is suppressed for the ADD scenario. Sub-figures (g) and (f) represent the $\cos\theta^*$ distributions on generator level without $|\eta|$-cut.

7.5 Cut optimization

To utilize the different angular distributions of ADD and SM, a possible cut on the pseudorapidity η has been investigated. As shown in Figure 7.10 the muons from the graviton G_{KK} are produced

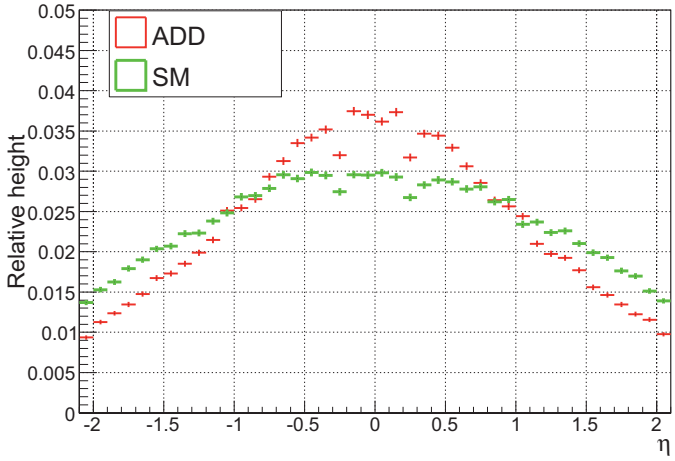

Figure 7.10: Comparison between the η-distributions predicted by the ADD model (here M_f = 2.0 TeV) and in the SM, for invariant di-muon masses $M_{\mu\mu}$> 650 GeV.

more in central (small values of $|\eta|$) direction. This has been used to investigate if it is beneficial to narrow the η-region in order to gain a better *signal* to *background* ratio. The estimator $N_{signal}/\sigma(N_{background})$ (number of signal events over background fluctuations) has been used with the uncertainties explained in the previous section (the dominant cross section error $\sim$ 25% is added to the statistical error in quadrature). The results are shown in Figure 7.11. As the ADD

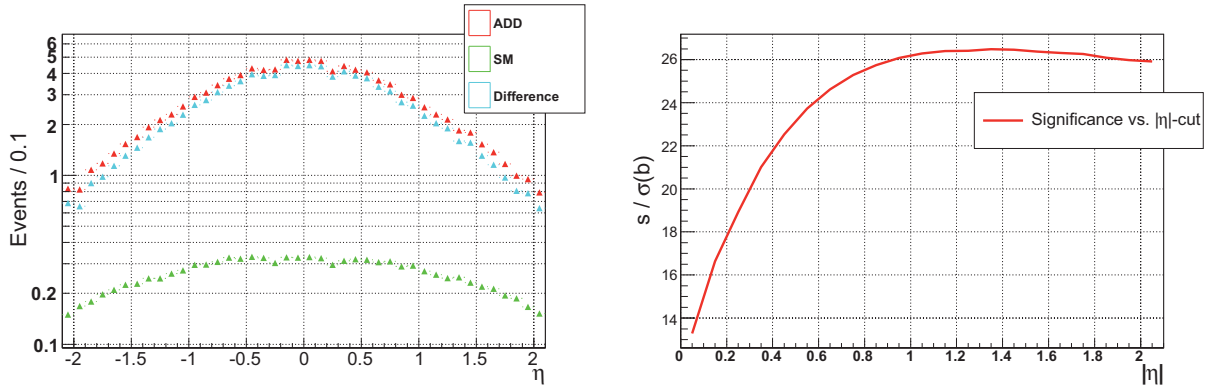

(a) Differences of the η-distributions of ADD and SM for $M_{\mu\mu}$>650 GeV

(b) $signal/\sigma(background)$ as function of the corresponding η-cut

Figure 7.11: The significance of a narrower $|\eta|$-cut is shown. As ADD parameter point the M_f = 2.0 TeV sample has been chosen for an integrated luminosity of 100 pb^{-1}.

samples contain both, graviton and SM contribution, the SM and ADD distribution have been subtracted to obtain the pure graviton couplings. Due to the interference of the graviton and SM gauge boson as shown in the theory chapter, this procedure is not entirely correct but sufficiently accurate to estimate the graviton contributions. For $|\eta| > 1$ the significance is nearly flat. The highest significance can be achieved by cutting symmetrically at $|\eta| = 1.35$. As the changes of the significances are very small, and the event rate is reduced additionally by any cut on $|\eta|$ (for discovery at least five events for signal+background are required) this cut is not too promising for

early data analyses. For higher integrated luminosities, this extra information may be beneficial to characterize the potential signal and help to separate the graviton contribution from the SM Drell-Yan process.

7.6 Expected Sensitivity and Limits for early data

The ADD samples have been produced in the GRW [17] convention which does not depend on the number of extra dimensions but only on the lowered fundamental scale M_f. The investigated parameter points have been chosen as M_f = 2.0 TeV, 2.5 TeV, 3.0 TeV, 3.5 TeV, and 4.0 TeV. Under the premise that the generated Monte Carlo samples are correctly characterizing the ADD and the SM di-muon distributions, the $-2\ln Q$-value of the data point, $-2\ln Q_{\text{data}}$, is set to the median of the CL_{S+B}-distribution for the estimation of the discovery potential and to the median of the CL_B-distribution to estimate the exclusion potential. This has to be done as there is no experimental data available yet. So with a 50 % probability the real data point is higher or lower than $-2\ln Q_{\text{data}}$. The values of $-2\ln Q_{\text{data}}^{\pm 1\sigma}$ points (84 % or 16 %) and $-2\ln Q_{\text{data}}^{\pm 2\sigma}$ points (97.5 % or 2.5 %) have been set as data points as well to estimate the σ bands of the sensitivity within the uncertainties shown in Figure 7.12. This is necessary to estimate the impact of a (statistical) fluctuation of the $-2\ln Q_{\text{data}}$ point of real data. The width of the these σ bands depend on the

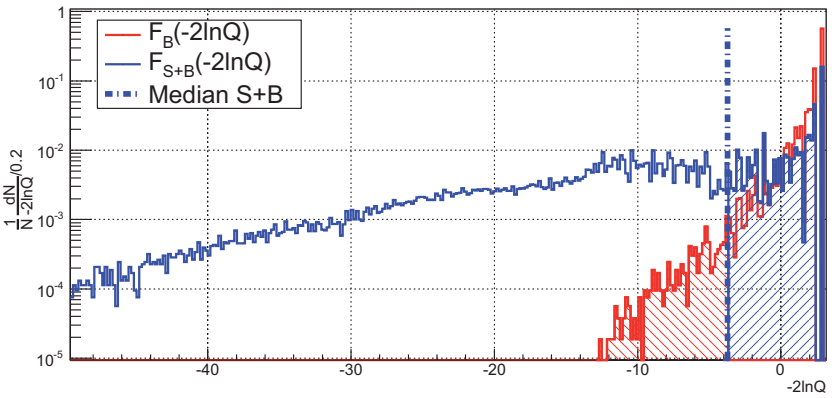

(a) $M_f = 2.5$ TeV and $\int \mathsf{L} = 100\,\text{pb}^{-1}$.

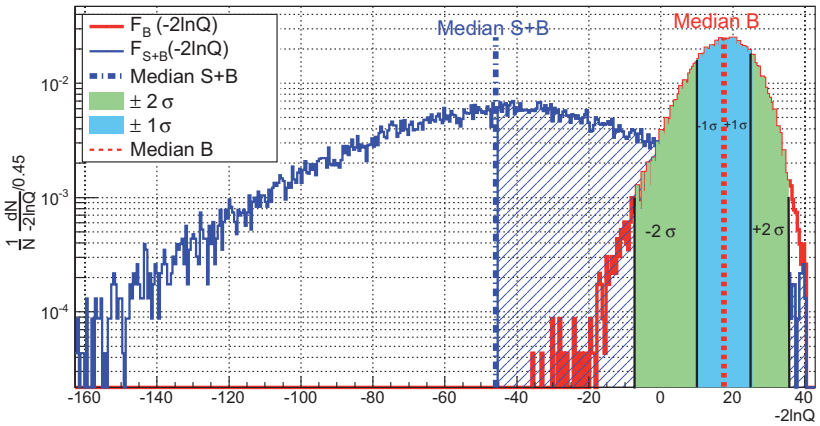

(b) $M_f = 3.5$ TeV and $\int \mathsf{L} = 1500\,\text{pb}^{-1}$. Also the $-2lnQ$-points for the 1σ and 2σ band are shown.

Figure 7.12: -2lnQ-distribution for two different parameters of the lowered fundamental scale M_f and luminosities. Also the $-2\ln Q$ positions the $1\,\sigma$ and $2\,\sigma$ width are taken as data points (have also to be set to the right of the median to get the two sided σ band).

statistical uncertainty (intrinsic width of the CL_{S+B} and CL_B-distribution) and on the systematic

uncertainties as they broaden the CL_{S+B} and CL_B distributions.

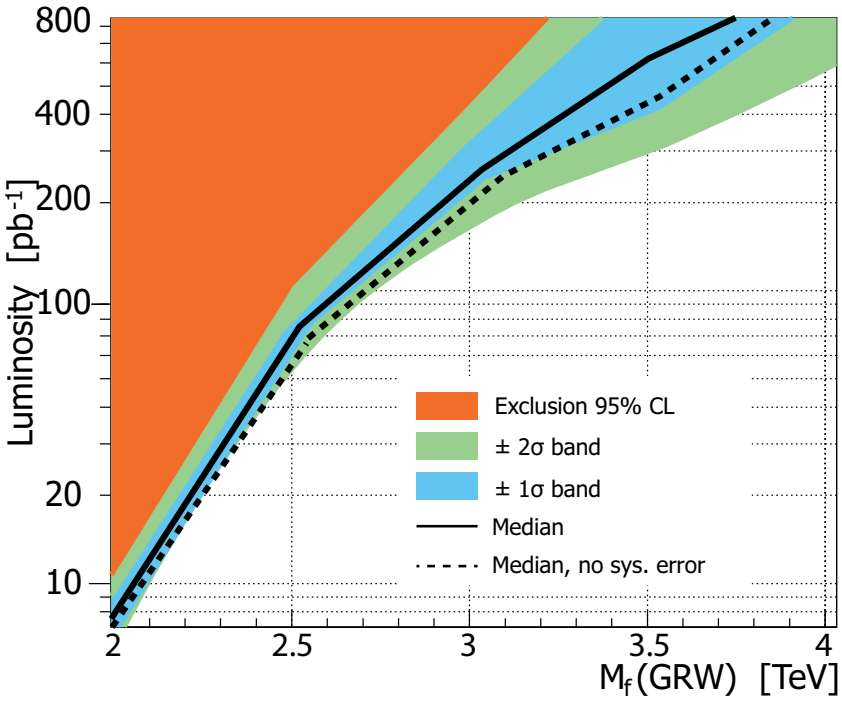

Figure 7.13: Exclusion limits for M_f as a function of the integrated luminosity for 95 % confidence level (1.96 σ).

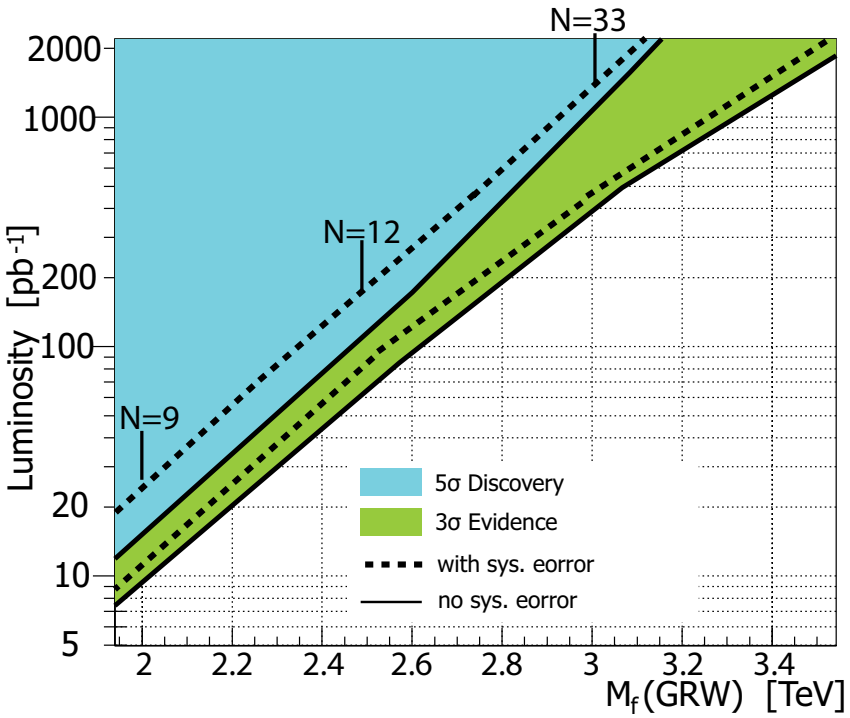

Figure 7.14: Discovery limits for M_f as a function of the integrated luminosity for 3 σ and 5 σ confidence level. N denotes the total number of observed signal events at the given point.

The luminosity dependency of the exclusion and discovery limit is shown in figures 7.13 and 7.14. For low luminosities up to $\sim 60\,\mathrm{pb}^{-1}$ the statistical uncertainty due to a low number of expected events is dominating the exclusion limit, whereas for high luminosities the σ-bands are getting wider significantly. This is due to the very large systematic uncertainties which have been taken into account for this analysis. They are clearly dominating the sensitivity of this study for integrated luminosities above $\sim 200\,\mathrm{pb}^{-1}$. As shown in figures 7.13 and 7.14 an integrated luminosity of less than $20\,\mathrm{pb}^{-1}$ will be sufficient to extend the highest recent limits set by the DØ experiment of $M_S = 1.66\,\mathrm{TeV}$.

To compare the results with other analyses it is necessary to convert the shown parameter point of the fundamental scale into the HLZ convention. Therefore the Formula 3.5 can be used:

$$\frac{1}{M_S^4(GRW)} = \frac{F}{M_S^4(HLZ)}, \tag{7.15}$$

$$\sqrt[4]{F \cdot M_S^4(GRW)} = M_S(HLZ), \tag{7.16}$$

where F can be written as:

$$F = \begin{cases} \log\left(\frac{M_S^2}{\hat{s}}\right) & n = 2 \\ \\ \frac{2}{n-2} & n > 2 \end{cases} \text{(HLZ)}. \tag{7.17}$$

The variable $\hat{s} = s \cdot x_1 \cdot x_2$ represents the center of mass energy of the parton-parton interaction and is different for every collision which took place, as the momentum fraction of the partons $x_{1,2}$ is different in every collision. So the transformation to HLZ for two extra dimensions $n = 2$ is not directly calculable from Formula 3.5. To conversion into the HLZ ($n = 2$) case has been done by running SHERPA several times in the HLZ convention for two extra dimensions at different fundamental scales and comparing the cross section generated by SHERPA . Once the cross section of a fixed fundamental scale M_S in the GRW convention and in the HLZ convention for $n = 2$ are equal, the GRW limit can be transformed to HLZ ($n = 2$). The values of discovery and exclusion for an integrated luminosity of $\int \mathsf{L} = 100\mathrm{pb}^{-1}$ for the GRW and HLZ conventions are listed in Table 7.2:

	M_S(GRW) [TeV]	M_S(HLZ)[TeV]				
Expected potential for $\int \mathsf{L} = 100\,\mathrm{pb}^{-1}$		n=2	n=3	n=4	n=5	n=6
95 % exclusion	2.65	2.81	3.15	2.65	2.39	2.22
$5\,\sigma$ discovery	2.3	2.43	2.74	2.3	2.08	1.93

Table 7.2: Conversion of the lowered fundamental scale M_S from GRW to HLZ for $\int \mathsf{L} = 100\mathrm{pb}^{-1}$.

As shown in Figure 7.14, the signal events $\mathrm{N_S}$ for each parameter point does not drop below the threshold of $\mathrm{N_S} = 5$ so that this criterion does not to be considered at all.

Chapter 8

Conclusions

The theory of extra dimensions in the ADD model predicts an interesting experimental signature for virtual graviton exchanges in high energy scattering processes. As discussed in this study, the di-muon pair production is a clean signature in CMS. Already with an integrated luminosity of $100\,\mathrm{pb}^{-1}$ at a center of mass energy of $\sqrt{s} = 10\,\mathrm{TeV}$ the recent limits of the lowered fundamental scale M_f can be extended. As also to some extend the systematic uncertainties (e.g. the luminosity and the cross section uncertainties) will be reduced with continuous data taking, the CMS experiment will be able to investigate the ADD model to a high degree. The matrix element generation framework SHERPA has been used and compared to theoretical predictions as the NLO QCD corrections of the Drell-Yan process. All relevant backgrounds have been studied with the conclusion that the SM Drell-Yan process is the only dominant background. The applied cuts have been discussed with the aim to achieve the best possible separation of the signal from the background. Concerning the impacts of the misaligned CMS detector, three different alignment scenarios have been investigated and compared. The discovery and exclusion potential has been estimated with the $\mathrm{CL_S}$-method where all relevant systematic uncertainties have been taken into account. The results have been compared with the CMS Note AN-2009/062 [93] where the di-photon channel has been studied. As the branching ratio $\frac{G_{KK}\to\gamma\gamma}{G_{KK}\to\mu^+\mu^-}$ of the KK graviton is twice as high for di-photons compared to di-muons, also the event rates for di-photons are twice as high. But due to the better reconstruction efficiency of the CMS detector for muons than for photons, the channels are comparable in the sensitivity. According to [93] the di-photon channel is slightly more sensitive than the di-muon channel. A comparison has also been done to the analysis presented in the Physics TDR of the CMS detector [30]. This analysis has been done with a center of mass energy of $\sqrt{s} = 14\,\mathrm{TeV}$. For the same integrated luminosity the $\sqrt{s} = 14\,\mathrm{TeV}$ analysis is able to set almost twice as high exclusion and discovery limits compared to the presented $\sqrt{s} = 10\,\mathrm{TeV}$ study.

As this study uses the Z-peak for calibration purposes, the presented analysis can also be used to understand the CMS detector for the very first collisions to measure the SM precisely.

Appendix

Appendix A

Sample production in SHERPA 1.1.2

The kinematic cuts and the decay chain to be specified needs to be set in SHERPA as follows:

```
(processes){
%-----------------------------------------------------
%-- Processes to calculate ---------------------------
%-----------------------------------------------------
%
% jet jet -> muon- muon+ + (n-jets)
%
  Process : 93 93 -> 13 -13 93{1}
  Order electroweak : 2
  Print_Graphs
  End process
%
}(processes)
(selector){
!-----------------------------------------------------
!-- Parton level selectors ---------------------------
!-----------------------------------------------------
  JetFinder   sqr(20/E_CMS) 1.
  Mass 13 -13 500 10000
}(selector)
```

Appendix B

Measurement of the transverse momentum of muons in the muon system

A particle of charge Q and velocity $\vec{v}$ experiences a force $\vec{F}$ in a magnetic field $\vec{B}$:

$$\vec{F} = Q\vec{v} \times \vec{B} \tag{B.1}$$

So only the perpendicular part of the velocity (momentum) experiences the force. Comparing this force with the centripetal force, the equation assumes the form:

$$F = \frac{dp_t}{dt} \quad \text{hence} \quad p_t = \gamma m v_t \rightarrow \frac{p_t}{dt} = \gamma m \frac{dv_t}{dt} \tag{B.2}$$

$$\frac{dv_t}{dt} = \frac{v_t^2}{r} = \frac{F}{\gamma m} = \frac{Q v_t B}{\gamma m} \tag{B.3}$$

$$r = \frac{\gamma m v_t}{QB} = \frac{p_t}{QB} \tag{B.4}$$

If the the particle has a curved track like in Figure B.1 the equation B.2 assumes the form:

$$r = \frac{p \sin \vartheta}{QB} \tag{B.5}$$

Further from fig. B.1 one gets:

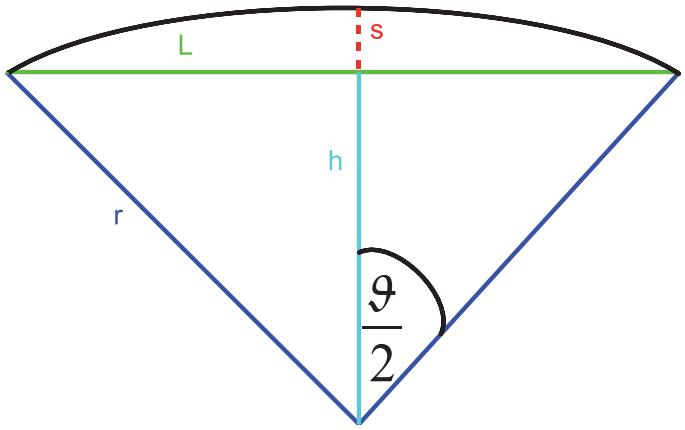

Figure B.1: Curvature of charged particles in a magnetic field

$$h^2 = r^2 - \left(\frac{L}{2}\right)^2 = r^2\left(1 - \frac{L^2}{4r^2}\right) \tag{B.6}$$

$$h = r\left(1 - \frac{L^2}{4r^2}\right)^{\frac{1}{2}} \approx r\left(1 - \frac{1}{2}\frac{L^2}{4r^2} + \mathcal{O}(1/r^4)\right) \tag{B.7}$$

$$s = r - h = r\frac{L^2}{8r^2} = \frac{L^2}{8r} \tag{B.8}$$

Putting the equations B.2 and B.6 together, the dependency of sagitta s and p_t can be expressed as:

$$s = \frac{L^2 QB}{8}\frac{1}{p_t} \tag{B.9}$$

So the magnitude of curvature depends on the p_t and the direction depends on the charge.

Appendix C

Used Data Samples

Name	N_{Events}	Cross section (LO)
/WJets-madgraph/Fall08_IDEAL_V11/GEN-SIM-RECO	$1 \cdot 10^7$	40 nb
/TTbar/Winter09_IDEAL_V11_FastSim/GEN-SIM-RECO	$1 \cdot 10^7$	317 pb
/WW_incl/Summer08_IDEAL_V11/GEN-SIM-RECO	$2.5 \cdot 10^5$	44.8 pb
/WZ_incl/Summer08_IDEALV11/GEN-SIM-RECO	$2.5 \cdot 10^5$	17.4 pb
/ZZ_incl/Summer08_IDEAL_V11/GEN-SIM-RECO	$2.5 \cdot 10^5$	7.1 pb

Table C.1: Used MC-Samples excluding Multi-jet

Name	N_{Events}	Cross section (LO)
/QCDpt470/Summer08_IDEAL_V11/GEN-SIM-RECO	$3 \cdot 10^6$	315 pb
/QCDpt800/Summer08_IDEAL_V11/GEN-SIM-RECO	$3 \cdot 10^6$	11.9 pb
/QCDpt1400/Summer08_IDEAL_V11/GEN-SIM-RECO	$1.5 \cdot 10^6$	0.172 pb
/QCDpt2200/Summer08_IDEAL_V11/GEN-SIM-RECO	$1.5 \cdot 10^6$	0.0014 pb
/QCDpt3000/Summer08_IDEAL_V11/GEN-SIM-RECO	$1.5 \cdot 10^6$	$86 \cdot 10^{-7}$ pb

Table C.2: Used Multi-jet samples.

The event generation is done with SHERPA 1.1.2. For the detector simulations CMSSW_2_2_9 has been used. The production of events is split up into three bins of the invariant di-muon mass $M_{\mu\mu}$:

Mass region [GeV]	Number of events generated
50-150	50000
150-450 (500)	50000
450 (500)-10000	100000

where only the last bin has a signal contribution. The generations have been performed for background and signal+background ($p + p \rightarrow \mu^+\mu^- + X$) in SHERPA. Following parameter points in GRW convention have been produced:

Fundamental Scale $M_S\,[TeV]$	1.5	2.0	2.5	3.0	3.5	4.0	SM
Number of ED n	2	2	2	2	2	2	$--$

GRW convention does not depend on the number of ED and so the number of Monte Carlo samples have been reduced. The conversion into the dimension depending HLZ convention is a straightforward exercise.

Appendix D

Additional ADD and SM-distributions

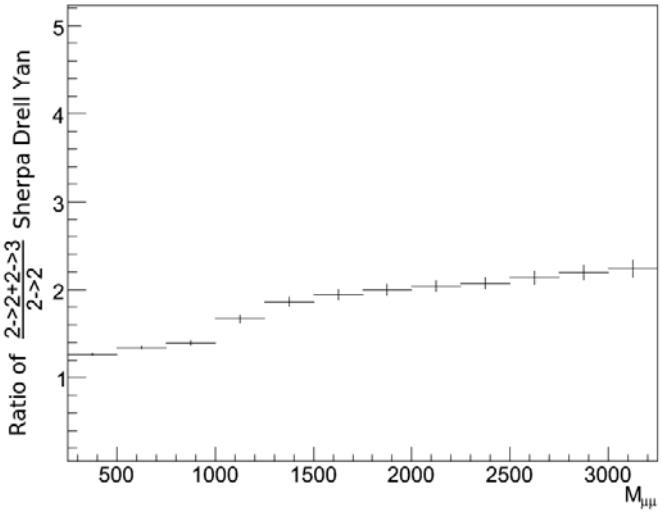

Figure D.1: Comparison of the $2 \to 2$ and $2 \to 2 + 2 \to 3$ process for $M_S = 2.5\,\text{TeV}$ (GRW) ADD Drel-Yan.

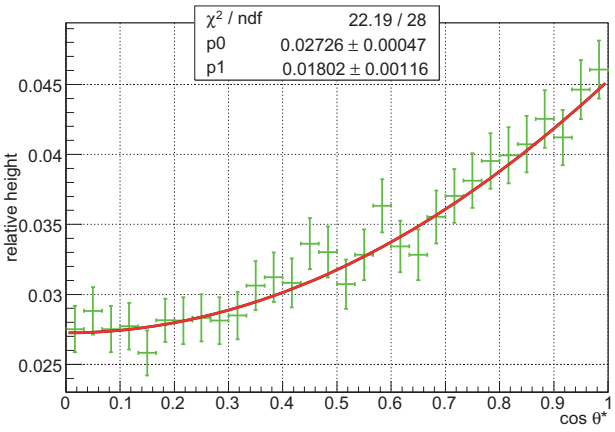

Figure D.2: Generator level $\cos\theta^*$ distribution for the Drell-Yan process. The function $A + B * \cos^2\theta^*$ has been fitted, where A and B are the fit parameters .

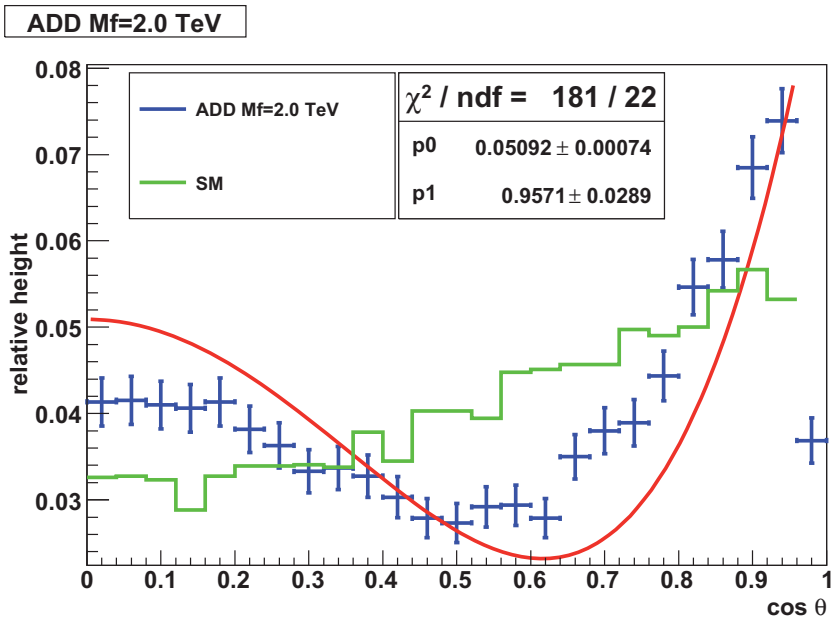

Figure D.3: $\cos\theta^*$-fit for $M_{\mu\mu}$>3.0 TeV and $M_S = 2.0$ TeV (GRW).

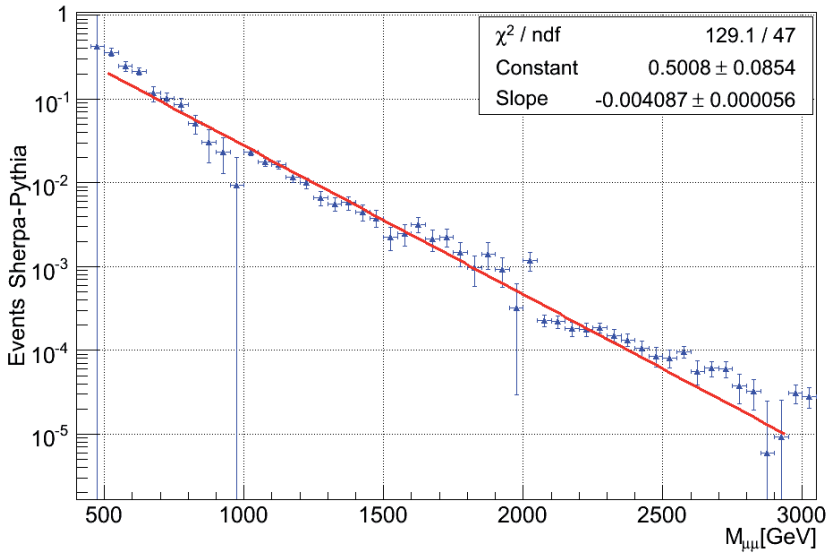

Figure D.4: Fitted exponential function to the difference of the SM-$M_{\mu\mu}$-distributions of SHERPA and PYTHIA.

List of Figures

List of Tables

Bibliography

[1] G. Altarelli, In *Landolt-Boernstein I 21A: Elementary particles* 3.

[2] CPEP, Website, 2009, Available online at http://www.cpepweb.org/.

[3] I. J. R. Aitchison and A. J. G. Hey, *Gauge Theories in Particle Physics: A Practical Introduction*, Second ed. (Hilger, Bristol UK, 1989).

[4] P. Schmüser, *Feynman-Graphen und Eichtheorien für Experimentalphysiker* .

[5] R. Manka, (1994), hep-ph/9405305.

[6] Pich, Antonio, (2007), arXiv:0705.4264.

[7] O. Klein, Z. Phys. **37**, 895 (1926).

[8] S. Hossenfelder, *Schwarze Löcher in Extra-Dimensionen, Eigenschaften und Nachweis*, PhD thesis, Goethe Universiät Frankfurt am Main, 2003.

[9] G. Gabadadze, (2003), hep-ph/0308112.

[10] Arkani-Hamed, Nima and Dimopoulos, Savas and Dvali, G. R., Phys. Lett. **B429**, 263 (1998), hep-ph/9803315.

[11] G. D. Kribs, (2006), hep-ph/0605325.

[12] EOT-Wachingten, Website, 2009, Available online at http://www.npl.washington.edu/eotwash/index.html;.

[13] R. D. Newman, E. C. Berg, and P. E. Boynton, Tests of the gravitational inverse square law at short ranges.

[14] D. J. Kapner *et al.*, Phys. Rev. Lett. **98**, 021101 (2007), hep-ph/0611184.

[15] Hannestad, Steen and Raffelt, Georg G., Phys. Rev. Lett. **88**, arXiv:071301 (2002).

[16] Han, Tao and Lykken, Joseph D. and Zhang, Ren-Jie, Phys. Rev. **D59**, 105006 (1999), hep-ph/9811350.

[17] Giudice, Gian F. and Rattazzi, Riccardo and Wells, James D., Nucl. Phys. **B544**, 3 (1999), hep-ph/9811291.

[18] R. Hamberg, W. L. van Neerven, and T. Matsuura, Nucl. Phys. **B359**, 343 (1991).

[19] F. A. Berends, G. J. H. Burgers, and W. L. van Neerven, Phys. Lett. **B185**, 395 (1987).

[20] K. Melnikov and F. Petriello, Phys. Rev. **D74**, 114017 (2006), hep-ph/0609070.

[21] Landsberg, Collider Searches for Extra Dimensions, 2004.

[22] D0, V. M. Abazov *et al.*, Phys. Rev. Lett. **102**, 051601 (2009), arXiv:0809.2813.

[23] D0, V. M. Abazov *et al.*, Phys. Rev. Lett. **95**, 161602 (2005), hep-ex/0506063.

[24] C. D. Server, Website, 2009, Available online at http://doc.cern.ch/yellowrep/2004/2004-003-v3.pdf;.

[25] L. Evans and P. Bryant, THE CERN LARGE HADRON COLLIDER: Accelerator and Detectors, 2008.

[26] ATLAS, G. Aad *et al.*, JINST **3**, S08003 (2008).

[27] CMS, R. Adolphi *et al.*, JINST **0803**, S08004 (2008).

[28] ALICE, K. Aamodt *et al.*, JINST **0803**, S08002 (2008).

[29] LHCb, A. A. Alves *et al.*, JINST **3**, S08005 (2008).

[30] CMS, the Compact Muon Solenoid. Muon technical design report, CERN-LHCC-97-32.

[31] T. C. Collaboration, The CMS experiment at the CERN LHC, JINST 3, S08004, 2008.

[32] CMS, Addendum to the CMS tracker TDR, CERN-LHCC-2000-016.

[33] CMS Tracker, C. Genta, CERN-CMS-CR-2008-098.

[34] G. Klaussen, Silicon Strip Detector Qualification for the CMS Experiment, 2008.

[35] CMS, G. L. Bayatian *et al.*, CMS physics: Technical design report, CERN-LHCC-2006-001.

[36] CMS, G. L. Bayatian *et al.*, J. Phys. **G34**, 995 (2007).

[37] The Hadron Calorimeter Project, Website, 1997, Available online at http://uscms.fnal.gov/uscms/Subsystems/HCAL/hcal_tdr/ch01/hcal_tdr_ch01.html.

[38] C. Lippmann, Detector Physics of Resistive Plate Chambers, 2003.

[39] CMS, e. . Sphicas, P., CMS: The TriDAS project. Technical design report, Vol. 2: Data acquisition and high-level trigger, CERN-LHCC-2002-026.

[40] L. C. Group, LHC 2009-2010 luminosity performance-estimate for 3.5 TeV plus move to higher energy, 2009.

[41] T. Gleisberg, *Automating methods to improve precision in Monte-Carlo event generation for particle colliders*, PhD thesis, TU Dresden, 2008.

[42] Particle Data Group, K. Hagiwara *et al.*, Phys. Rev. **D66**, 010001 (2008).

[43] T. Sjostrand, S. Mrenna, and P. Skands, JHEP **05**, 026 (2006), hep-ph/0603175.

[44] H. Buckley, Andy and Hoeth, H. Lacker, H. Schulz, and E. von Seggern, Monte Carlo tuning and generator validation, 2009.

[45] R. Corke and T. Sjostrand, Multiparton Interactions and Rescattering, 2009.

[46] J. Archibald *et al.*, Prepared for 16th International Workshop on Deep Inelastic Scattering and Related Subjects (DIS 2008), London, England, 7-11 Apr 2008.

[47] S. Schuhmann, *Simulation of signal and background processes for collider experiments*, PhD thesis, TU Dresden, 2008.

[48] Krauss, F., JHEP **08**, 015 (2002), hep-ph/0205283.

[49] N. Lavesson and L. Lonnblad, JHEP **04**, 085 (2008), arXiv:0712.2966.

[50] A. Schaelicke, *Event generation at hadron colliders*, PhD thesis, TU Dresden, 2005.

[51] S. Hoeche, F. Krauss, S. Schumann, and F. Siegert, JHEP **05**, 053 (2009), arXiv:0903.1219.

[52] Stefanis, N. G., (1998), hep-ph/9811262.

[53] T. Gleisberg *et al.*, JHEP **09**, 001 (2003), hep-ph/0306182.

[54] CMS Collaboration, Markus Merschmeyer, Website, 2009, Available online at https://twiki.cern.ch/twiki/bin/view/CMS/SherpaInterface.

[55] C. Collaboration, Website, 2009, Available online at https://twiki.cern.ch/twiki/bin/view/CMS/WorkBookCMSSWFramework.

[56] R. Brun, R. Hagelberg, M. Hansroul, and J. C. Lassalle, CERN-DD-78-2-REV.

[57] CERN, *GEANT, detector description and simulation tool*, 1994, Program library long writeup W5013.

[58] C. Collaboration, Website, 2009, Available online at https://twiki.cern.ch/twiki/bin/view/CMS/WorkBookPAT.

[59] C. Collaboration, Website, 2009, Available online at https://twiki.cern.ch/twiki/bin/view/CMS/Aachen3ASusy.

[60] R. Fruhwirth, Nucl. Instrum. Meth. **A262**, 444 (1987).

[61] Particle Data Group, S. Eidelman *et al.*, Phys. Lett. **B592**, 1 (2006).

[62] Viatcheslav Valuev (UCLA), CFT-09-014-paper (2009).

[63] C. Collaboration, Website, 2009, Available online at Seehttps://twiki.cern.ch/twiki/bin/view/CMS/TSG_18_II_09_1E31#HltMu9.

[64] CMS Collaboration Muon Physics Object Group, Website, 2009, Available online at https://twiki.cern.ch/twiki/bin/view/CMS/MuonPOG.

[65] I.Bloch et al., CMS-AN-2008/098 (2008).

[66] C. Collaboration, Website, 2009, Available online at https://twiki.cern.ch/twiki/bin/view/CMS/WorkBookFireworks.

[67] Sippach, W., Paper published in the Proceedings of the Workshop on Triggering, Data Acquisition, and Offline Computing for High Energy / High Luminosity Hadron-Hadron Colliders, 11- 14 November, 1985, Fermilab, Batavia, IL.

[68] CMS, Fiore, L., Nucl. Instrum. Meth. **A473**, 39 (2001).

[69] C. Collaboration, Website, 2009, Available online at https://twiki.cern.ch/twiki/bin/view/CMS/CRAFTPaperWorkflows.

[70] The CMS Collaboration, Website, 2009, Available online at https://twiki.cern.ch/twiki/bin/view/CMS/AlCaScenarios.

[71] Jim Pivarski, 2009, Private Communications.

[72] N. de Filippis, F. P. Schilling, A. Schmidt, M. Weber, Update of Misalignment Scenarios for the CMS Tracker, 2007, CMS IN 2007/036.

[73] G.Abbiendi et al., CMS-AN-2008/097 (2008).

[74] Glen Cowan, Multivariate statistical methods and data mining in particle physics, 2008.

[75] Volker Blobel and Erich Lohrmann, *Statistische und numerische Methoden der Datenanalyse*, 1 ed. (Teubner Verlag, 1998).

[76] Lucien M. LeCam and Jerzy Neyman, editor, *Theory of statistics*, Berkeley, Calif., 1972, University of California Press.

[77] Read, Alexander L., Prepared for Workshop on Confidence Limits, Geneva, Switzerland, 17-18 Jan 2000.

[78] Read, Alexander L., J. Phys. **G28**, 2693 (2002).

[79] The CMS Collaboration, Website, 2009, Available online at https://twiki.cern.ch/twiki/bin/view/RooStats/WebHome.

[80] W. J. Metzger, Statistical Methods in Data Analysis, 2002.

[81] H. Burkhardt, R. Schmidt, CERN-AB-2004-032 (ABP) (2004).

[82] The CMS Collaboration, Website, 2009, Available online at https://twiki.cern.ch/twiki/bin/view/CMS/TWikiEWK.

[83] The CMS Collaboration, Towards a measurement of the inclusive W and Z cross sections in pp collisions at s = sqrt10 TeV, CMS PAS 2009/001 (2009).

[84] The CMS Collaboration, Website, 2009, Available online at https://twiki.cern.ch/twiki/bin/view/CMS/TeVMuons.

[85] D. Bourilkov, (2003), hep-ph/0305126.

[86] The CMS Collaboration,Search for New High-Mass Resonances Decaying to Muon Pairs in the CMS Experiment , CMS AN-2007/038 (2007).

[87] Piotr Traczyk, 2009, Private Communications.

[88] P. Mathews and V. Ravindran, Nucl. Phys. Proc. Suppl. **157**, 251 (2006).

[89] Prakash Mathews, 2009, Private Communications.

[90] P. Biallass, T. Hebbeker, C. Hof, A. Meyer, and S. A. Schmitz, MUSiC - An Automated Scan for Deviations between Data and Monte Carlo Simulation, 2008, CMS AN-2008/065.

[91] B. C. Allanach *et al.*, JHEP **12**, 039 (2002), hep-ph/0211205.

[92] Mathews, Prakash and Ravindran, V., Nucl. Phys. **B753**, 1 (2006), hep-ph/0507250.

[93] J.P.Chou,Selda Esen, Greg Landsberg, Duong Nguyen, Search for Large Extra Dimensions in Diphoton Final State in CMS, 2009, CMS AN-2009/062.

Trivia

I would like to conclude this thesis with a very joyful event. The day before yesterday, November the 24th in the year 2009 has been a very special one. The first collisions at LHC took place.

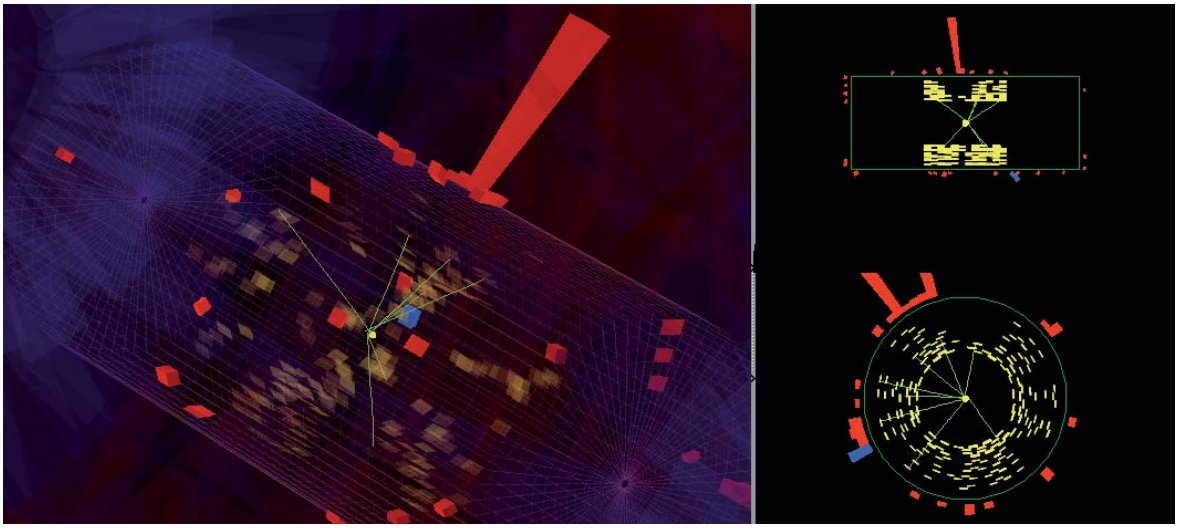

Figure D.5: First collision event reconstructed with the CMS detector.

Hopefully we will be able to get a new idea of phyisics in the Tera-scale with the LHC. I am glad to be witness of it and congratulate all scientists who spend a lot of time and effort in designing, planing, builing (repairing), and finally now "using" the LHC. I also hope that many theses will be written using the LHC data, as I claim to be (very likely) the first one ;-) (see Figure D.5).

Danksagung/Acknowledgements

Nun ist ein Jahr vergangen und diese Arbeit kommt zum Ende. Höchste Zeit also den vielen Personen zu danken, die mich in diesem Jahr unterstützt haben. Den ersten Dank möchte ich an Prof. Dr. Hebbeker richten, welcher mir diese Arbeit anbot und mich ein Jahr lang betreut hat. Vielen Dank auch an Prof. Dr. Wiebusch für die Zeit die er sich nimmt, um meine Arbeit als Zweitgutachter zu lesen. Ich danke der Aachener CMS Gruppe für die Hilfe und ausgezeichnete Arbeitsatmosphäre hier vor Ort und auch z.B. auf den vielen Dienstfahrten.
Kerstin Hoepfner, Jens Frangenheim und Carsten Hof, ich bedanke mich bei Euch für das Korrekturlesen dieser Arbeit.
Arnd Meyer, vielen Dank für die intesive Hilfe und Anregungen bei der Analyse.
Carsten Magass, großen Dank für den Umbau des SUSY-Fillers, so dass ich es auch mit SHERPA Sachen benutzen konnte.
Markus Merschmeyer, vielen Dank für die gute Stimmung bei uns im Büro und die Hilfe z.B. bei SHERPA -Angelegenheiten.
Prof. Dr. Dr. h.c. Mathias Bauer danke ich für seine Mühen bei der Betreuung außerhalb der Physik.
Prof. Dr. Zerwas und Prof. Dr. Böhm danke ich für die viele Zeit, welche sich beide genommen haben, um meine Fragen zu beantworten.
An meine vielen Freunde, ich danke Euch für die große Unterstützung und die viele Zeit, die ich mit Euch zusammen verbringe.

I would like to thank the whole SHERPA team for their support and quick answers. Further thanks go to Greg Landsberg for his assistance and his analysis experience he shared with me. Also thanks to Jim Pivarski for the alignment support.
Special thanks to Prakash Mathews et. al. for the immediate help with the higher order calculations.

Mit der Abgabe der Diplomarbeit versichere ich hiermit schriftlich, dass ich die Arbeit selbständig verfasst und keine anderen als die angegebenen Quellen und Hilfsmittel benutzt sowie Zitate kenntlich gemacht habe.